DESIGN OF A PANTOGRAPHIC SYSTEM FOR RECHARGING ELECTRICAL URBAN BUSES

Matteo Di Fonzo

Department of Mechanical and Aerospace Engineering
Master Degree in Mechanical Engineering

Supervisors:

Antoni Grau Saldes

Stefano Marchesiello

Politecnico di Torino

Universitat Politécnica de Catalunya

A.Y. 2024/2025

Contents

List of Figures

List of Tables

Chapter 1

Introduction

1.1 Context

In recent years, the issue of global warming has led to a growing interest in sustainability, with the transportation sector being one of the most affected. There is a high demand for achieving zero-emission transportation.

In the 21st century, the car is considered a primary necessity, much like housing. It is difficult to imagine life without cars, especially given the increasing need for travel and mobility observed in recent years.

According to a 2019 article by the European Parliament, the transportation sector is responsible for 25% of CO_2 emissions, with 71.7% of them coming from road transport. Driven by research studies, legislation is evolving to impose stricter pollution limitations. The EU has set two key objectives: compared to 1990 CO_2 emission levels, it aims to achieve a 60% reduction in transport-related CO_2 emissions by 2030 and a 90% reduction by 2050. However, despite a steady decrease in emissions over the years, a countertrend was observed in 2017 due to increased mobility. This indicates that achieving these goals will not be easy [3].

Among these emissions, cars represent the largest contributor. This impact could be reduced if cars were used to transport multiple passengers, but the average occupancy of a car is only 1.7 persons [3].

Given this scenario, it is clear that limiting the use of personal vehicles in favor of more sustainable transportation alternatives is necessary.

In line with the European Green Deal's objective of climate neutrality by 2050, Kyoto Club and CNR-IIA have compiled a list of possible initiatives that governments and local authorities should adopt [4]:

- increasing investment in the railway sector by introducing new routes for commuters;

- enhancing public transport within cities;

- establishing low-emission zones in cities, where cars, motorcycles, and polluting commercial vehicles are restricted;

- promoting electric mobility.

As highlighted in this list, one of the key solutions is the use of public transport, which helps reduce traffic congestion by discouraging car usage.

In major cities, the public transport sector is continuously improving, with new routes and more efficient technologies being developed.

Public transport agencies are particularly interested in this shift towards sustainability to comply with the stricter regulations that governments will impose in the coming years.

The primary means of combating global warming in this sector is the adoption of electric vehicles.

Although concerns exist regarding the fact that a significant portion of electricity is still generated from coal, the environmental benefits of electric vehicles remain undeniable. Furthermore, with ongoing technological advancements, these benefits are only expected to increase [5].

Today, most major cities employ hybrid or fully electric vehicles. This transition has been facilitated by economic incentives provided by governments to support transport agencies [6] [5].

One of the key aspects to consider when transitioning to fully electric vehicles is their range and the time required for recharging. A technological solution to this challenge is the implementation of charging breaks between routes.

A fully electric bus can be equipped with a charging infrastructure at the final stop of its route. With a short service break, typically lasting 5 to 10 minutes, the bus undergoes a rapid partial charge of its batteries. As a result, the bus begins its daily service with fully charged batteries and recharges at the end of each route with brief stops to ensure continuous operation.

These charging systems are usually located at the final stops of routes and are designed to deliver a large amount of energy in a short time.

One of the technologies used for this purpose is the pantograph system, which will be analyzed in detail in the following sections.

1.2 Research Motivation and Scope of the thesis

Barcelona is one of the big cities with more interest in sustainability and in step with recent sustainable developments.

In fact the city adopted an urban planning project in order to become more sustainable and livable by encouraging the growth of green spaces and making roads less busy.

Superblocks have redefined urban mobility by shifting the modal split towards public transport, cycling and pedestrians but they also intend to improve urban green infrastructure and biodiversity by creating urban corridors that cross the city [7].

In 2023 Barcelona has registered a record in sustainable movements: the 80.1% of movements has been done on foot, with a bicycle, devices of personal mobility or with public transport [8].

The public transport uses many 100% electric vehicles. One of its transport lines, the H16, uses for its service a full electric bus which receives an energy charge every time it ends its route via a pantograph system [9]. This device concerns the focus of this work.

In the following a modeling of the pantograph realized by SolidWorks will be shown, in order to analyze its mechanical behavior. It will be accompanied by a comparison with fuel engines in order to determine not only the sustainable advantages, but also the economic ones.

1.3 Research Objectives

The main objective of this research is to model a pantograph system in SolidWorks taking into account a real application of it to recharge a full electric bus.
The work analyses the system under its mechanical aspects, focusing on critical points such as the attack and detachment moments between the pantograph and the recharging structure.

Chapter 2

Electricity vs Fuel

2.1 Is Electricity Truly Zero-Emission?

The debate between fuel-powered and electric vehicles remains a crucial topic in the transition toward sustainable mobility. A common misconception is that electricity equates to zero emissions, particularly in the transportation sector. However, a comprehensive evaluation must consider the entire energy production process.

While battery electric vehicles (BEVs) produce zero tailpipe emissions, the electricity used to charge them often originates from power plants that generate emissions through the extraction, processing, and distribution of primary energy sources [10]. The environmental benefits of electric vehicles (EVs) largely depend on the energy mix of a given region. In countries with a high share of renewable energy, EVs provide a clear advantage over conventional internal combustion engine (ICE) vehicles. Conversely, in areas where electricity is primarily generated from fossil fuels, the overall reduction in emissions is less significant [10].

Moreover, differences in energy management strategies across countries can influence the sustainability of electric mobility. For instance, nations with substantial solar power generation may prioritize daytime vehicle charging, whereas those relying on wind energy may require different grid management approaches [11].

The following graph illustrates the energy sources used for electricity generation in the United States, based on national averages across all 50 states:

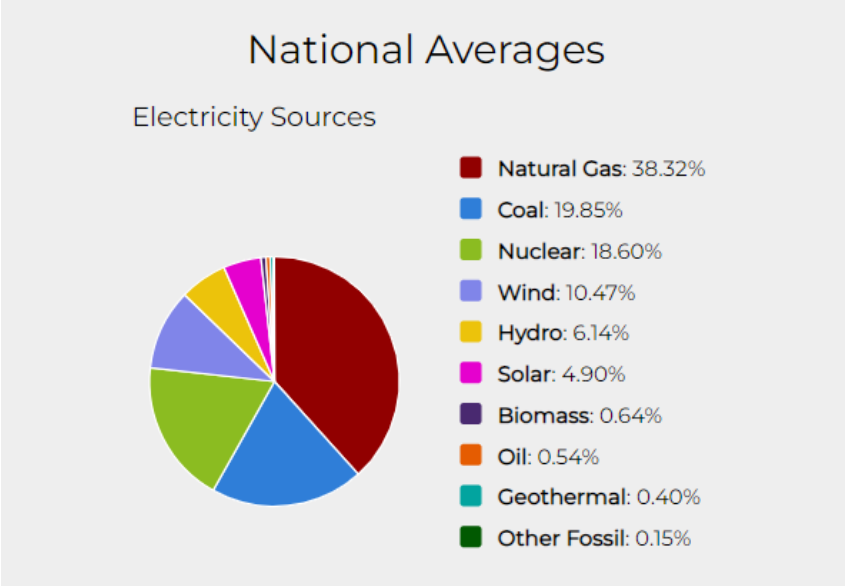

Figure 2.1: Electricity generation sources in the United States.

The life-cycle emissions of gasoline-powered vehicles include pollutants released during oil extraction, refining, fuel distribution, and combustion. In contrast, electric vehicles eliminate direct emissions, but their life-cycle impact depends on the source of electricity generation.

A comparative analysis of vehicle emissions highlights the advantages of electrification. The following graph displays the annual CO_2 emissions for different vehicle types in the United States:

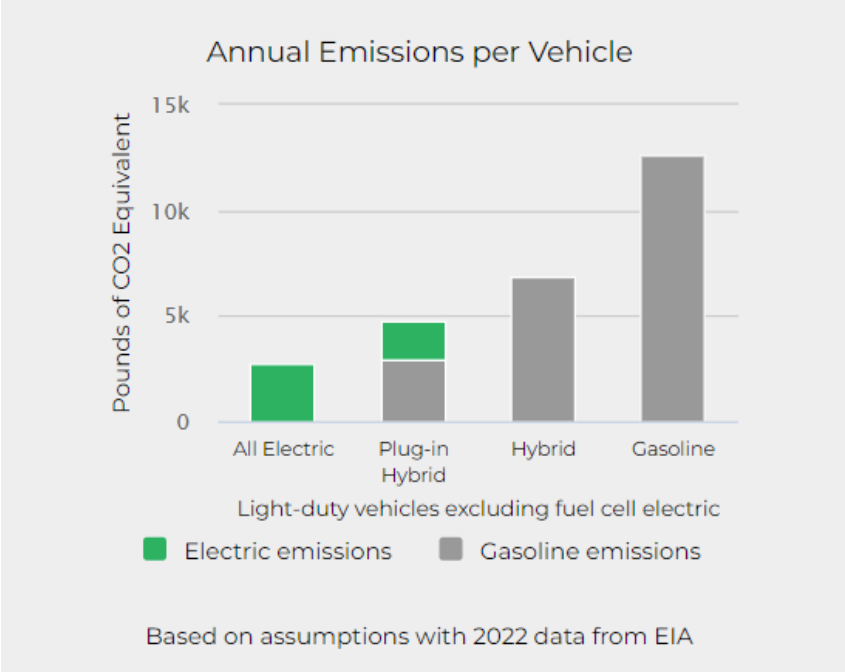

Figure 2.2: Annual CO_2 emissions per vehicle.

The adoption of EVs will inevitably lead to an increased demand for electricity. According to the European Environment Agency, the total electricity consumption from electric

vehicles accounted for approximately 0.03% of total electricity use in 2014. Projections suggest this figure will rise to 4-5% by 2030 and reach 9.5% by 2050, assuming that 80% of the vehicle fleet will be electric by then [11]. While the demand increases until 2030 is expected to be manageable, the energy requirements by 2050 will have a significant impact on power systems.

Despite these challenges, the net effect of electrification remains positive. The shift to EVs will lead to a substantial reduction in CO_2 emissions from road transport, outweighing the additional emissions from electricity generation, as illustrated in the following graph:

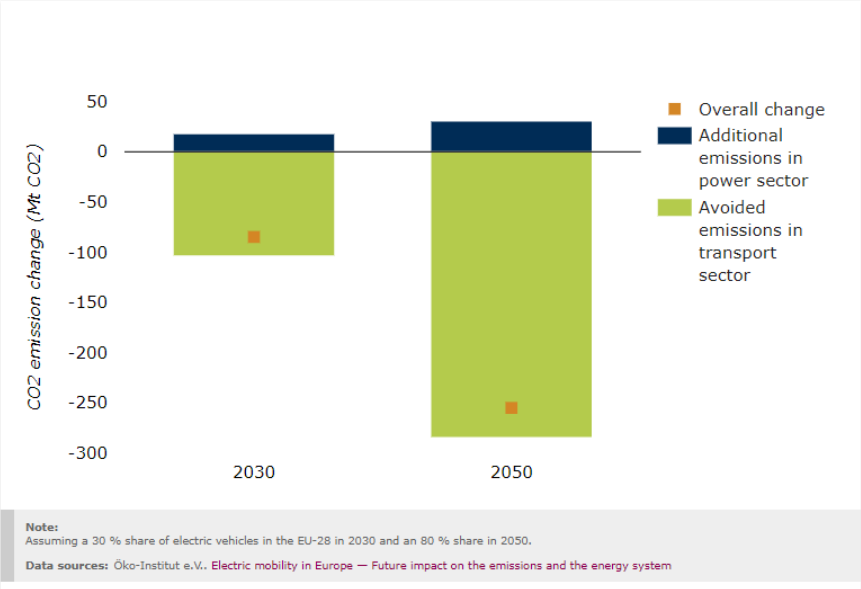

Figure 2.3: Projected changes in CO_2 emissions due to vehicle electrification.

According to data from Oko-Institut e.V., "Electric mobility in Europe - Future impact on the emissions and the energy system," the reduction in emissions from the transport sector will be significantly greater than the increase in emissions from electricity production [12].

Another key consideration is the impact of emissions on human health. Unlike power plants, which are typically located in industrial zones with lower population densities, road transport emissions occur at ground level in urban areas where exposure to pollutants is significantly higher. A transition from gasoline-powered vehicles to EVs could therefore lead to considerable health benefits by reducing direct emissions in densely populated areas [11].

A final aspect to consider is the end-of-life impact of EVs. The materials used in batteries, including critical raw materials, require energy-intensive processing and may generate hazardous waste. Effective recycling strategies are essential to minimize environmental harm and maximize resource efficiency. The reuse or repurposing of EV batteries can help mitigate their environmental footprint and reduce waste generation [5].

In summary, while electricity generation is not entirely emission-free, the overall benefits of electrification in transportation are clear. The reduction in direct emissions, lower CO_2

output over a vehicle's lifetime, and potential health improvements outweigh the challenges associated with increased electricity demand and battery recycling. The transition to a cleaner energy mix will further enhance the environmental advantages of EVs in the coming decades.

2.2 Barcelona's case

As mentioned in the introduction, Barcelona is one of the most advanced cities in terms of environmental commitment. Since 2015, the city has adopted a strategic approach to mitigate climate change by actively involving its citizens. These initiatives offer multiple benefits in environmental, economic, and public health sectors [13]. The goal is to reduce CO_2 emissions and expand green urban areas by 1.6 km^2 by 2030 [13].

One of the key solutions implemented is an urban redevelopment project aimed at enhancing sustainability and livability by increasing green spaces and reducing traffic congestion.

As introduced earlier, this strategy involves the creation of *superblocks*: 400 x 400 m units that are larger than a city block but smaller than a neighborhood. These superblocks reorganize urban space to prioritize pedestrians by restricting car access within certain areas.

The following figure illustrates a superblock:

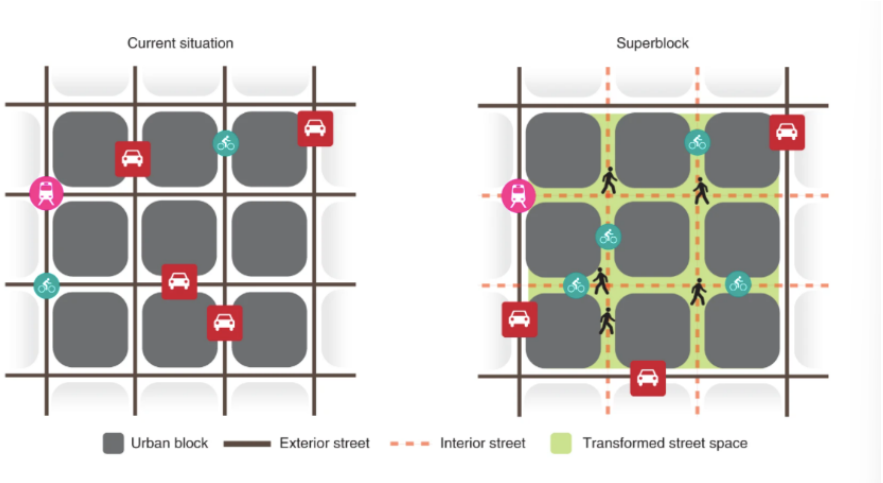

Figure 2.4: Superblocks

Barcelona is one of the most congested and densely populated cities in Europe. The implementation of superblocks, first introduced in the Eixample district, has demonstrated clear benefits for both the environment and residents.

The urban structure consists of nine superblocks, with internal streets where speed limits are restricted to 10-20 km/h.

This initiative has reshaped urban mobility by shifting transportation preferences towards public transit, cycling, and walking [7].

As a result, in 2023, Barcelona achieved a milestone in sustainable mobility: 80.1% of trips were made on foot, by bicycle, or via public transport [8].

The city is currently developing its Urban Mobility Plan (UMP) 2025-2030, which focuses on three main objectives:

1. Establishing a safe, efficient, and sustainable mobility model.
2. Strengthening public transportation to encourage a shift from private vehicles.
3. Reducing car and motorcycle dependency while mitigating their negative impacts.

These initiatives have led to a significant increase in public transport usage, which grew by 18% between 2022 and 2023 [8].

2.3 Electric buses technology

Having highlighted the importance of the transition to electric vehicles, and how Barcelona stands among the cities most committed to ecological transformation, before presenting the city's specific public transport initiatives, this paragraph aims to provide an overview of the electric bus sector, illustrating the different technologies that can be employed to achieve a fully sustainable vehicle.

Electric buses rely entirely on electric power to operate all on-board systems. Since they involve no combustion process, they produce no tailpipe emissions—neither carbon dioxide (CO_2) nor any type of local pollutant.

Electric buses can be battery-electric (BEB) or hydrogen fuel cell buses, both of which employ an electric motor.
The main difference lies in the energy source: while battery-electric buses are recharged directly from the electrical grid, fuel cell buses are equipped with a fuel cell that generates electricity on board through the combination of hydrogen and oxygen drawn from the ambient air.

Hydrogen-powered vehicles offer a driving range comparable to that of diesel buses, making the technology particularly attractive. However, due to the current state of development and high costs—along with the economic and sustainability challenges associated with hydrogen production—they are still disadvantaged. Additionally, hydrogen buses require constant monitoring during refueling, as temperature, pressure, and tank charge status must be carefully supervised [2] [14].

For these reasons, battery-electric vehicles currently remain the most competitive solution in terms of operating costs for electric propulsion.

In general, battery electric buses can be classified into two categories: long-range BEBs and fast-charging BEBs.

Long-range BEBs are equipped with large battery packs to maximize range between charges, often favoring low-power charging to reduce grid impact. Full charging can take up to 8 hours or more, depending on battery capacity and charger power. Typical values include:

- Battery capacity: 250–660 kWh
- Service range: over 150 km on a single charge
- Required charging power: 50–150 kW

Fast-charging BEBs, on the other hand, use smaller battery packs as they are designed for frequent, high-power charging during operation, often multiple times per day. Typical values include:

- Battery capacity: 50–250 kWh
- Service range: not fixed, as a well-designed and dense charging network could enable continuous operation without the need for full charging stops
- Required charging power: 150–600 kW via pantograph or wireless charging systems along the route

The remainder of this thesis will focus on pantograph technology, which is employed for the fast charging of BEBs. [2]

2.4 Public Transport and H16 line

In alignment with Barcelona's long-term sustainability objectives, public transport plays a pivotal role in reducing urban emissions and improving energy efficiency.

In recent years, the metropolitan transport agency, Transports Metropolitans de Barcelona (TMB), has undertaken a progressive replacement of its conventional fleet. Since 2021, TMB has ordered 210 new hybrid and electric buses, ensuring that its operations now rely exclusively on electric, hybrid, or compressed natural gas (CNG) vehicles, thereby completing the phase-out of diesel-powered buses. This transition, while requiring significant investment, is a strategic measure to achieve the targets outlined in TMB's 2025 Strategic Plan and to move towards the 2050 objective of a fully sustainable public transport network [15].

The H16 line represents a flagship example of this transformation. In the summer of 2021, it became the first fully electric bus line in Barcelona [16]. The line was selected due to its high passenger demand—over 20,000 daily users—and its operational characteristics, which include 18-meter articulated buses to ensure adequate capacity. The full electrification of the route means that all 22 vehicles assigned to the H16 are 100% electric, making it an ideal case study for evaluating electric mobility solutions in high-demand

contexts.

The success of the H16 electrification relies heavily on the deployment of a robust charging infrastructure at both termini of the route. There are several charging strategies available for electric buses in public transport. Figure 2.5 illustrates the main options, ranging from overnight depot charging to high-power on-route charging.

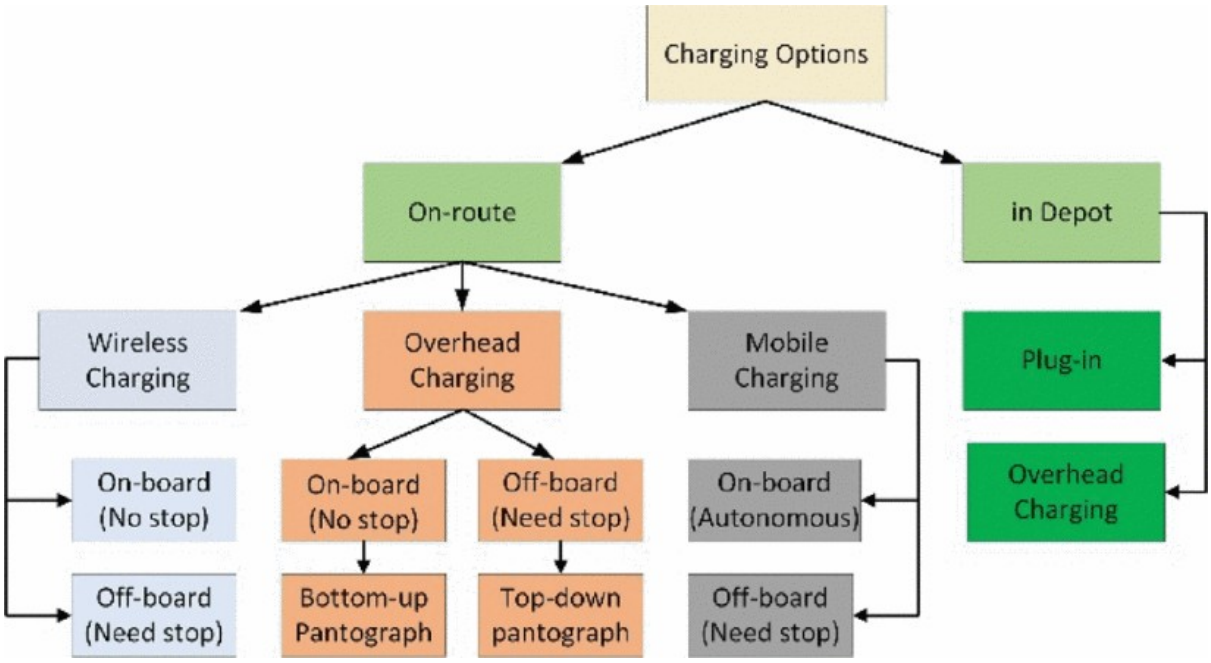

Figure 2.5: Charging options for electric buses

On-route charging enables buses to operate with smaller battery capacities, thereby improving efficiency by reducing weight and cost. For this reason, it is frequently preferred in modern urban transport systems. However, the high instantaneous power demand of these systems can pose challenges to the electrical grid, including voltage stability issues, increased transmission losses, and potential impacts on power quality. Effective control strategies are therefore essential to mitigate these effects [17].

In the case of the H16 line, the buses employ a pantograph-based fast-charging system capable of recharging up to 80% of the battery in under eight minutes.
This approach allows buses to maintain uninterrupted service throughout the day, while full recharging is carried out overnight at TMB depots. Such a strategy avoids the need for oversized batteries, optimising both energy efficiency and vehicle weight.
The pantograph infrastructure was developed by Endesa, with the first prototype installed and tested in 2016, positioning Barcelona as one of the pioneers in large-scale deployment of this technology [18].

2.5 Comparative Analysis of Battery Electric Bus Charging Strategies

This section presents a comparison of the main charging strategies for Battery Electric Buses (BEBs), highlighting the advantages and disadvantages of each approach. The aim is to provide a clear overview of the technology discussed and analyzed in the subsequent stages of this thesis.

2.5.1 Depot Charging

In this approach, the bus is charged at the depot during downtime, predominantly overnight. Charging can be performed via a fixed cable connection to the charging infrastructure or through a pantograph system.

The charging power typically ranges from 25 kW to 150 kW, with charging times between 5 and 8 hours. Energy storage systems (batteries) are usually large in size, enabling the bus to complete its scheduled service without additional charging. To increase availability, opportunity charging may also be performed during operation, either at stops or at terminal stations.

Advantages	**Disadvantages**
Lower unit costs, as all chargers are located in a single facility	Slow charging process
Easier maintenance	Required space increases with fleet size
Flexible design	Plug-in charging requires staff intervention
Buses are not bound to fixed routes, allowing greater operational flexibility	Simultaneous charging of multiple buses can cause power demand peaks, requiring load management systems
Scalable solution for large fleets	
Charging occurs during idle periods	
Overnight charging benefits from lower electricity tariffs	

Table 2.1: Depot Charging: Advantages and Disadvantages

2.5.2 Opportunity Charging via Pantograph at Terminals and/or Selected Stops

In this strategy, the bus undergoes high-power opportunity charging at terminal stations or selected stops along the route. The same charger can serve multiple buses operating on the line.

Charging power ranges between 150 kW and 600 kW (depending on dwell times) and is achieved through an automated connection between the charging mast and the vehicle roof via a pantograph.

Charging times are very short, 5–8 minutes at terminal stations (compatible with scheduled layovers) and only 20–30 seconds at equipped intermediate stops. The process does not aim to fully recharge the battery to 100%, but rather to provide enough energy to reach the next charging opportunity. For this reason, smaller battery packs are used, typically Lithium-Titanate-Oxide (LTO) for high-power cycles, while Nickel-Manganese-Cobalt (NMC) batteries are more suitable for overnight charging.

Advantages	**Disadvantages**
Infrastructure costs can be contained if few charging stations are used by multiple vehicles	Very high charging power can create electricity demand peaks
Easily integrated into existing bus lines with minimal route adjustments	Pantograph must be precisely aligned during charging
Automatic connection process	Maintenance complexity may increase depending on infrastructure distribution
Enables virtually unlimited operational time	
Charging can occur while the bus remains in service	
Ongoing EU and US standardization efforts	
Smaller onboard batteries reduce cost, weight, and complexity	
Lower battery weight allows for higher passenger capacity	

Table 2.2: Opportunity Charging: Advantages and Disadvantages

The following figure, taken from an ABB product catalogue, illustrates example cases of charging infrastructure deployment under different application scenarios [1].

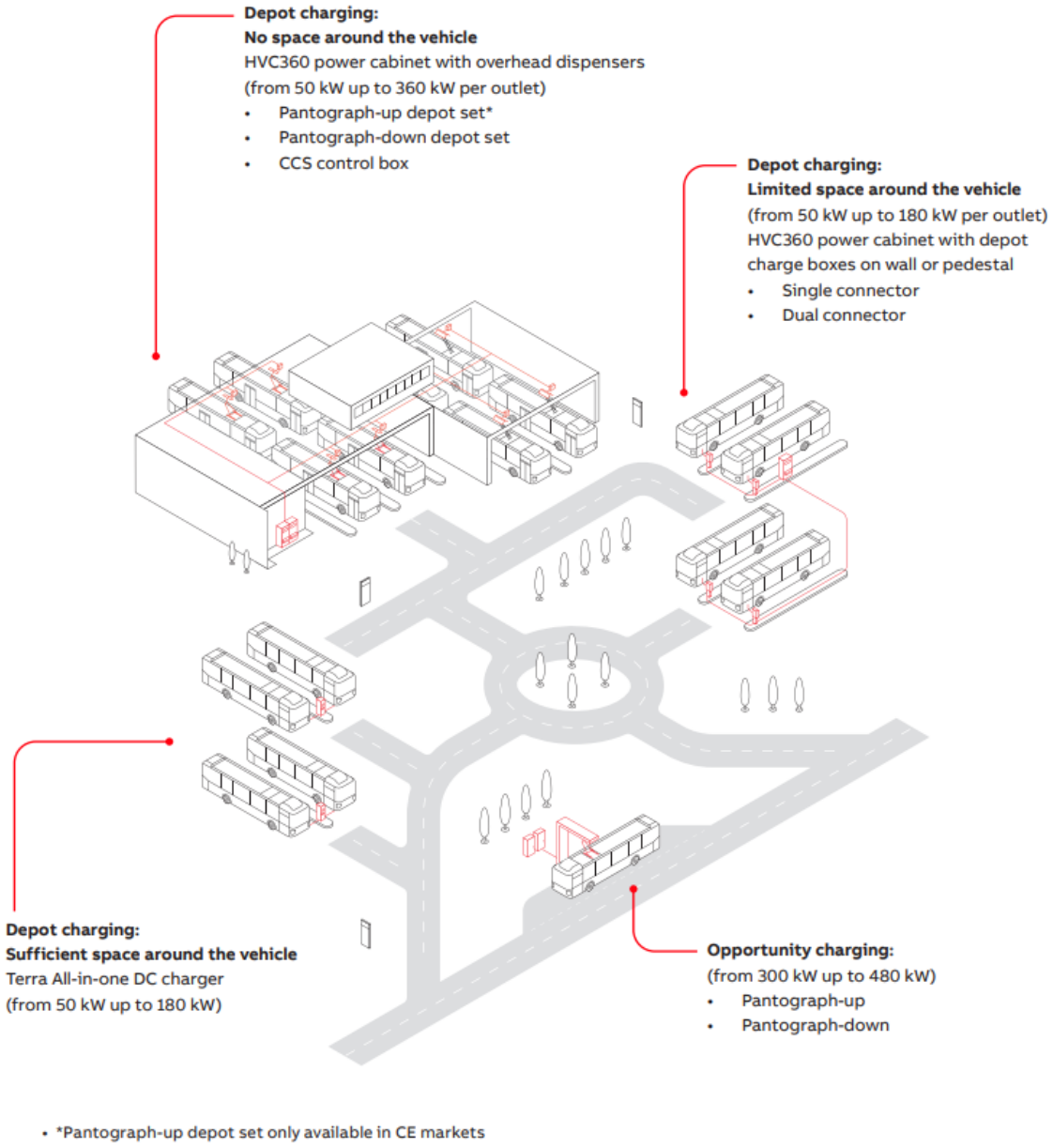

Figure 2.6: Example applications of charging infrastructure (source: ABB catalogue) [1]

2.5.3 Wireless Inductive Charging

This discontinuous charging system uses fixed stations to supply power via inductive coupling. The stations are installed at selected stops or terminal points. The same charger can serve multiple buses in alternation, with power levels typically ranging from 50 kW to 250 kW.

Advantages	Disadvantages
Infrastructure costs can be significantly reduced if chargers are shared among many buses	Higher capital and construction costs per charger
No manual or moving-part connections; fully automated process	Charging efficiency depends on bus alignment with the pad
Best aesthetic and visual integration in the urban environment	Maintenance may require road surface interventions
Unaffected by adverse weather conditions	Limited real-world deployment
Charging can occur while the bus remains operational	

Table 2.3: Wireless Inductive Charging: Advantages and Disadvantages [2]

2.5.4 Strategic Charging: The Key to Sustainable and Efficient Bus Operations

There is no universally "best" charging method; rather, the most suitable choice depends on the specific application. Factors influencing the decision include:

- Fleet size
- Route characteristics (speed, gradient, number of stops)
- Service timetables
- Available electrical capacity and electricity tariffs at stops, terminals, or depots
- Route length and duration
- Passenger load
- Seasonal and operational temperatures
- Space availability for infrastructure

An efficient charging system can substantially reduce the operational costs of an electric bus fleet. Once installed, charging infrastructures generally have lower maintenance costs and a longer operational lifespan compared to the buses themselves.

It is therefore essential to define effective battery charging strategies, which depend on the required charging time and timetable constraints.

For depot charging, large-capacity batteries are required to ensure autonomy for the entire scheduled service. However, such batteries significantly increase cost, weight, and vehicle mass, often representing up to 45% of the total vehicle cost, and reduce passenger capacity.

In the case of opportunity charging at terminal stations, as implemented on Barcelona's H16 line, the bus must recharge in less time than the scheduled layover. Layovers are primarily intended for driver rest and to compensate for potential service delays. During peak hours, when layover times are shorter, partial charging may be necessary, just enough to reach the next charging point, thereby ensuring virtually unlimited operational autonomy without compromising schedule adherence.

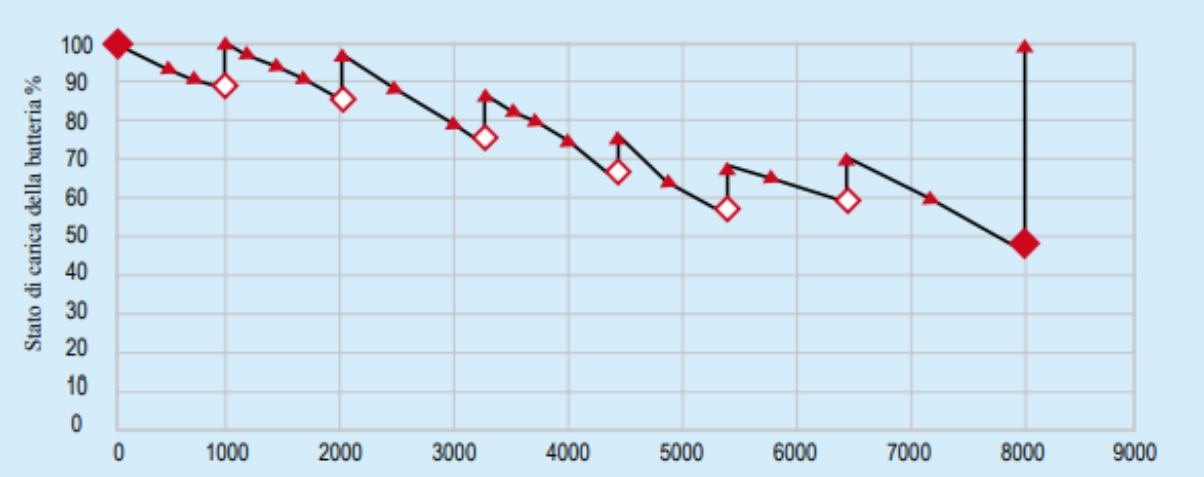

Figure 2.7: Example of Partial Battery Recharges in an Electric Bus

Ultimately, selecting the most appropriate charging system for a Battery Electric Bus is a critical decision. When performed optimally, charging operations can enable an electric bus line to be managed with a low Total Cost of Ownership (TCO) while ensuring efficient transport and a negligible environmental impact [2].

2.6 Total Cost of Ownership of Battery Electric Buses

The Total Cost of Ownership (TCO) is a key metric for assessing the costs associated with the entire life cycle of an electric bus. In general, the TCO of a Battery Electric Bus (BEB) is more advantageous than that of a conventional diesel bus, despite the higher initial investment cost.

The main driver of this upfront cost is the battery pack, which represents not only a significant portion of the purchase price but also a critical factor in determining vehicle performance. Over the last decade, however, the global production capacity of batteries has increased at a faster pace than demand. This trend has resulted in a substantial reduction in the cost per kilowatt-hour, as shown in the following table of historical and projected prices.

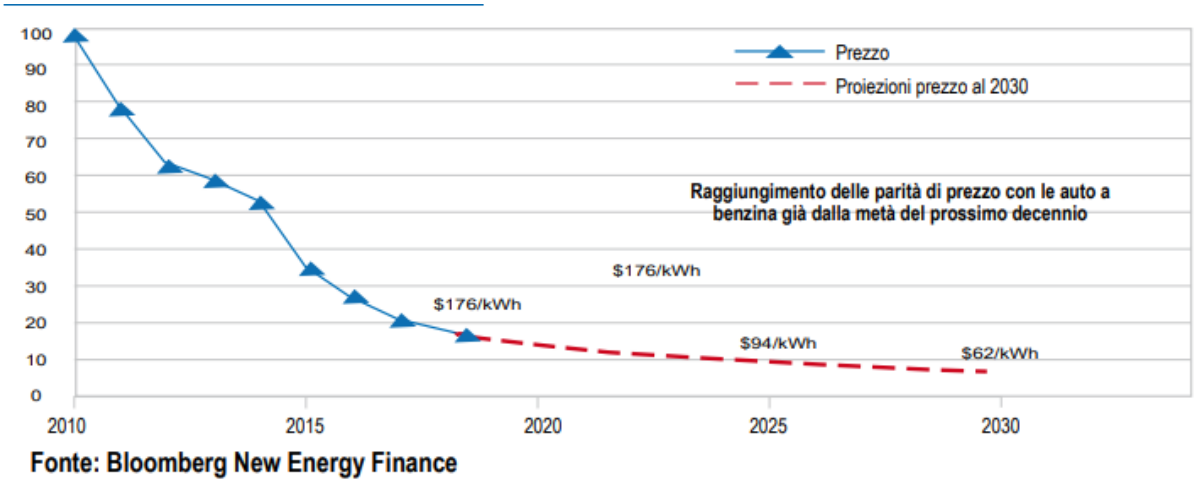

Figure 2.8: Historical and projected battery prices [2]

Battery prices vary depending on the cell chemistry, production volumes, and battery pack design, which explains the significant cost differences between China and the rest of the world. The selection of battery chemistry is therefore closely linked to the intended application and the required performance characteristics.

The rapid decline in battery prices, combined with continuous improvements in technology, is expected to strongly influence the future TCO of electric buses. Unlike cars, BEBs are less constrained by space for the battery pack, making battery lifetime and durability particularly important to maximize return on investment. The lifetime of a battery is generally defined as the number of cycles or years it can sustain before its capacity falls to 80% of the original value. Battery degradation is driven by internal electrochemical reactions, as well as external operational factors such as extreme temperatures.

Another important aspect concerns end-of-life management. Depending on their condition, batteries can either be recycled or reused in second-life applications, both of which have cost and environmental implications, as well as reputational effects for public transport operators.

Finally, in addition to measurable economic and environmental benefits, electric buses also offer less tangible advantages, such as improved passenger comfort due to reduced noise and vibration. These qualitative aspects, although more difficult to quantify, further enhance the overall value proposition of BEBs [2].

Chapter 3

The pantograph

3.1 Introduction

This chapter reviews the existing state of the art on the pantograph system, its operating system and its different fields of application.
In particular it explains the differences between the bus and trains application field.

3.2 The pantograph

3.2.1 Definition and Railway application

The pantograph was invented in 1879 by Walter Reichel. By definition the pantograph is a device used to power electric vehicles by an overhead contact line [19]. It is used for a railway, tram or tethered guided vehicle.

The pantograph was the development of the simple trolley pole, compared to which it has a greater capacity to remain in contact with the power line without detaching from it, even at high speeds.

The pantograph consists of an articulated system mounted on the roof of the vehicle by means of insulators and a small arch with sliders which are in direct contact with the electrical power wire or wires [20].

The interaction between the pantograph and the contact line is one of the most important aspects, as it is needed an adequate pressure on the catenary in order to guarantee a regular current collection. If a detachment occurs an electric arc could be encountered and it can cause damages to the pantograph, the contact line and the vehicle's engine. At the same time the pressure can not be too high to avoid premature wear of the material. The upper end is composed by sintered graphite and copper based sliders in order to obtain a low coefficient of friction and good electrical conductivity. Furthermore these materials allow minimal wear of the line and greater wear of themselves as their maintenance is simpler and cheaper than that of the contact line [20].

Usually the railway traction vehicles have two pantographs to prevent the train from being blocked in the event of a fault in the pantograph in use. To assure the continuity

of the service it is sufficient to exclude the faulty pantograph and replace it by using the other one [21].

The previous description refers to a railway application. In Figure 3.1 is shown the pantograph structure for a railway application.

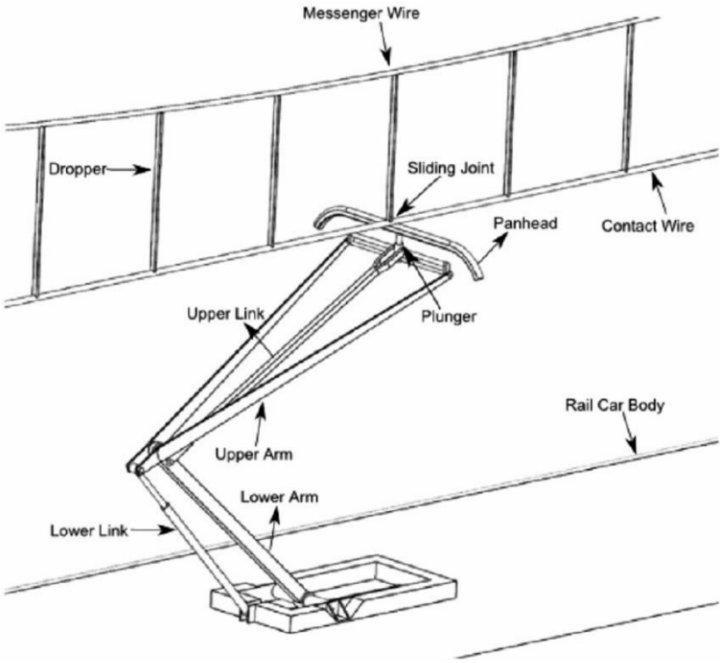

Figure 3.1: The pantograph structure for a railway application

3.2.2 Bus application and pantographs typology

The pantograph finds application also in buses field. Unlike railway, tram or any tethered guided vehicle, buses have a major flexibility of their routes and movement, so they don't receive power in a continuously way as for tethered guided vehicles, but the pantograph is only used to charge the battery during little breaks of the service.

The aim of the pantograph application is to provide a fast charge to the bus in order to assure the continuity of the service, allowing the bus to continue its service without any problem linked to the battery autonomy.

The pantograph is a ultra-fast charging system with power up to 500 kW, which allows to reach the 80% of charging in 5-8 minutes [9]. This velocity allows that the charging moments coincide with the driver's breaks between one route and the next.

Referring to the Barcelona's case and the H16 line the pantograph uses a 400 kW power and the battery charging varies between the 40% and the 80% in 5-8 minutes. Furthermore it can share its results and real-time data with the TMB control center in order to optimize the bus fleet management [22].

Basing on the main application needed there are two principal types of pantograph: pantograph up and pantograph down, also known as Inverted Pantograph [23].

- **Pantograph Up**: the moving arm is mounted on the roof of the bus and extends upward to connect with a hood.
  In this configuration, the bus carries the mobile component of the charging system. While this can increase the overall height and weight of the vehicle, the extra roof space is typically already used for components like batteries or air conditioning units.
  If a malfunction occurs, only the affected bus is impacted, and it can be replaced with a spare vehicle. Repairs can then be carried out back at the depot, in a warm, secure, and well-equipped workshop.
  Since layover operations involve fewer pantograph cycles, this can lead to potentially lower maintenance costs.
  The overhead infrastructure required is generally simpler, which can result in reduced initial investment and maintenance expenses. However, the mechanisms onboard the bus are more complex.
  A straightforward wired communication system is used: the pantograph's actuator motor is located on the bus and directly controlled by the operator [23].

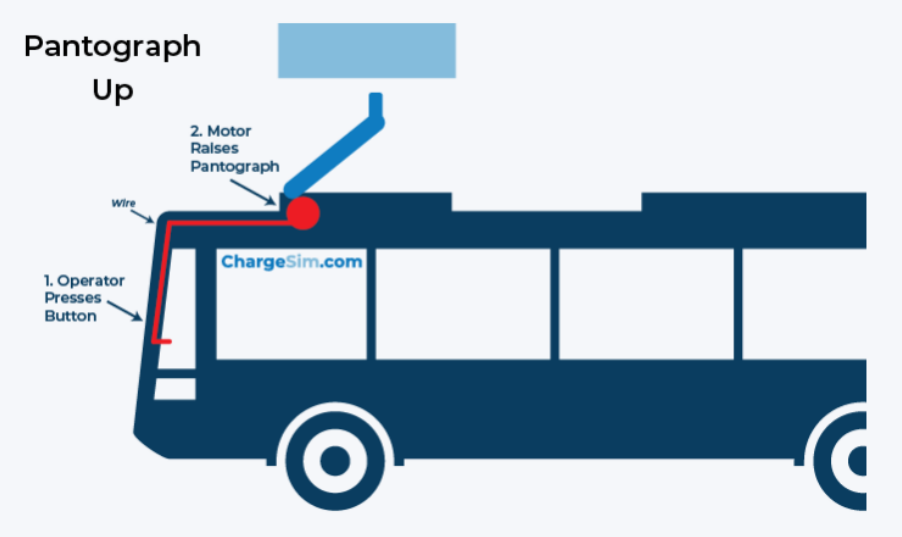

Figure 3.2: Pantograph Up

- **Pantograph Down**: in this setup, flat contact rails are installed on the bus roof, and the pantograph, which is part of the charging infrastructure, extends downward toward the bus.
  The moving component is integrated into the charging station, typically mounted on a gantry structure above the vehicle.
  This configuration reduces the weight carried by the bus and keeps its overall height lower, improving aerodynamics and potentially placing less strain on the vehicle structure.
  However, if the charging station experiences a malfunction, it can interrupt service for all buses that rely on it, potentially affecting an entire route. Repairs must be performed on-site, in varying weather conditions, and on elevated platforms.
  This design demands stronger and more expensive gantry systems to support the

heavier pantograph mechanism. On the other hand, the components installed on the bus are simpler and more cost-effective than those used in the Pantograph Up system.
Because the actuator motor is located on the charger rather than the vehicle, the bus must initiate several steps to trigger the charging process. It first establishes a Wi-Fi connection with the charger (preferably secured) and then sends a signal for the pantograph to be lowered. With multiple chargers potentially nearby, the system must ensure that the correct charger responds to the correct bus. This is achieved through an RFID positioning system, using beacons mounted on the bus. Only after verifying the bus's position and identity does the charger begin to lower the pantograph. These additional Wi-Fi and RFID communication elements, along with their controllers, significantly increase the system's complexity.
Moreover, the controller required on the charger side is an extra component compared to the Pantograph Up solution. As these systems are used exclusively for buses, they remain niche, low-volume products. This results in a limited number of charger manufacturers supporting Pantograph Down technology, along with higher costs and complexity related to the electronic components [23].

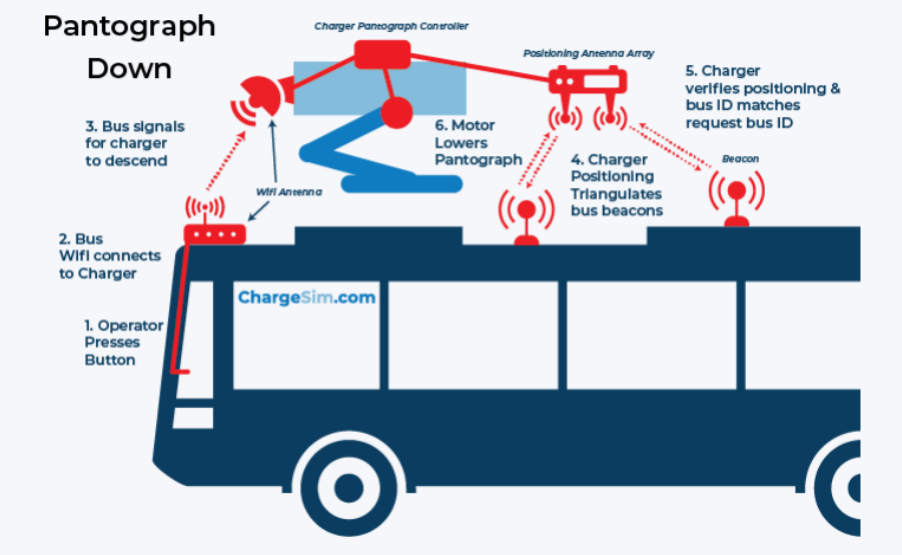

Figure 3.3: Pantograph Down

The decision between pantograph up and pantograph down setups depends on several factors, including the specific operational requirements, maintenance approach, and charging strategy of a given bus fleet.
Although pantograph up introduces greater mechanical complexity on the vehicle itself, its benefits—such as enabling maintenance to be performed at a centralized depot, limiting failures to individual buses, and avoiding reliance on Wi-Fi and positioning technologies—can outweigh the drawbacks. For these reasons the H16 line we talked about in the previous paragraphs uses a system with pantograph up.
As fleets expand, considerations like interoperability with nearby systems and the availability of suppliers also become increasingly relevant.
Transit agencies must carefully evaluate these elements to determine which configuration best fits their needs, factoring in long-term operational efficiency and the potential for

future technological developments [23].

In Figure 3.2 and Figure 3.3 it is possible to observe a simplified diagram of the Pantograph Up and Down functioning, while in the following there are some real application photos.

Figure 3.4: Pantograph Up - Real application

Figure 3.5: Pantograph Down - Real application

Chapter 4

Pantograph modeling

This chapter describes the research and modeling methods used in this thesis. It explains how I got to model the pantograph.

4.1 On-site observation

After gathering all the theoretical information regarding the functioning and applications of pantograph technology, as explained in the previous chapters, it is now possible to proceed with modeling the system.

The first step in this process is to analyze its real-world application. To this end, I conducted an on-site observation at the bus terminus to study the pantograph in operation.

This observation allowed me to gain a thorough understanding of the pantograph's functioning, most of the components involved, and the notable versatility of this technology. In particular, it was possible to appreciate the efficiency of the electric bus charging process, which takes place during the very short intervals between consecutive routes.

The following includes several photographs taken during the on-site observation, which help illustrate the operation of the pantograph and support the development of a detailed model of the system.

Figure 4.1: Pantograph's real application

Figure 4.2: Pantograph's real application

Figure 4.3: Charging infrastructure

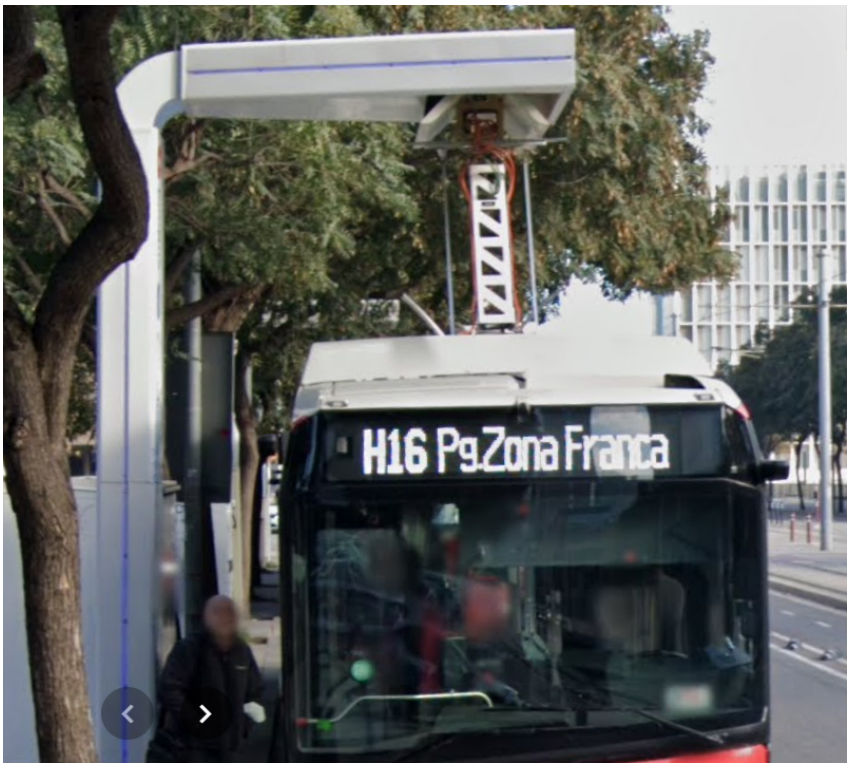

Figure 4.4: Pantograph's real application - Front view

4.2 SolidWorks modeling

Based on the information collected during the on-site observation, along with technical catalogs found online, it was possible to identify most of the components involved in this technology, as well as their approximate dimensions.

In particular, through personal assessments based on the H16 line of TMB in Barcelona and technical documentation from manufacturers such as Kempower, ABB, and IVECO, it was possible to derive the results presented below.

The main components and their analysis will be presented into detail in the following section.

The following images show the outcome of the pantograph modeling, which was carried out using SolidWorks software.

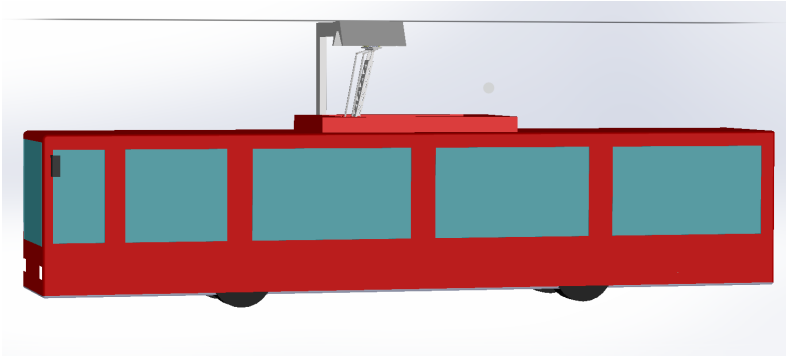

Figure 4.5: SW Modeling

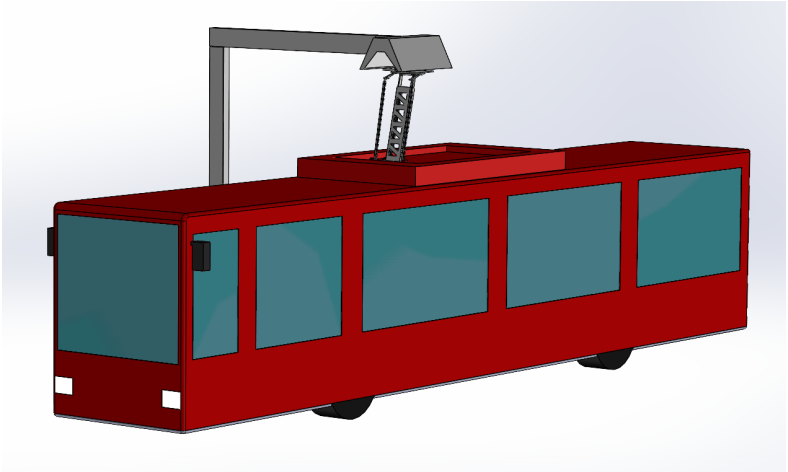

Figure 4.6: SW Modeling

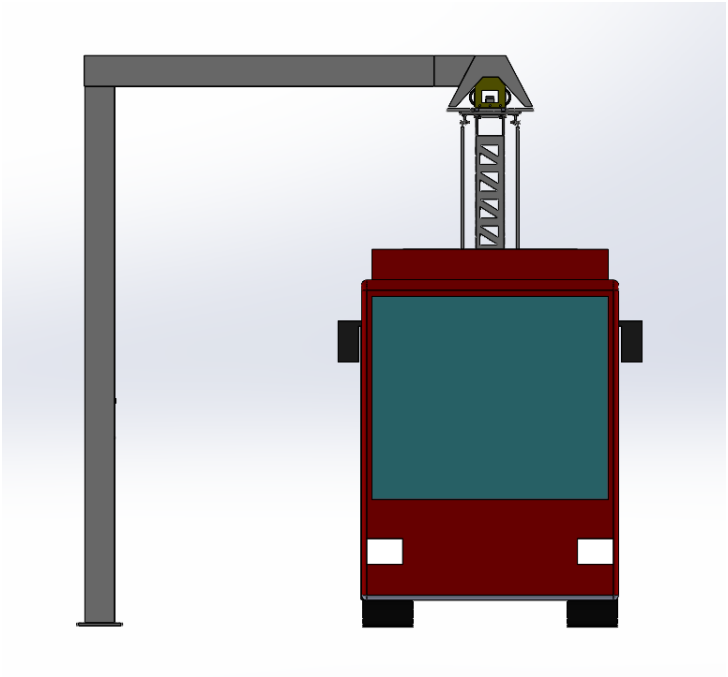

Figure 4.7: SW Modeling

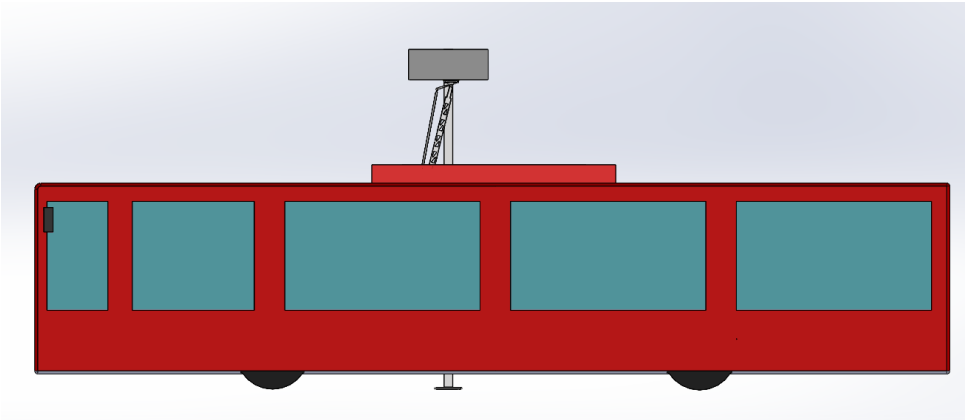

Figure 4.8: SW Modeling

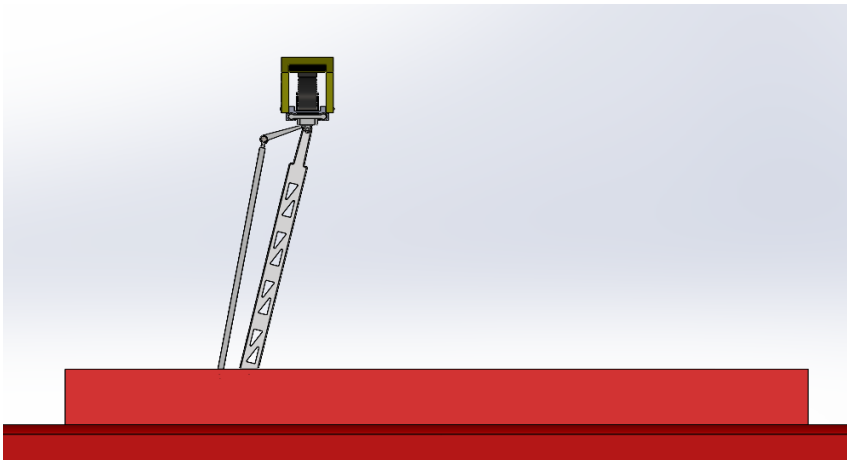

Figure 4.9: SW Modeling - Pantograph zoom

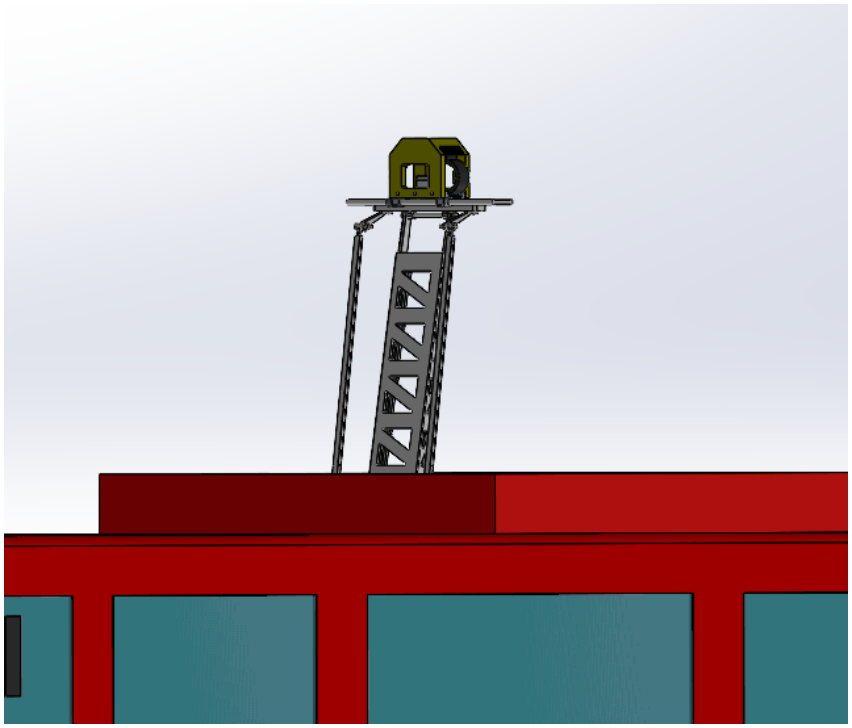

Figure 4.10: SW Modeling - Pantograph zoom

Figure 4.11: SW Modeling - Charging column

4.3 Modeling explanation

It is important to emphasize that the modeling phase includes only the mechanical moving parts, in order to simplify the modeling process.

This choice is also justified by the fact that the technology currently occupies a niche market, is not yet fully developed, and the few major manufacturers are unable to share their internal documentation due to patents and confidentiality restrictions.

In this section, only the model developed in SolidWorks and its components are analyzed, bearing in mind that several crucial elements for the complete operation of the pantograph are not included.

Based on the on-site observation and the consultation of online catalogs, I identified the main components required for mechanical moving part of the pantograph-up model.
The following table lists the primary structural components identified, excluding the electrical elements.

1. Contact head;
2. Contact plate (conductive area);
3. Lattice rod;
4. Support rod;
5. Underhead plate with electrical components;
6. Head lift actuator;
7. Lattice arm lift cylinder;
8. Support rod lift cylinder;
9. Bushing;
10. Roof bushing;
11. Connection components.

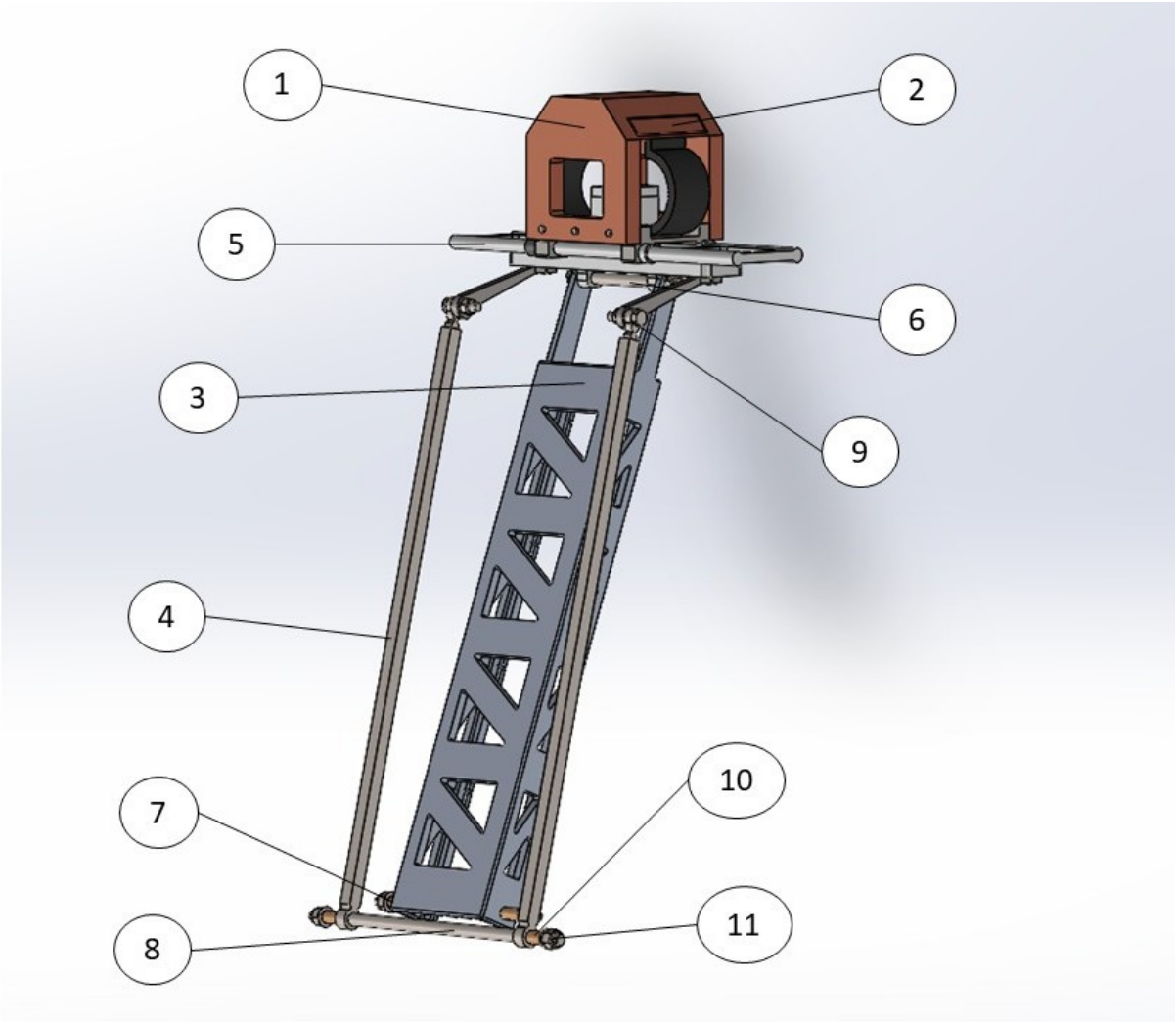

Figure 4.12: Pantograph's components

Once the main components had been identified, the next step was to assign an appropriate material to each of them.
Each material was selected based on the primary function of the corresponding component, with the aim of making the model as realistic as possible. The selection process took into account optimal performance, practical feasibility, and economic considerations.

The following table presents the material choices made for the modeling, followed by the corresponding technical justifications.

N	Component	Material	Function
1	Contact head	Copper alloy	Outer housing that protects the mechanism and guides the position of the contact system.
2	Contact plate (conductive area)	Copper alloy	Conductive contact surface, likely made of silver-coated copper (Cu-Ag), where energy transfer happens.
3	Lattice rod	Al 6061 T6	Main structural support arm, also called the reticular arm.
4	Support rod	Alloy steel	Lateral rods that stabilize movement and define kinematic motion.
5	Underhead plate with electrical components	AISI 304 Steel	Likely includes connectors, terminals, busbars, and insulators.
6	Head lift actuator	Alloy steel	Performs fine contact pressure adjustment.
7–8	Arm lift actuators	Alloy steel	Cylinders that drive the raising/lowering of the pantograph arms.
9	Bushing	Bronze	Provides guided pivoting and reduces friction.
10	Roof bushing	Bronze	Base-mounted bushing or bearing for rotational motion from the roof.
11	Connection components	Plain Carbon Steel	Bolts, pins, joints, and linkages used for mechanical connections.

Table 4.1: Material selection for each component of the pantograph system

Technical justifications

- **Contact head**: Copper alloy, as it provides electrical conductivity combined with mechanical reinforcement. For instance, it could consist of a nylon matrix filled with copper. This component is designed to maintain a contact pressure between 150–300 N.

- **Contact plate (conductive area)**: Copper alloy, chosen for its high electrical conductivity, as well as good resistance to wear and arcing.

- **Lattice rod**: Aluminum 6061-T6, selected for its excellent stiffness-to-weight ratio, good corrosion resistance, weldability, and cost-effectiveness.

- **Support rod**: Alloy steel, due to its high resistance to compression and torsion. This material provides the necessary rigidity for welded or bolted joints.

- **Underhead plate with electrical components**: AISI 304 stainless steel, offering structural rigidity, resistance to atmospheric agents, and the ability to serve as an electrical shield.

- **Head movement component**: Alloy steel, capable of withstanding frequent push–pull stresses, making it a robust and reliable material for this application.

- **Movement components**: Alloy steel, chosen for its rigidity and wear resistance. These components may require lubrication and must ensure smooth operation, with resistance to corrosion, wear, and contamination.

- **Bushing**: Bronze, selected for its low friction and self-lubricating properties, which make it ideal for slow, continuous movements with minimal maintenance requirements.

- **Roof bushing**: Bronze, for the same reasons as the main bushing—low friction, self-lubrication, and durability.

- **Connection components**: Plain carbon steel, offering good machinability and mechanical strength. It is typically galvanized to enhance corrosion resistance.

An important consideration for the design of electrical components is that all conductive areas—such as contact plates and terminals—must be structurally and electrically isolated from the supporting metallic parts.

Furthermore, it is worth noting that some material choices were made with economic considerations in mind. For instance, while certain steel components could be replaced with aluminum or titanium alloys to reduce weight, this would significantly increase production costs. In this work, I aimed to take on the perspective of a pantograph manufacturing company, striving to achieve the best possible product at the lowest feasible production cost.

4.4 Modeling analysis

Once the model has been fully realized and defined in all its components, it is possible to proceed with an analysis of the results and compare them with real-world systems to ensure that the digital prototype complies with actual standards.

In particular, it is essential that the model respects weight and strength limitations, while also satisfying the operating conditions required by the technology.

In order to validate the structural feasibility of the proposed design, a quantitative assessment of each component is carried out. The following table presents, for each component type, the estimated volume, the material density, and the resulting weight. The volume values is taken by the software SolidWorks, the density from the material choice.

Component	**Volume** $[m^3]$	**Density** $[\frac{kg}{m^3}]$	**Mass [kg]**
Contact head	0.006239	8900	55.52
Contact plate (conductive area)	0.000088	8900	0.78
Lattice rod	0.009821	2700	26.52
Support rod	0.000704	7700	5.42
Underhead plate with electrical components	0.002307	8000	18.46
Head lift actuator	0.000155	7700	1.20
Lattice arm lift cylinder	0.000248	7700	1.91
Support rod lift cylinder	0.000390	7700	3.00
Bushing	0.0000002	8800	0.002
Roof bushing	0.000001	8800	0.006
Connection components	0.000151	7800	1.18

Table 4.2: Estimated volume, density, and theoretical mass for each pantograph component.

4.4.1 Mass model validation

When validating CAD models, it is essential to check the consistency between the manually calculated mass values and those returned by the modelling software.

The deviation between these values may arise from several factors:

- Numerical rounding within the software calculations;
- Use of nominal material densities from the library, which may differ from actual values depending on composition and treatment;
- Geometric simplifications in the 3D model compared to the real component;

- Dimensional approximations due to drawing tolerances.

According to ISO 5725:2023 *(Accuracy (trueness and precision) of measurement methods and results)*, the accuracy of a measurement method should be assessed considering both systematic and random errors. In the absence of a specific standard for pantographs or for direct CAD model validation, it is reasonable to refer to good engineering practices, where a maximum tolerance of ±3% between theoretical and simulated data is commonly adopted.
If the deviation is less than 3%, the model can be considered valid with respect to its mass properties.
The percentage deviation is calculated using the following formula:

$$\frac{(M_{SW} - M_{theoretical})}{M_{theoretical}} \times 100$$

Table 4.3 reports, for each component, the theoretical mass obtained from its volume and nominal density, the mass returned by SolidWorks, and the corresponding percentage deviation.

Component	$M_{theoretical}$ **[kg]**	M_{SW} **[kg]**	**Deviation [%]**
Contact head	55.52	55.52	-2.02 e-10
Contact plate (conductive area)	0.78	0.78	-4.80 e-04
Lattice rod	26.52	26.52	-3.60 e-10
Support rod	5.42	5.42	-8.81 e-09
Underhead plate with electrical components	18.46	18.46	-1.56 e-09
Head lift actuator	1.20	1.20	-2.99 e-04
Lattice arm lift cylinder	1.91	1.91	1.78 e-08
Support rod lift cylinder	3.00	3.00	3.41 e-05
Bushing	0.002	0.002	-7.58 e-02
Roof bushing	0.006	0.006	-6.26 e-03
Connection components	1.18	1.18	4.38 e-09

Table 4.3: Mass percentage deviation for each component

It is evident that the percentage deviations between the manually calculated masses and those automatically generated by SolidWorks are limited to negligible decimal differences. All values fall well within the predetermined tolerance threshold of ±3%, in line with established engineering practice and the principles set out in ISO 5725:2023.
Consequently, the model can be considered fully compliant and valid in terms of its mass properties, and therefore reliable for proceeding with the design analysis and the dynamic validation of the system.

Total mass calculation :

In this section, the total mass of the system is calculated.
As demonstrated in the previous sections, the model has been validated; therefore, it is now possible to determine its overall mass. This process is summarized in the following table, which lists each component along with the corresponding quantity present in the system, in order to obtain the total mass of the pantograph-up assembly.

Component	**Number**	**Mass [kg]**	**Total mass** [kg]
Contact head	1	55.52	55.52
Contact plate (conductive area)	2	0.78	1.56
Lattice rod	1	26.52	26.52
Support rod	2	5.42	10.84
Underhead plate with electrical components	1	18.46	18.46
Head lift actuator	1	1.20	1.20
Lattice arm lift cylinder	1	1.91	1.91
Support rod lift cylinder	1	3.00	3.00
Bushing	2	0.002	0.004
Roof bushing	4	0.006	0.024
Connection components		1.18	1.18
Total mass			**120.2**

Table 4.4: Number of component, mass of each component and total mass of the system

As stated at the beginning of the modeling process, the calculated weight refers exclusively to the mechanical moving parts.
This means that the obtained value of 120.2 kg does not represent the mass of the entire pantograph system, but only that of its moving mechanical components.

For a more comprehensive analysis, the complete pantograph system must be considered, including actuation mechanisms, electronic components, wiring, and control systems.

All the data regarding the missing components in the model, their functions, and their respective weights have been collected from various sources, including technical sheets from Schunk Transit Systems, ABB, the TOSA project, and Siemens Mobility, as well as the ISO 15118-2, OEM data, and IEC 60529.

The following table lists the main components not included in the present model, along with a description of their role in the overall functioning of the system.

Component	**Function**
Hydraulic actuation and control group	Hydraulic pump, oil tank, valves, position sensors, and control panel.
Electronic control unit (PLC / ECU)	Controls movement, position, safety logic, and communication with the column.
Power wiring from roof to battery pack	High-voltage conductors (400–800 V DC), insulated and flexible.
CAN/Ethernet signal and communication wiring	Position sensors, safety systems, and diagnostic interface.
Position and proximity sensors	Limit switches, linear or magnetic encoders.
Structural support of the actuation group	Welded frame or profiles mounted on the bus roof.
Additional safety electrical insulators (at the head)	Dielectric elements in the head–contact area.
IP protective seals / covers	Weather protection (IP65/IP67).
Dampers and lateral guides	Gas or elastic shock absorbers to prevent violent impacts.

Table 4.5: Missing parts in the modeling of the pantograph system

An estimation of the weight of the excluded components can be performed to derive the total mass of the pantograph system.

Component	**Mass [kg]**
Hydraulic actuation and control group	15–25
Electronic control unit (PLC / ECU)	3–5
Power wiring from roof to battery pack	3–5
CAN/Ethernet signal and communication wiring	1
Position and proximity sensors	0.5
Structural support of the actuation group	5–10
Additional safety electrical insulators (at the head)	1–2
IP protective seals / covers	1
Dampers and lateral guides	2
Total mass	**51.5**

Table 4.6: Estimated mass of the missing components in the pantograph system

The data collected from the previously cited sources provided a range of weights, which vary depending on the specific application. From an engineering perspective, we adopted a conservative worst-case approach by assuming the highest possible weight for each component. This results in an estimated additional mass of 51.5 kg.

Therefore, the total mass of the pantograph system is:

$$120.2 \text{ kg} + 51.5 \text{ kg} = 171.7 \text{ kg}$$

This value should be regarded as a conservative estimate, as it may vary depending on geometry, manufacturing tolerances, or the specific materials used. Nonetheless, it is consistent with the mass range reported for real pantograph-up applications.

Chapter 5

Kinematic Analysis

In the previous chapter, a three-dimensional model of the pantograph was developed, and the materials of its main components were characterized in order to verify their mass properties. Having defined the system from a structural point of view, this chapter focuses on the kinematic behavior of the pantograph.

The purpose of this analysis is to identify the degrees of freedom, the main constraints, and the trajectory of the contact points between the pantograph head and the charging column. The study was carried out through theoretical considerations supported by numerical simulations performed on the CAD model. Specifically, the software PTC Creo was employed, importing the geometry modeled in SolidWorks, and introducing the appropriate joints to correctly reproduce the relative motion of the components.

Definition of fixed and moving components :

As a first step, the fixed components of the system were defined. The charging column was modeled as a fixed body. Similarly, the bus was considered fixed. Although the bus position is crucial for ensuring proper alignment during the charging phase, since the driver must park within a certain tolerance window, this aspect is outside the scope of the present kinematic analysis.

The study therefore concentrated on the attachment and detachment phases of the pantograph relative to the charging column. The fixed structure was then complemented by the mobile parts responsible for the pantograph's motion.

- The main (reticular) arm, which constitutes the main supporting structure of the pantograph, was connected to the bus roof through a pin joint, allowing rotation around the pin axis. This enables the lifting and lowering of the pantograph.
- The two lateral support arms were modeled in a similar manner, with the aim of stabilizing the main arm and providing controlled motion of the mechanism.
- The contact head was connected via pin joints to all three arms, enabling it to rotate and adapt its orientation to the charging column, thereby ensuring a parallel alignment of the contact surfaces.

Photographic documentation of the various modeling steps is reported in the following figures.

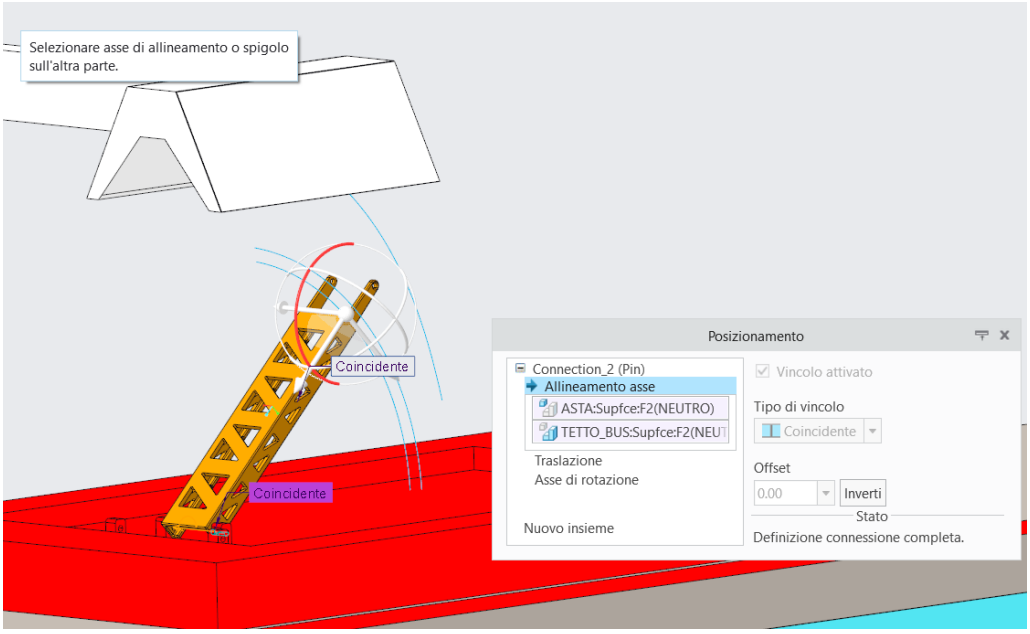

Figure 5.1: Main arm pin definition

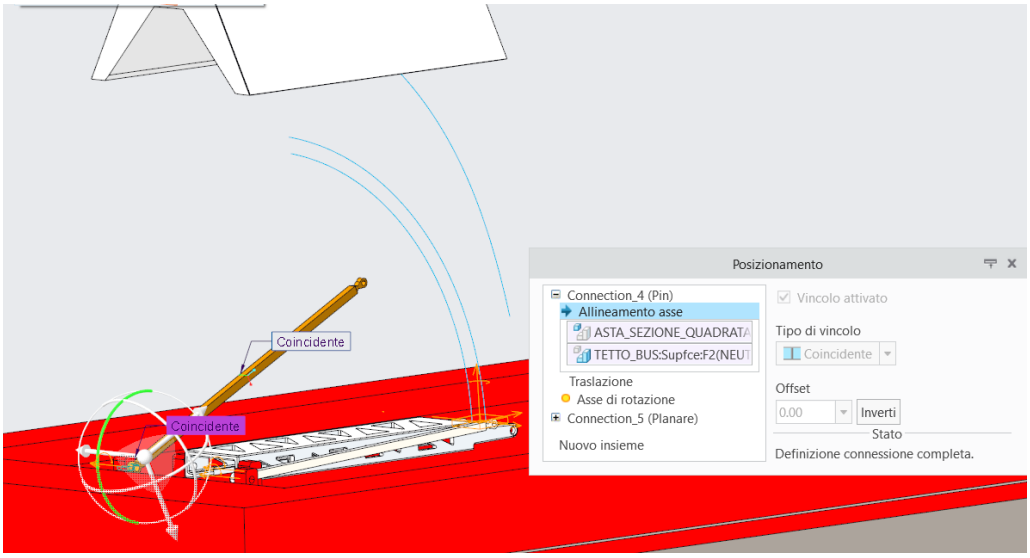

Figure 5.2: Support arms pin definition

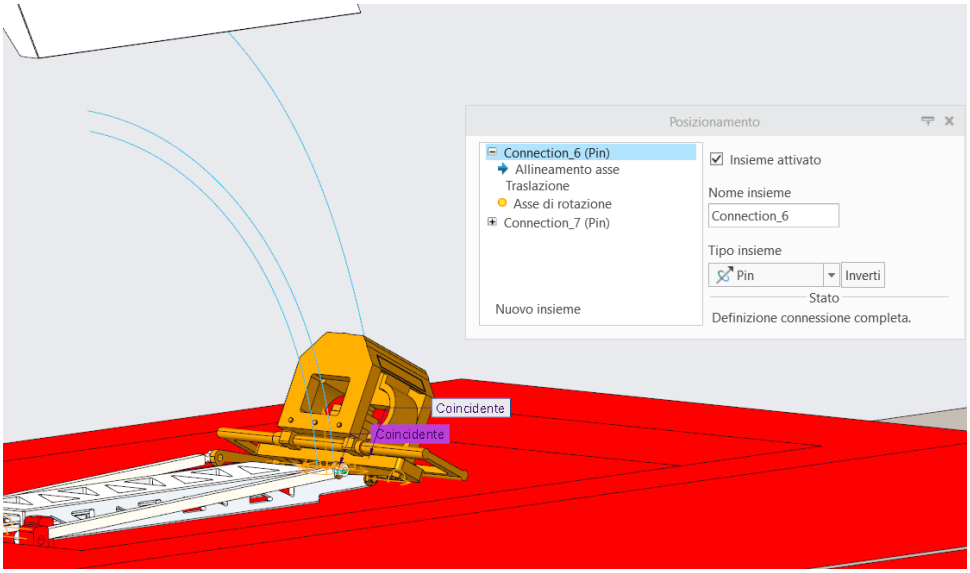

Figure 5.3: Head contact pin definition

5.1 Degrees of freedom

The pantograph mechanism can be represented as a planar articulated system composed of rigid links connected through lower revolute joints. The system mobility can be evaluated using the Kutzbach–Grübler criterion for planar mechanisms, which is expressed as:

$$N_{dof} = 3 \cdot (n - 1) - 2j_1 - j_2$$

where:

- N_{dof}: the number of independent degrees of freedom, which defines the mobility of the mechanism;
- n: the number of mobile members of the mechanism;
- j_1: number of joints with 1 free degree of freedom;
- j_2: number of joints with 2 free degree of freedom.

The pantograph system can be modeled as:

1. Head contact
2. Main arm
3. Support bar 1
4. Support bar 2

Thus, $n = 4$, as the mechanism is composed by 4 moving links.

For the evaluation of j_1, we identified 4 revolute joints:

1. Main arm to the bus roof;

2. Main arm to the head contact;
3. Support bars to the bus roof;
4. Support bars to the contact head.

Since the two support bars are symmetrical and connected to the same lower link, their motion can be considered as that of a single body, which gives:

$$j_1 = 4$$

No joints with two degrees of freedom are present, hence:

$$j_2 = 0$$

Therefore, the number of degrees of freedom is:

$$N_{dof} = 3 \cdot (n-1) - 2j_1 - j_2 = 3 \cdot (4-1) - 2 \cdot 4 = 1$$

As expected, the system allows only 1 independent motion, corresponding to the lifting motion of the main arm.
Through the movement of the main arm, provided by a rotational motor, and by geometric constraints, the contact head can reach the parallel alignment with the charging plate of the charging column.

Hence, the pantograph mechanism can be considered as a 1-DoF system, driven by the rotational motion of the main arm with respect to the bus roof. The passive motions (such as the rotation of the contact head) are kinematically dependent on this input motion and do not require additional actuators.

5.2 Actuation and Motion Law

After defining the constraints, a driving element was introduced. A rotational servomotor was applied at the joint between the main arm and the bus roof. To reproduce realistic motion, a cosine-based motion law was selected, which reflects the cyclic nature of the raising and lowering phases.

The charging and resting phases of the mechanism were neglected, as they correspond to static conditions where the system remains stationary and thus are not relevant for the present kinematic investigation.

Furthermore, for the law definition in the software there were limited options and the cosine-based one was the best possible. PTC Creo cosine equation usable was of the form:

$$\theta(t) = A \cdot cos(360 \cdot \frac{t}{T} + B) + C$$

The limits angles were 0°, the initial position, and 76.3°, which corresponds to the contact angle. From these values it was easy to calculate the different equation parameters:

- $A = 38.15°$

- $B = 0$
- $C = -38.15°$

It is chosen a period T of 10 seconds, assuming 5 second for the raising phase and 5 s for the lowering one.
The actual law of the motor is:

$$\theta(t) = 38.15 \cdot cos(360 \cdot \frac{t}{10}) - 38.15$$

5.3 Kinematic measurements and reference systems

For the analysis, the motion of a point on the contact head was selected. Specifically, one corner of the contact plates was tracked; however, since the head behaves as a rigid body, the results would be equivalent for any other point on the head.

To accurately describe the interaction with the charging column, an auxiliary reference system was defined on the surface of the column's contact plate. In this way:

- the z-component represents the displacement normal to the contact surface (with $z = 0$ indicating contact), and its velocity and acceleration correspond to the normal kinematic components, directly linked to the contact force;
- the x- and y-components represent the tangential motion, which is related to friction and wear phenomena at the interface.

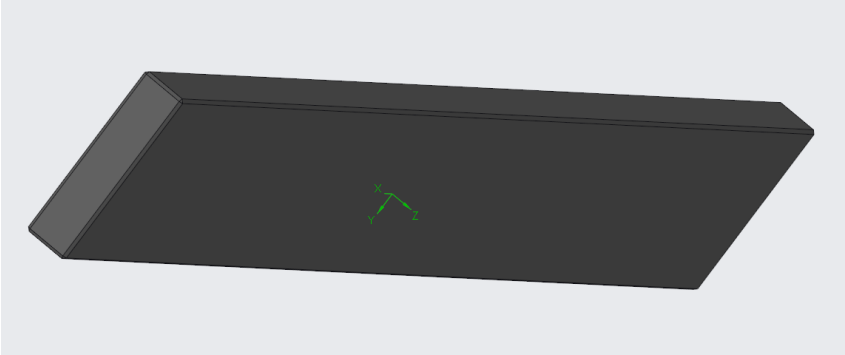

Figure 5.4: Contact plate's reference system

5.4 Results and discussion

The results of the kinematic analysis are presented in the following graphs, which show the displacement, velocity, and acceleration of the selected point.

5.4.1 Angular quantities

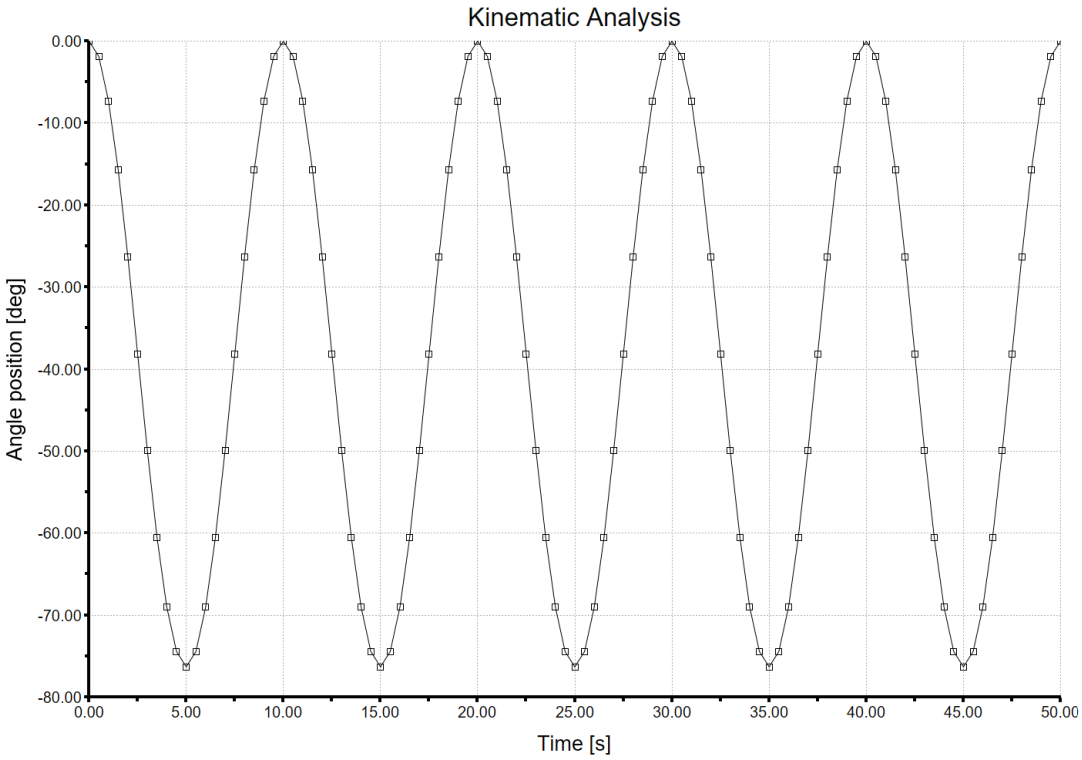

Figure 5.5: Angle Position

The plot verifies that the main (driving) arm correctly follows the commanded motion law imposed by the servomotor. The angular law used in the simulation is

$$\theta(t) = 38.15 \cdot cos(360 \cdot \frac{t}{10}) - 38.15$$

where t is time in seconds and θ is in [deg].
This expression yields $\theta_{max} = 0°$ (when $cos = 1$) and $\theta_{min} = -76.3°$ (when $cos = -1$); the negative sign results from the adopted reference system in the CAD environment. In physical terms the arm sweeps between 0° (rest position) and 76.3° (fully raised position). These bounds coincide with the motion limits imposed on the revolute joint during assembly in PTC Creo.
The figure therefore confirms both the correct implementation of the cosine motion law and the respect of the assembly limits (0° and 76.3°) during the simulated lift/lower cycle.

We can explicit the expression in rad/s:

- A = 38.15° $\cdot \frac{\pi}{180} = 0.6658$ rad

- $\omega = \frac{2\pi}{T} = \frac{2\pi}{10} = 0.6283$ rad/s

$$\theta(t) = 0.6658 \cdot cos(0.6283 \cdot t) - 0.6658$$

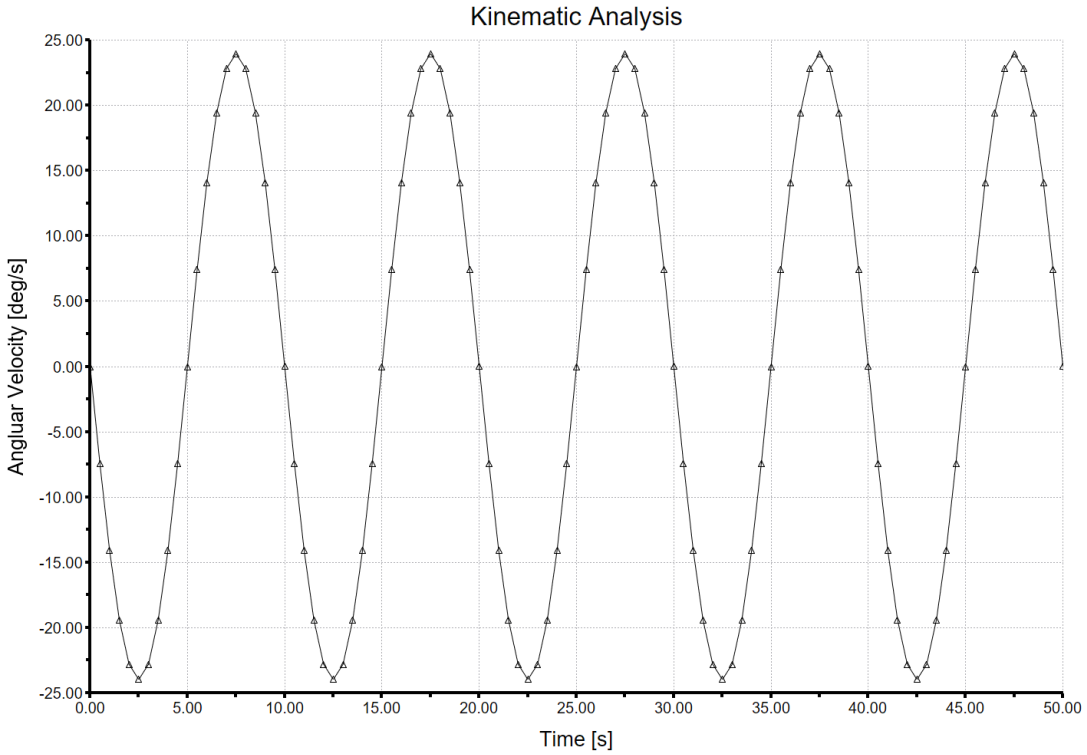

Figure 5.6: Angular velocity

The angular velocity shown in the plot is derived analytically from the commanded motion law. The analytical derivative yields

$$\dot{\theta} = -0.4183 \cdot sin(0.6283 \cdot t)$$

By evaluating the expression at $t = 2.5s$, where $sin = 1$, we have the velocity maximum value.

$$\dot{\theta}(t) = -0.4183 \left[\frac{\text{rad}}{\text{s}}\right] = -23.97 \left[\frac{\text{deg}}{\text{s}}\right]$$

The value obtained is in perfect agreement with the maximum and minimum amplitudes displayed in the plot, confirming both the correctness of the analytical expression and the unit convention adopted by the software.

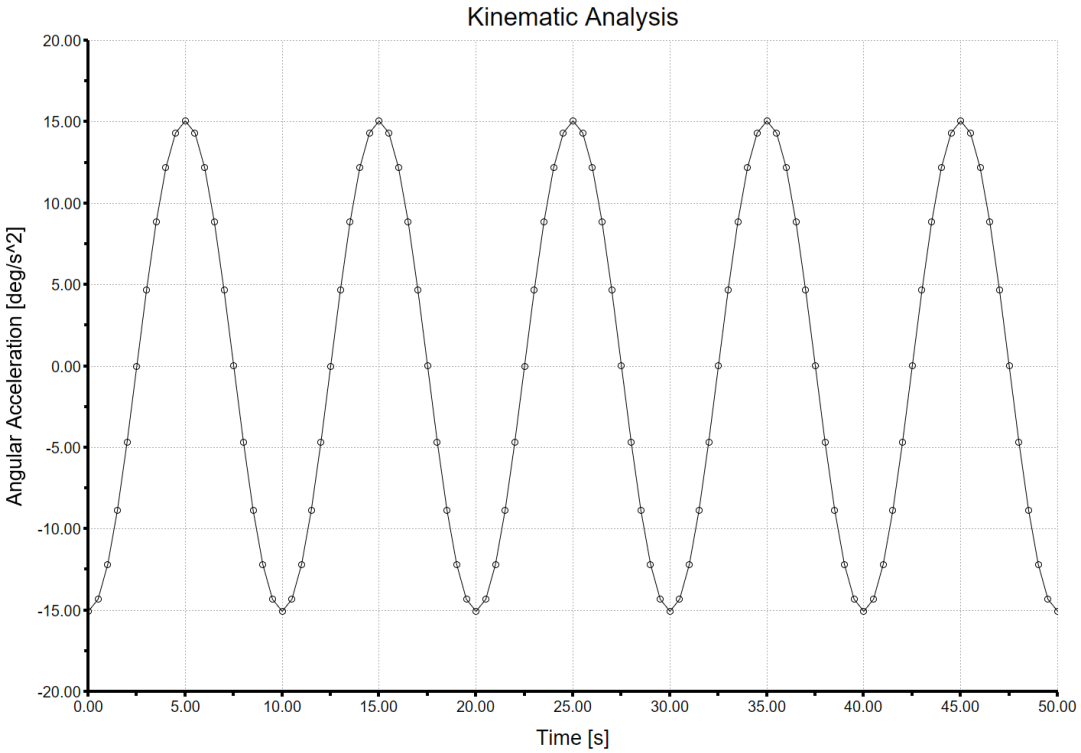

Figure 5.7: Angular acceleration

By further differentiating the angular velocity, we obtain the angular acceleration of the mechanism:

$$\frac{d\dot{\theta}}{dt} = \frac{d}{dt}\Big(-0.4183 \cdot \sin(0.6283 \cdot t)\Big)$$

$$\ddot{\theta}(t) = 0.4183 \cdot 0.6283 \cdot \cos(0.6283 \cdot t) = -0.2628 \cdot \cos(0.6283 \cdot t) \left[\frac{\text{rad}}{\text{s}^2}\right]$$

The angular acceleration follows a cosine law with an amplitude of approximately 0.2628 rad/s^2 = 15.06 deg/s^2. As expected, it reaches its maximum absolute values at the beginning and at the end of the lifting and lowering motion, where the angular velocity changes most rapidly. Conversely, the acceleration tends to zero at mid-stroke, corresponding to the maximum velocity of the mechanism. This behavior is consistent with the cyclic operation of the pantograph: higher torque is required from the actuator during the initial engagement and the final release phases, while the central portion of the trajectory exhibits smoother motion.

5.4.2 Contact Head's Position

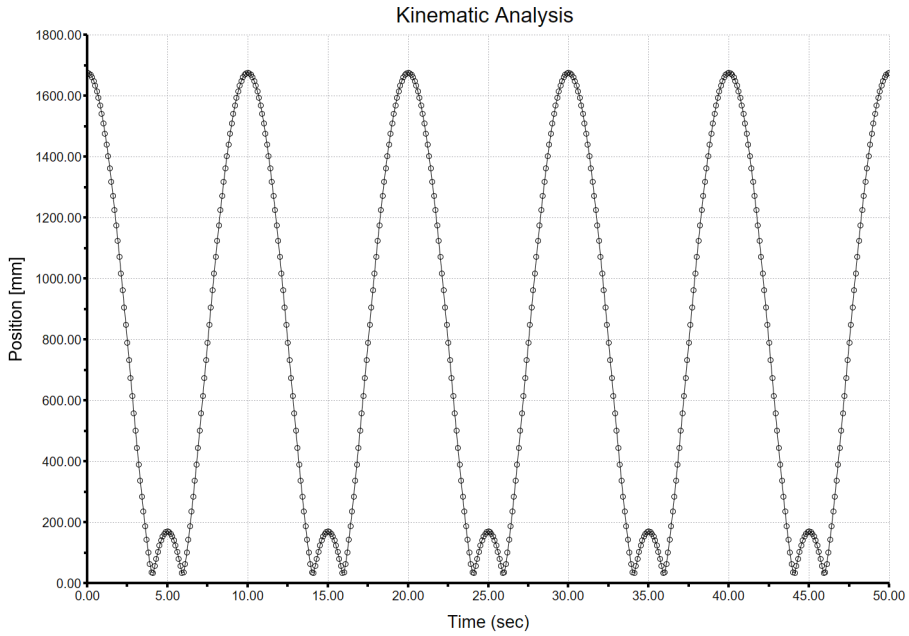

Figure 5.8: Contact Head's Position

The absolute position of the monitored point on the contact head shows a predominantly cyclic trend, moving from its initial elevation of approximately 1675 mm down to the minimum of about 35 mm at 4 s, before rising slightly to 170 mm around 5 s, and then returning to 35 mm at 6 s. Finally, the trajectory rises again to the initial height of about 1675 mm at the end of the cycle.

It is important to remark that these values do not represent the absolute displacement of the pantograph head with respect to the bus roof, but rather the distance of a specific vertex of the contact plate from the auxiliary reference system. This reference system was placed at the center of the counterpart plate located on the charging column. As a result, the monitored point starts from a distance of about 1675 mm, which simply corresponds to the initial spacing between the two components in the rest configuration.

The small intermediate increase around 5 s is not an anomaly, but rather a consequence of the kinematic chain: the non-linear interaction between the lattice arm, the supporting links, and the rotational degree of freedom of the contact head induces a local rebound in the trajectory. This effect ensures that the head surfaces remain correctly aligned with the charging column, even though the monitored vertex does not follow a strictly monotonic path.

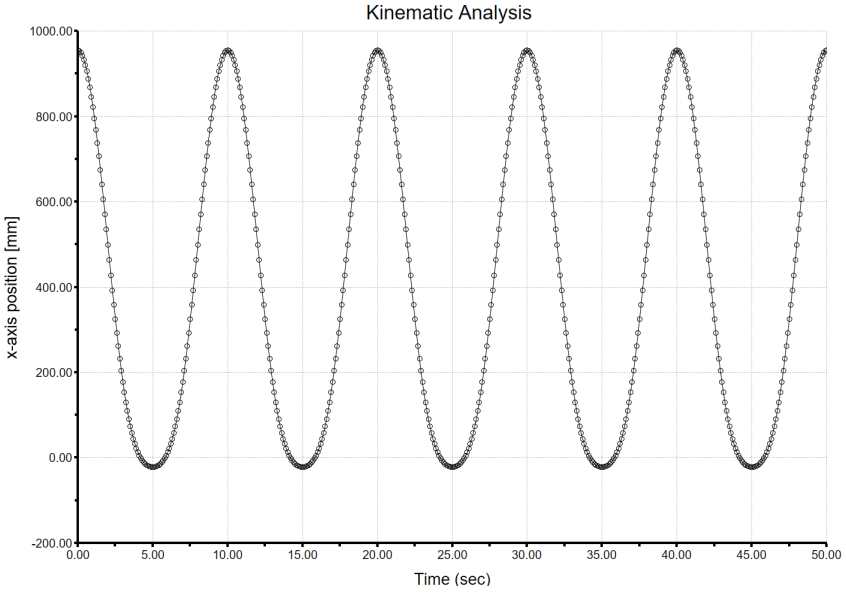

(a) X Position

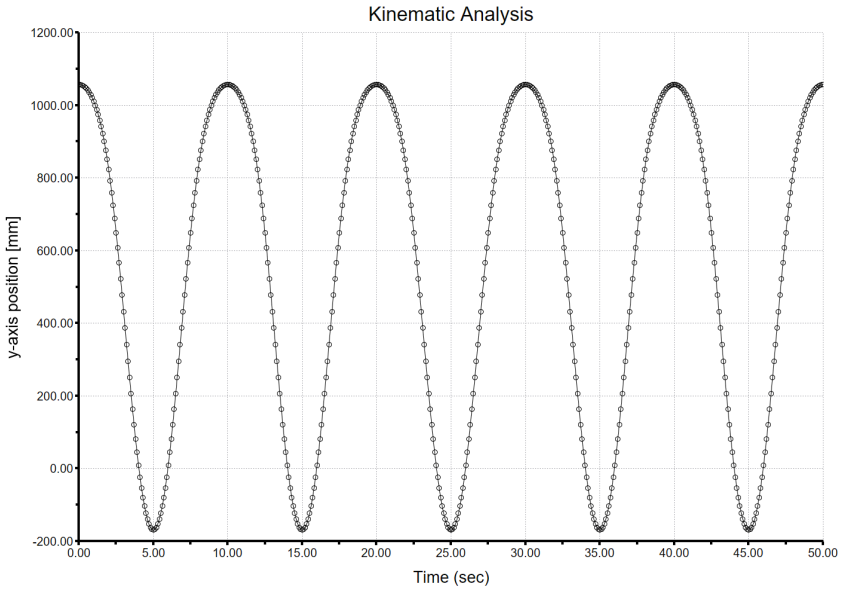

(b) Y Position

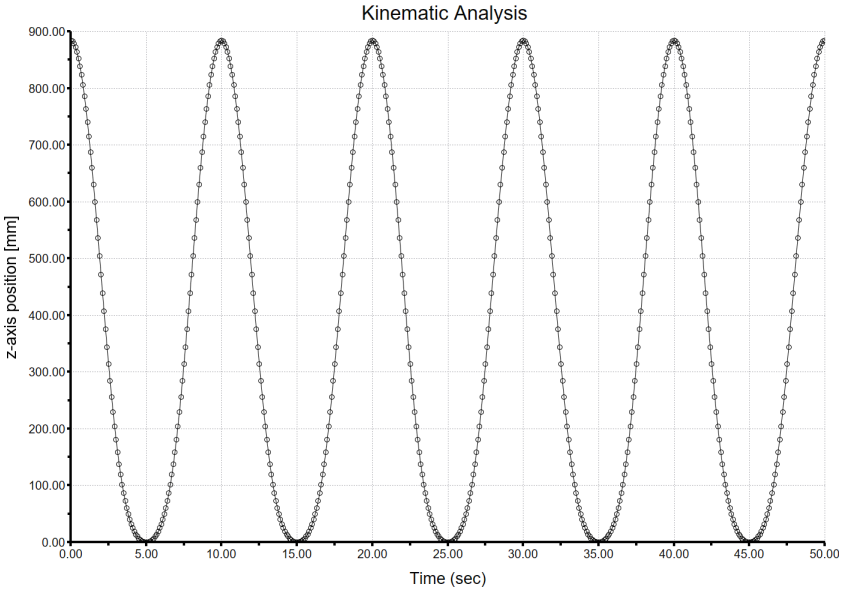

(c) Z Position

Figure 5.9: Position components of the contact head along x, y, and z.

The X- and Y-components of the position exhibit harmonic behavior, starting from 955 mm and 1057 mm respectively, and returning to their initial values at the end of the cycle. Their values depend solely on the arbitrary choice of the monitored vertex on the contact plate, and therefore have no direct functional meaning. However, their harmonic nature confirms the consistency of the imposed motion law and the kinematic modeling.

The Z-component of the position is of primary importance, as it represents the normal distance between the contact head and the charging column. The trajectory starts from approximately 885 mm, decreases to zero at t = 5 s (corresponding to the instant of contact between the two surfaces), and returns to 885 mm at the end of the cycle. This curve directly identifies the engagement and disengagement phases of the pantograph, confirming the correct operation of the mechanism. It should be noted that, in the present study, the pantograph immediately descends after reaching contact, whereas in a real charging process it would remain at $z = 0$ for a certain time corresponding to the effective duration of the energy transfer.

5.4.3 Contact Head's Velocity

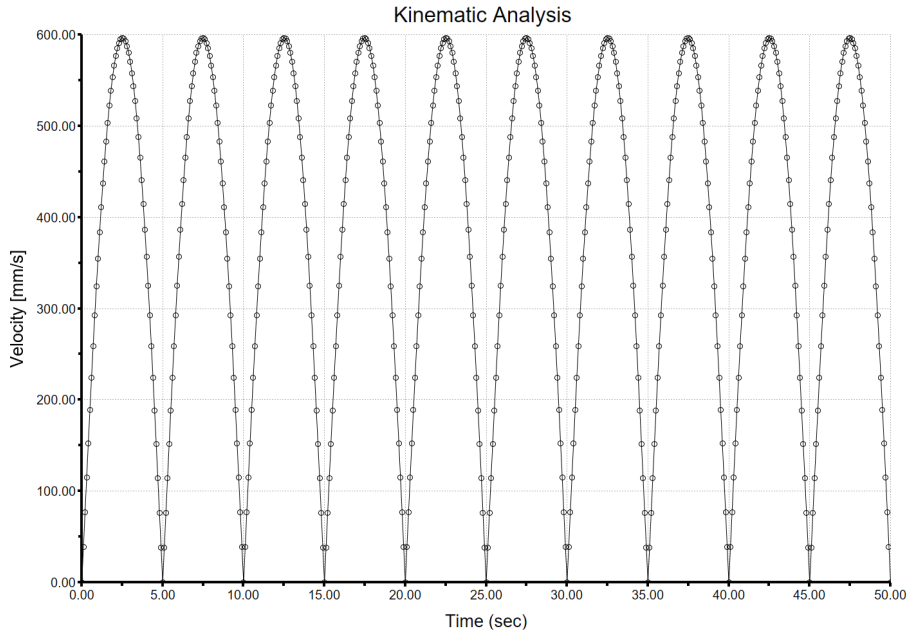

Figure 5.10: Contact Head's Velocity

The absolute velocity of the monitored vertex exhibits a periodic sequence of parabolic trends, starting from zero, increasing to a maximum value of approximately 600 mm/s, and returning to zero within half a cycle. Each complete period therefore contains two identical branches with concavity directed downwards. This behavior reflects the cyclic nature of the lifting and lowering motion, where the velocity peaks at halfway and goes to zero at the initial and final configurations.

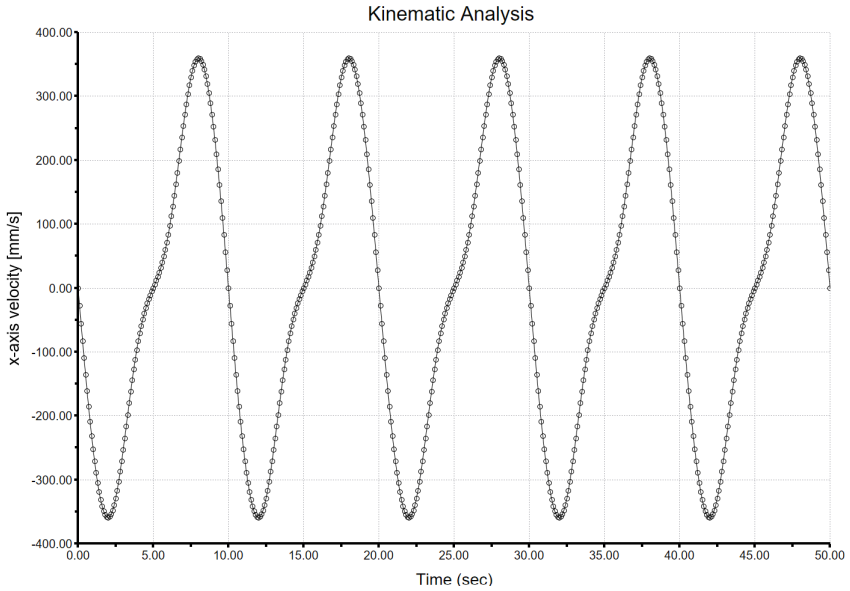

(a) X Velocity

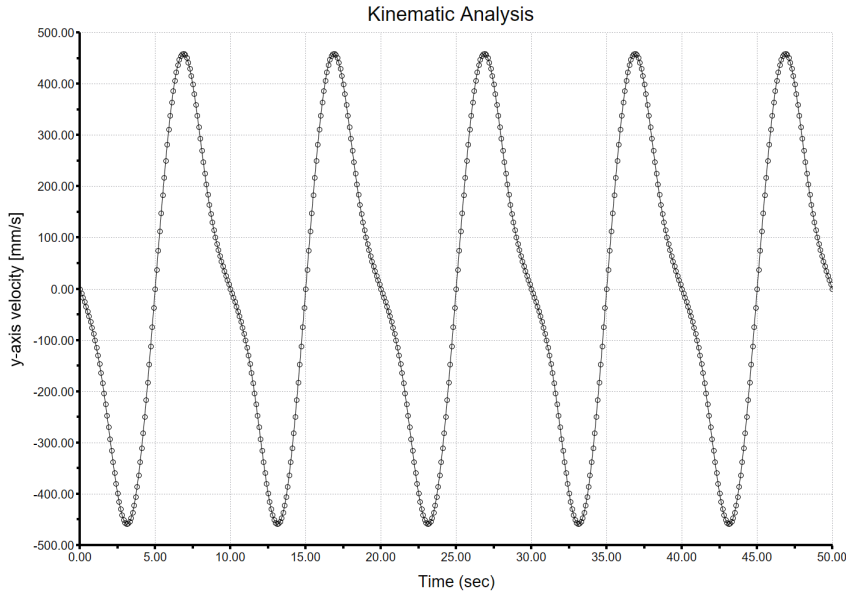

(b) Y Velocity

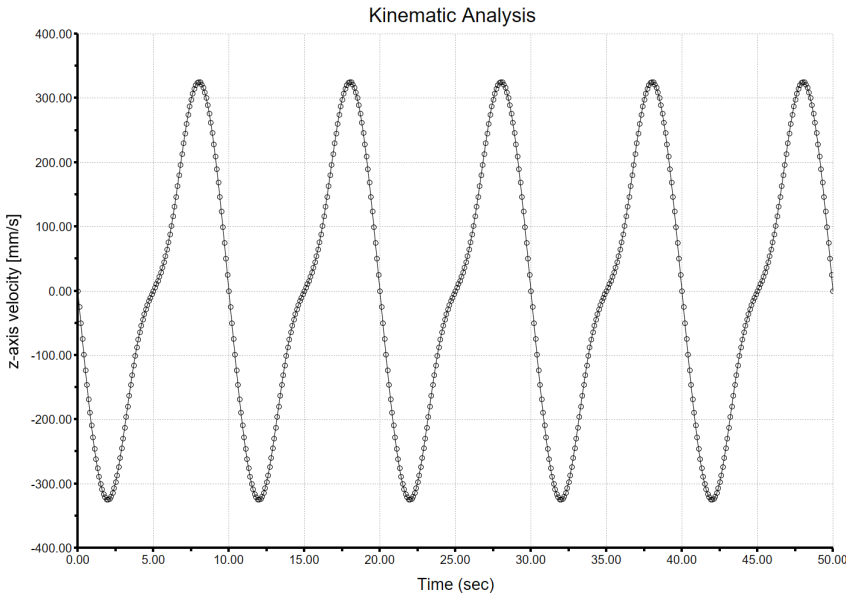

(c) Z Velocity

Figure 5.11: Velocity components of the contact head along x, y, and z.

It can be observed in the following page that the X, Y, and Z velocity components are not perfectly sinusoidal. This deviation is expected, as the point under investigation is not undergoing a simple harmonic motion, but rather the result of the combined kinematics of the pantograph's linkages. The non-linear constraints of the mechanism, together with the specific choice of the monitored vertex, lead to slight departures from ideal sinusoidal trends. Nevertheless, the periodicity and symmetry of the curves confirm the consistency of the imposed motion.
The velocity components along X and Y confirm the harmonic nature of the imposed motion.
The X-component shows alternating parabolic segments, with a negative peak of about -360 mm/s during the first half-period and a symmetric positive peak of 360 mm/s during the second half-period. The Y-component follows a similar pattern, with extrema of approximately –460 mm/s and +460 mm/s.
It is worth noting that these components depend on the arbitrary choice of the monitored vertex on the contact plate; therefore, while their exact values lack direct functional meaning, their trends are consistent with the kinematics of the system.

The Z-component of velocity is more meaningful, since it describes the approaching and separation speed between the pantograph head and the charging plate. The profile alternates between maximum positive and negative values of about ±325 mm/s, with zero crossings at the initial, contact, and final instants. This information is directly related to the effectiveness of the engagement and disengagement phases, as the magnitude of the vertical velocity governs the smoothness of the impact and release during operation.

We calculated the tangential component of the velocity v_{xy} as:

$$v_{xy} = v_t = \sqrt{v_x^2 + v_y^2}$$

and we obtained the following graph:

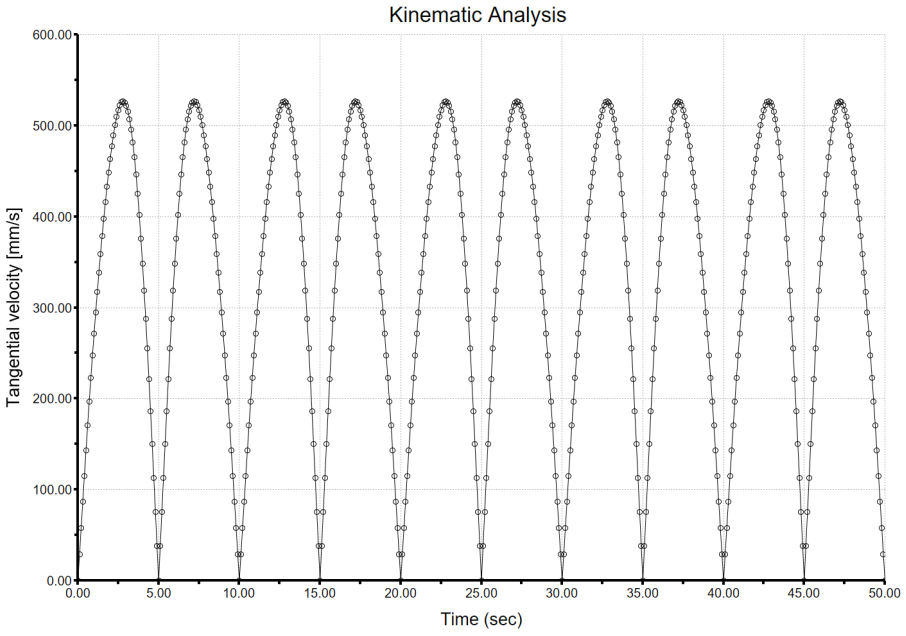

Figure 5.12: Tangential Velocity on XY-plane

The tangential velocity in the XY plane shows a trend that is practically identical to the absolute velocity, with the same parabolic-like envelope and periodicity. The only difference is in the peak value, which reaches approximately 525 mm/s instead of 600 mm/s. This reduction is expected, since the XY velocity is obtained by neglecting the vertical (Z) component of motion. The comparison confirms that the major contribution to the overall velocity is given by the in-plane displacement, while the out-of-plane component accounts for the difference between the two curves.

Calculating the tangential velocity on the XY plane is particularly important for analyzing friction and wear phenomena at the contact interface, as these are primarily influenced by the relative motion in the plane of contact.

5.4.4 Contact Head's Acceleration

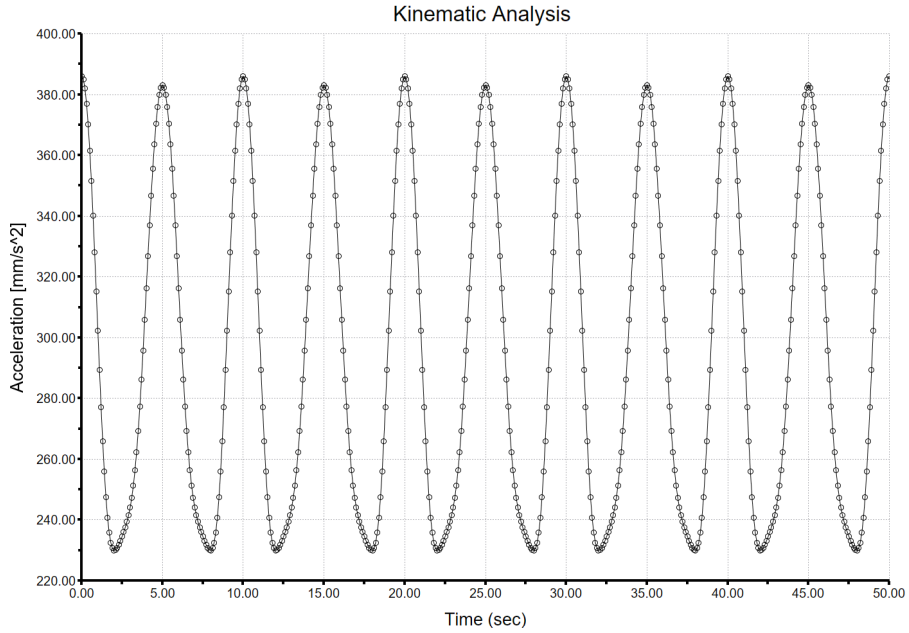

Figure 5.13: Contact Head's Acceleration

The behavior is periodic, with oscillations ranging from approximately 230 mm/s^2 to 386 mm/s^2. The curve has a harmonic nature, consistent with the imposed trajectory, but with a constant positive component that prevents the curve from oscillating around zero. This is because the total acceleration values are always positive, regardless of the sign of the components along the individual axes. In fact, it is obtained from:

$$a = \sqrt{a_x^2 + a_y^2 + a_z^2}$$

The behavior confirms that the analyzed point, and the contact head in general, is subjected to acceleration and deceleration cycles related to the pantograph's raising and lowering motion. It is worth noting that the shape is not perfectly sinusoidal.

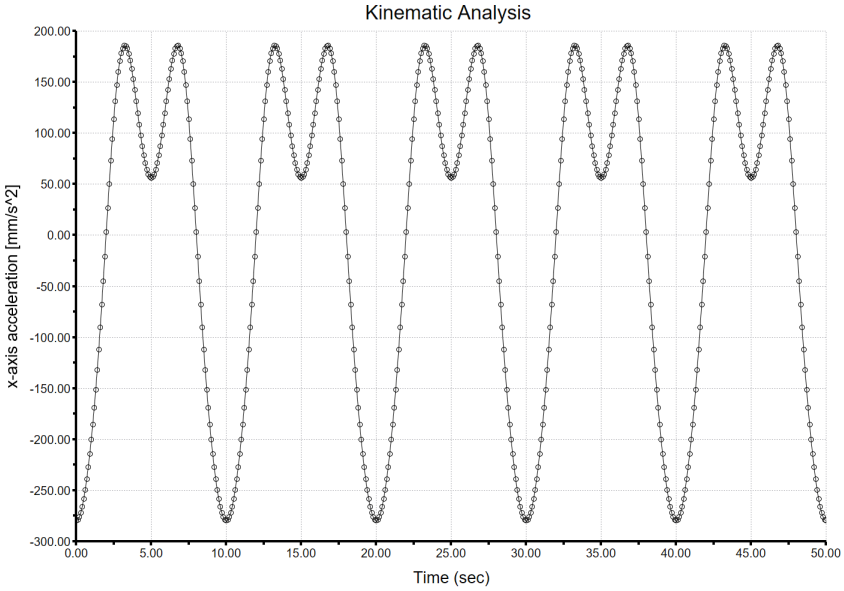

(a) X Acceleration

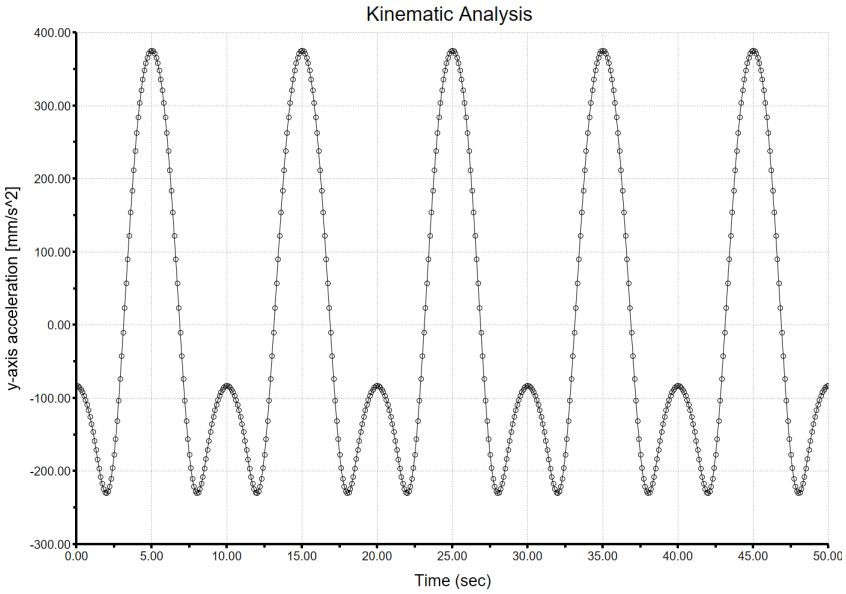

(b) Y Acceleration

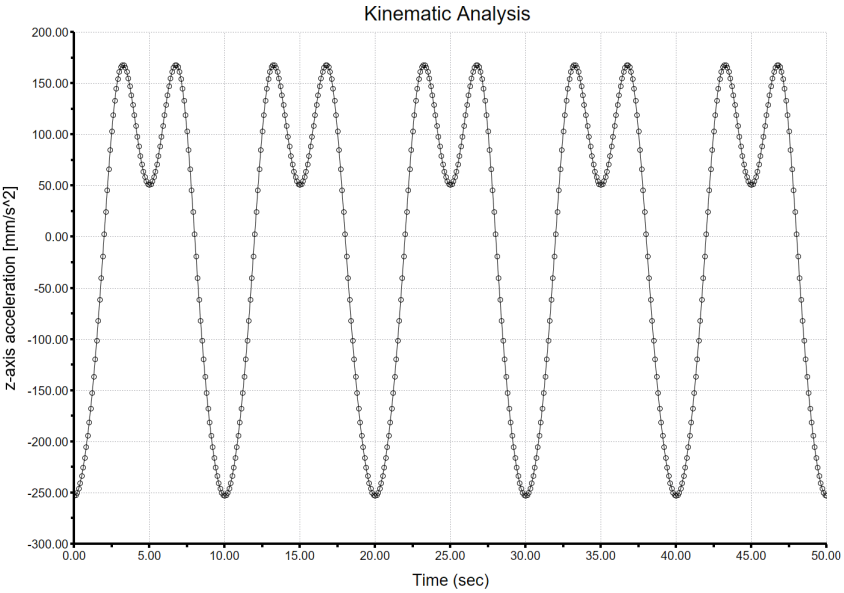

(c) Z Acceleration

Figure 5.14: Acceleration components of the contact head along x, y, and z.

The X component of the acceleration begins around –280 mm/s^2, climbs to a local maximum of about +185 mm/s^2, then drops to a positive valley of +55 mm/s^2 at the contact event. The pattern then repeats itself: it rises again to +185 mm/s^2 and finally returns to –280 mm/s^2 by the end of the cycle.
The Y component starts near –83 mm/s^2, decreases to about –229 mm/s^2, and then peaks at approximately +375 mm/s^2 at contact. Afterwards it repeats the same trend, falling back to –229 mm/s^2 and finally returning close to the initial –83 mm/s^2.

They exhibit periodic yet non-sinusoidal oscillations: the lobes are asymmetric and include contact-aligned shoulders. This distortion is consistent with the nonlinear kinematics of the pantograph and with evaluating an off-center point on the contact plate. Notably, the largest contact-synchronous acceleration occurs along Y.

The Z component mirrors the qualitative shape of the X component but with different magnitudes. It ranges from about –253 mm/s^2 to +168 mm/s^2, shows a shallow valley near +50 mm/s^2 at contact, rises again toward +168 mm/s^2, and closes the cycle back near –253 mm/s^2.

The Z component describes the motion along the normal to the charging plate. Peak magnitudes occur during the fastest approach/separation phases. The sign of these peaks depends on the adopted axis orientation.

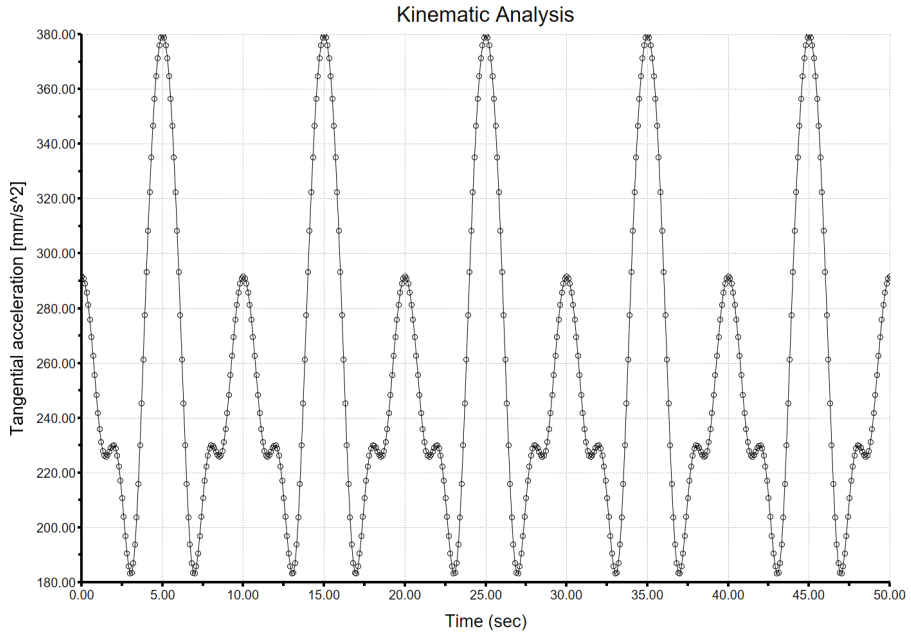

Figure 5.15: Tangential Acceleration on XY-plane

The tangential acceleration along XY plane is defined as:

$$a = \sqrt{a_x^2 + a_y^2}$$

It can be also obtained by the difference between the absolute acceleration and the normal acceleration (the Z-component). The maximum occur at the instants of contact, when the pantograph undergoes the highest tangential forces on the contact surface.

Chapter 6

Dynamic Analysis

Building on the kinematic analysis, this chapter quantifies the mechanical actions that drive the pantograph-up system during the raising, contact, and lowering phases. Specifically, we determine:

- the torque required at the actuator and the associated instantaneous power;
- the normal contact force $F_n(t)$ needed to ensure a reliable electrical connection (target order of 150–300 N);
- the constraint reactions at the main pins (in-plane radial forces F_r and bending moments M_r; axial components F_a, M_a about the pin axis).

The objective is to verify correct operation under realistic loading and to provide design-relevant quantities for actuator sizing and joint verification.

6.1 Introduction: assumptions and limitations

The pantograph is modelled as a planar, single-DOF rigid-body mechanism mounted on the bus roof and driven by a rotary actuator at the reticular (main) link–roof joint.

Owing to geometric symmetry, half of the mechanism is analysed; the mirrored half experiences equivalent loads.
The bus roof and the charging column are treated as ground. Gravity is included.

Because all applied loads lie in the plane of motion, the axial reactions along the pin axes (F_a, M_a) are expected to be negligible relative to the in-plane components; this will be shown explicitly in the results.

The mechanism is driven by the cosine law presented in the previous chapter, which ensures near-zero angular velocity at the contact instant ($t = 5s$), mitigating impulsive effects and enabling a quasi static interpretation of the contact distribution. The steady dwell at the upper (charging) position is not simulated; instead, the contact is modeled as a short, smooth window centered at $t = 5s$ (end of raising, start of lowering), under the simplifying assumption of quasi-static stability and essentially constant force during

an actual dwell. A consequence is that the power at contact is modest (angular speed near 0), while the torque increment due to contact is captured with

$$T_{contact}(t) = F_n(t) \cdot r_{eff}(t)$$

This study relies on a set of modeling choices and tool constraints, chiefly imposed by the available version of PTC Creo.

Surface-to-surface 3D contact between the column face and the pantograph head could not be solved robustly in the software. The interaction was therefore represented by an equivalent normal force, implemented through four spring–damper pairs connecting arbitrary, corresponding points on the head and on the column at the "up" pose. Each pair becomes active when the clearance falls below 0.5 mm and acts in compression only. This surrogate captures the time history and order of magnitude of the resultant normal force $F_n(t)$ required for charging, but it does not reproduce the local pressure distribution, tangential friction, or microslip at the interface.

For this reason, results were obtained by combining:

- a baseline simulation with gravity and inertia only;
- (ii) a contact window (0.10 s around the event, precisely [4.95 s; 5.05 s]) where a smoothly windowed $F_n(t)$ was applied on the contact patch.

Although smooth profiles and careful alignment were used to minimise numerical artefacts, small residual spikes near the window edges may remain and are interpreted as non-physical.

6.2 Contact Force

As outlined above, the head–column interaction was represented by a mechanical surrogate consisting of four spring–damper pairs acting between corresponding points on the contact head and on the charging column. Each pair is oriented along the local contact normal and is active in compression only.

The contact time window was identified as [4.95, 5.05]s. A dedicated motion analysis was run with a time step $\Delta t = 1ms$, logging at each instant the elastic forces of the four springs and the viscous forces of the four dampers.

The pointwise contribution to the normal force is then

$$F_{n,i}(t) = F_{k,i}(t) + F_{c,i}(t) = k_i \cdot \delta(t) + c_i \cdot \dot{\delta}(t)$$

where k_i and c_i are the stiffness and damping assigned to the i-th pair. In the system they have the following values:

$$k_i = 64.5 \frac{N}{mm}$$

$$c_i = 0.055 \frac{N \cdot s}{mm}$$

The resultant contact force is obtained as:

$$F_n(t) = \sum_{i=1}^{4} F_{n,i}(t)$$

Two plots are reported.

1. Over the full cycle (0–10 s), $F_n(t)$ is identically zero except in the contact window, where a single, localized peak appears.

2. a zoom on [4.95 , 5.05] s shows the detailed time history; as expected, the maximum occurs at t=5s, with

$$F_{n,max} = 240.1N$$

   As previously said, in our simplification, we imagine that during all the contact this force remains constant. This value lies within the expected operational range for pantograph charging (typically 150–300 N, with upper bounds reported up to 600 N), in line with the references discussed earlier [24], [25].
   This confirms that the adopted surrogate produces a realistic contact load for the subsequent torque and joint-reaction analyses.

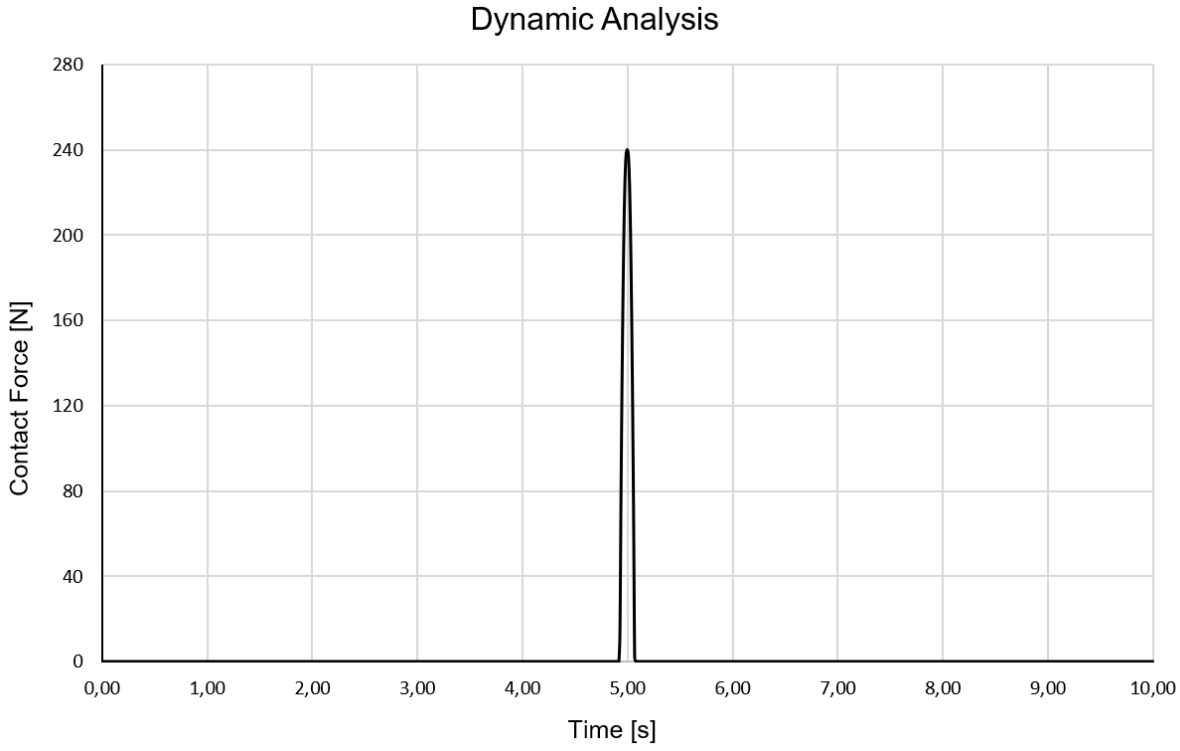

Figure 6.1: Contact Force over the full cycle

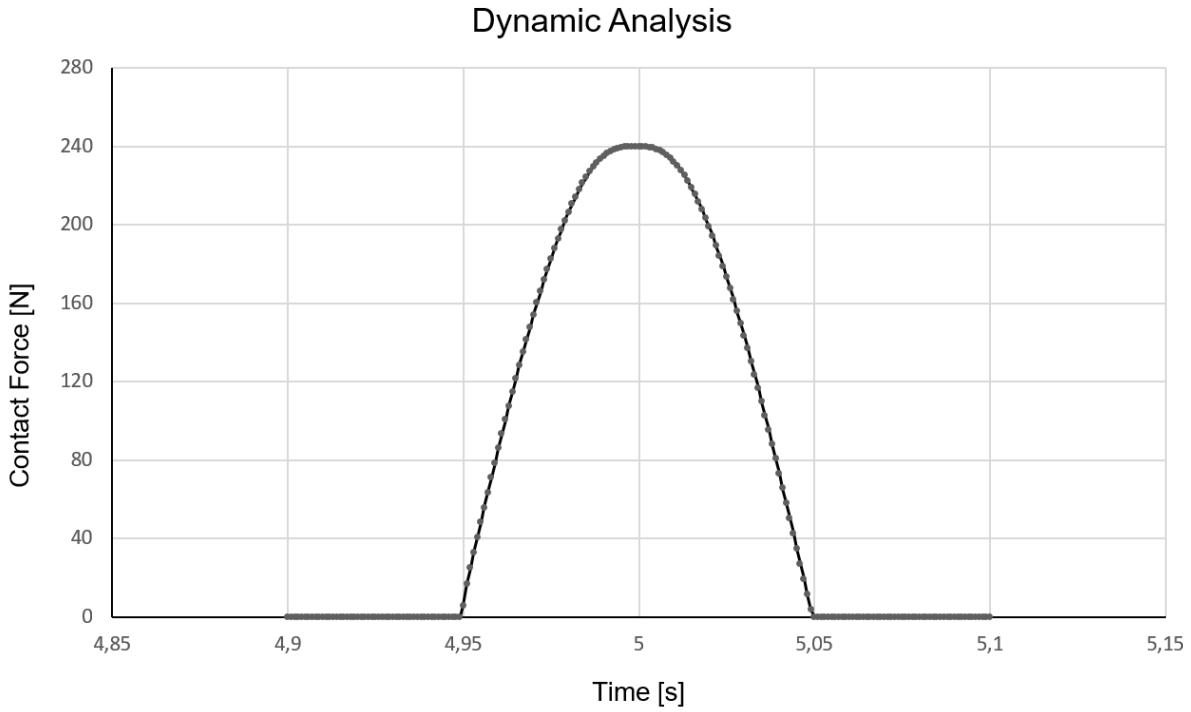

Figure 6.2: Contact Force zoomed on the contact window

6.3 Motor Torque

The torque analysis follows the same two–step strategy adopted for the contact force:

- a baseline run with gravity and inertia only, yielding the actuator torque required for raising and lowering;

- a contact evaluation in which the effect of the normal force is superposed on the baseline.

To account for the mechanism geometry, the effective lever arm between the actuator axis and the centroid of the contact patch on the head, $r_{eff}(t)$, was extracted from the CAD model. The distance was measured at the start of the contact window and at its center (e.g., t=4.95 s and t=5.00 s); the resulting variation across the 0.10 s window is small.

Accordingly, $r_{eff}(t)$ was represented by a linear interpolation sampled at $\Delta t = 1ms$, as the small variation justifies this assumption.

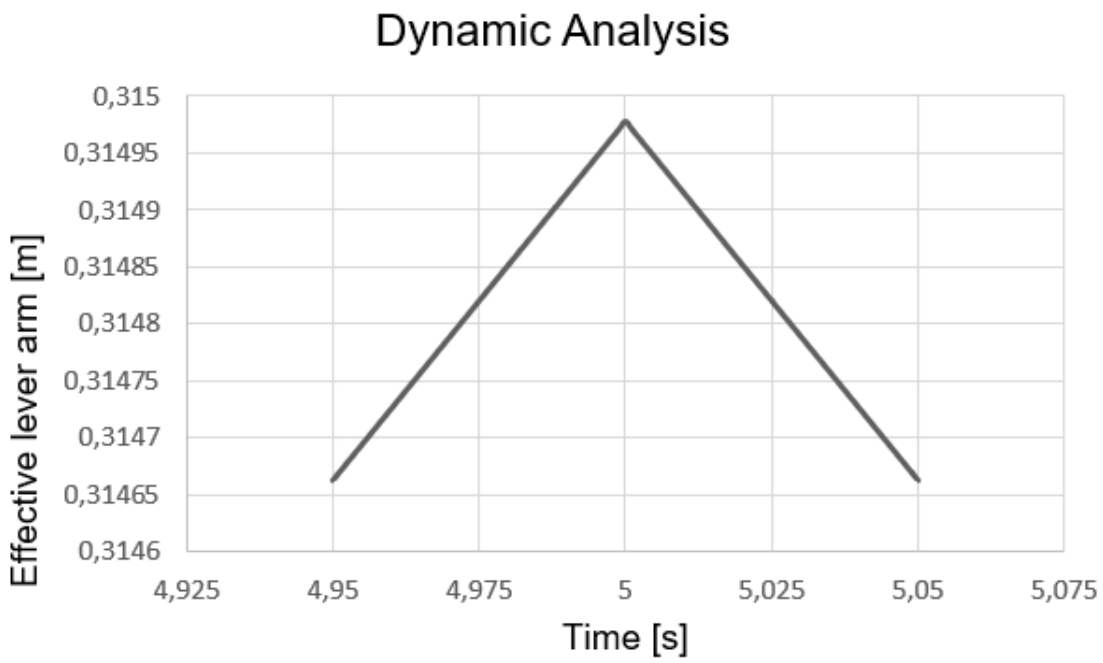

Figure 6.3: Effective lever arm due to contact

Given the contact force time history $F_n(t)$, the torque increment due to contact is computed as

$$T_{contact} = F_n(t) \cdot r_{eff}(t)$$

Its behavior is shown in the following Figure:

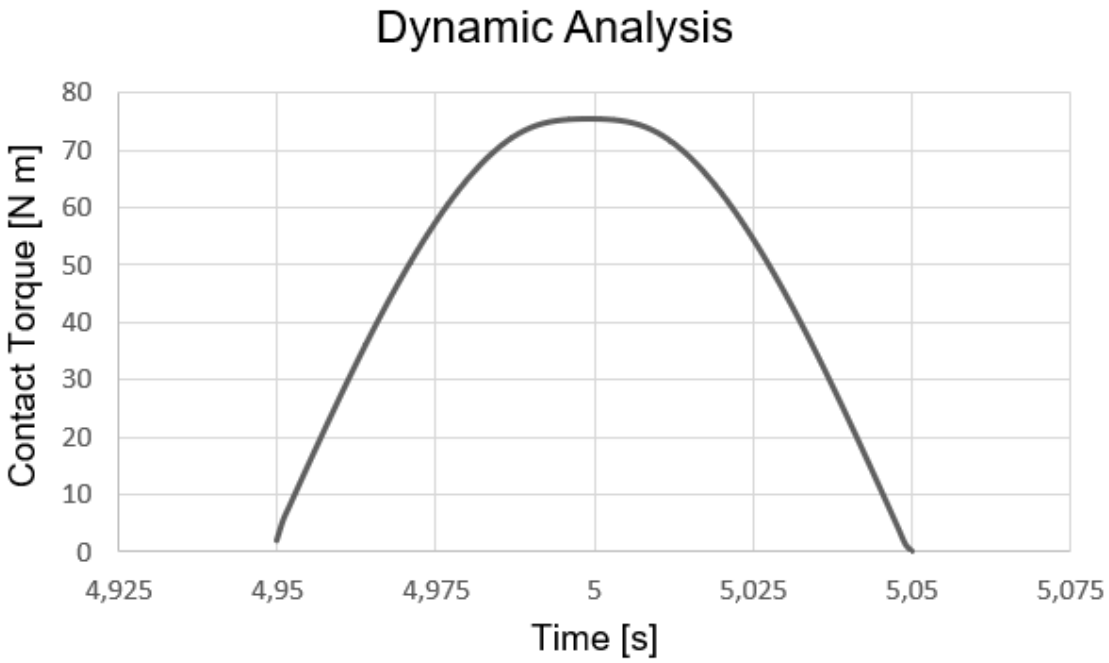

Figure 6.4: Torque increment due to contact

From the graph we can observe that the measured peak is at t=5s, equal to

$$T_{contact,max} = 75Nm$$

6.3.1 Total torque

The total actuator torque is obtained by superposition:

$$T(t) = T_{base}(t) + T_{contact}(t)$$

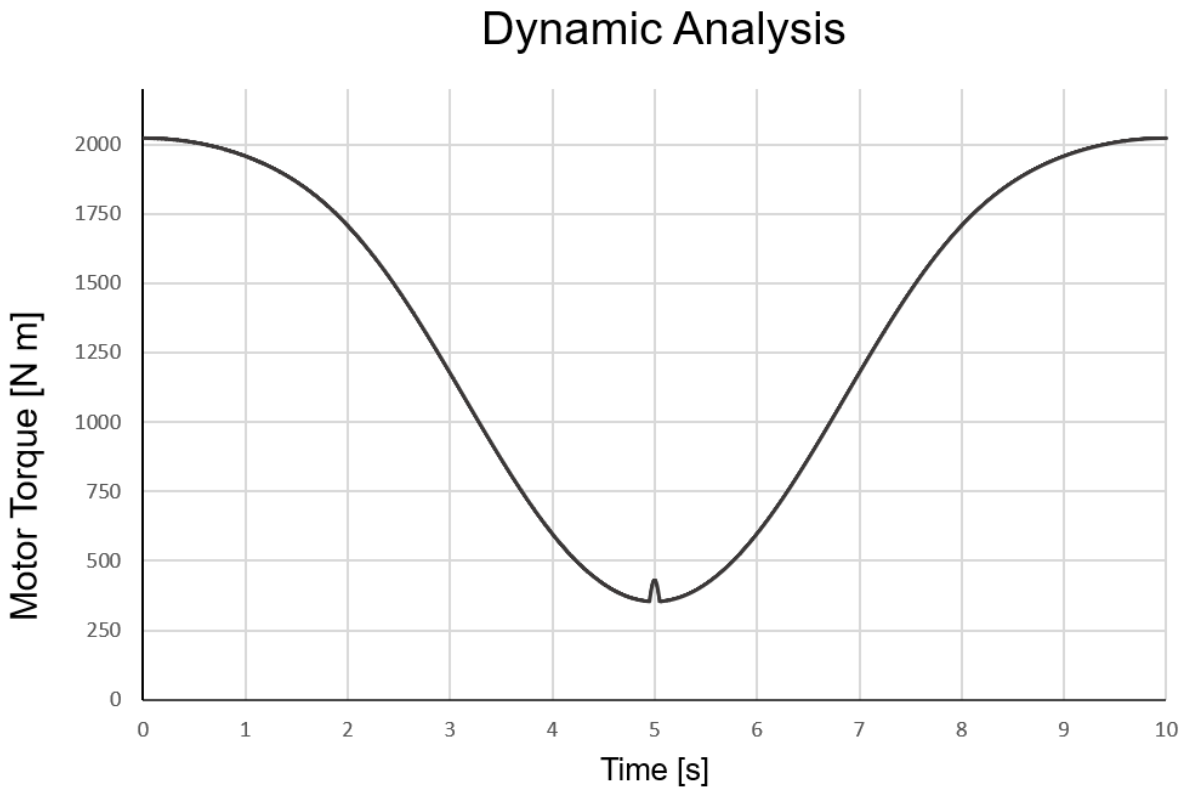

Figure 6.5: Total Actuator Torque

Over the full 10 s cycle, the curve is dominated by the gravitational component, with a smooth, localized bump in correspondence of the contact window. The contact adds only a modest, short-duration increment (about 75 $N \cdot m$), whereas the peak torque required by the mechanism is approximately 2.02 x 10^3 $N \cdot m$, confirming that gravity governs actuator sizing.

Power demand :

Using the angular velocity from the kinematic chapter, the instantaneous power is

$$P(t) = T(t) \cdot \dot{\theta}(t)$$

As expected for the imposed cosine law, $|\dot{\theta}|$ is maximum in t=2.5 s and in t=7.5 s, and near zero at t=5 s. Although it has been already presented in the previous chapter, the angular velocity graph is shown again below.

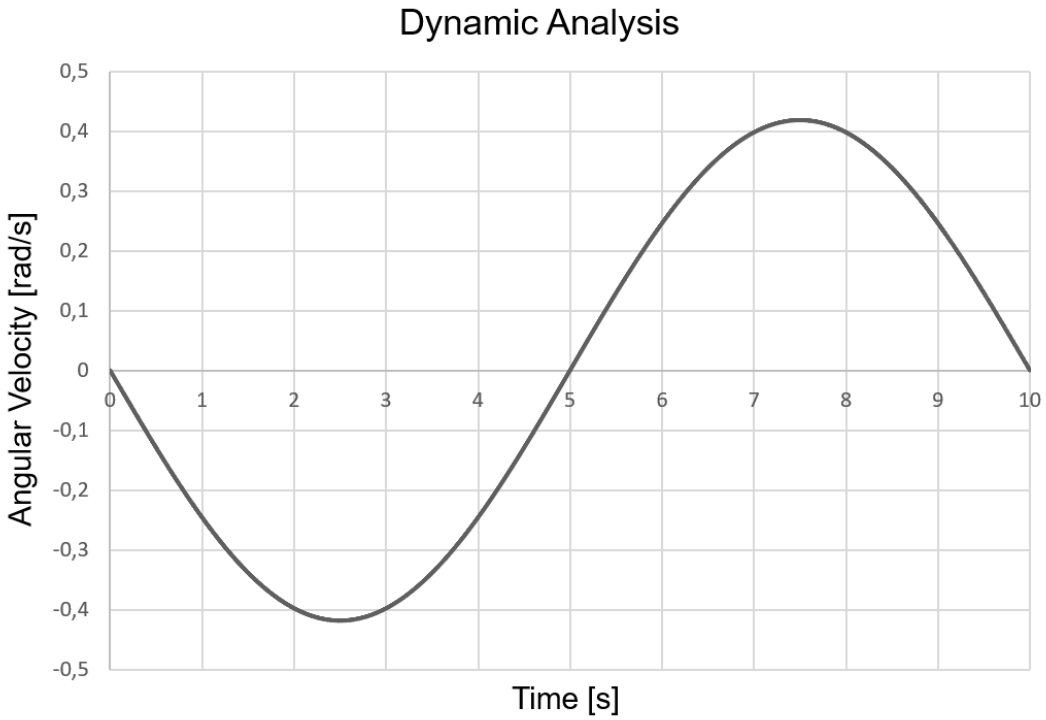

Figure 6.6: Motor Angular Velocity

Consequently, the power peak occurs away from contact and is about 0.7 kW. At the contact instant the power remains low despite the torque bump, because the angular speed is nearly zero.

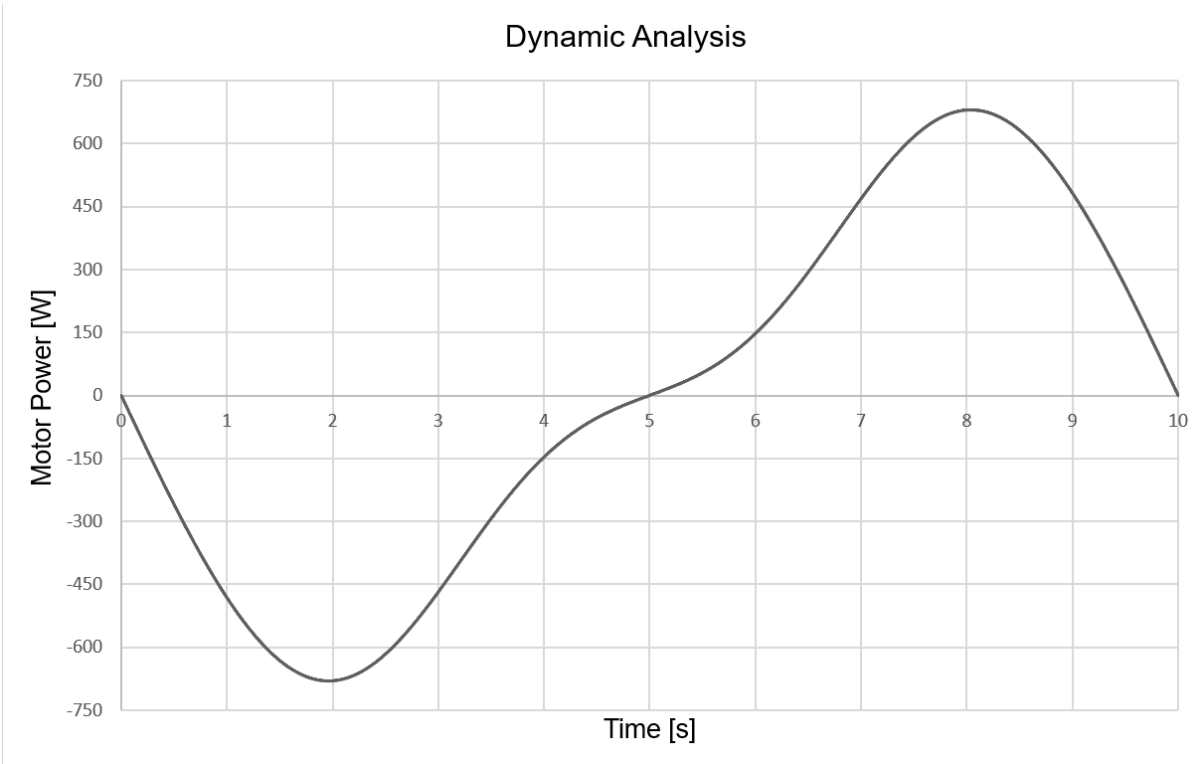

Figure 6.7: Actuator Power demand

6.4 Constraint reactions

Before presenting the reaction plots, we briefly define the four joints analyzed (see figure for reference and labels):

1. J1 – Roof - Main (reticular) link. It is the actuated revolute joint that drives the mechanism.
2. J2 – Roof - Support link. Together with J1 it anchors the mechanism to the bus roof (ground).
3. J3 – Contact head - Main link. Allows relative rotation to maintain proper alignment between the head and the charging column during contact.
4. J4 – Contact head - Support link. Same function as J3 on the support side.

Only one side of the mechanism is reported: the opposite side is geometrically symmetric and, where not exactly coincident, differs by only a few percent.

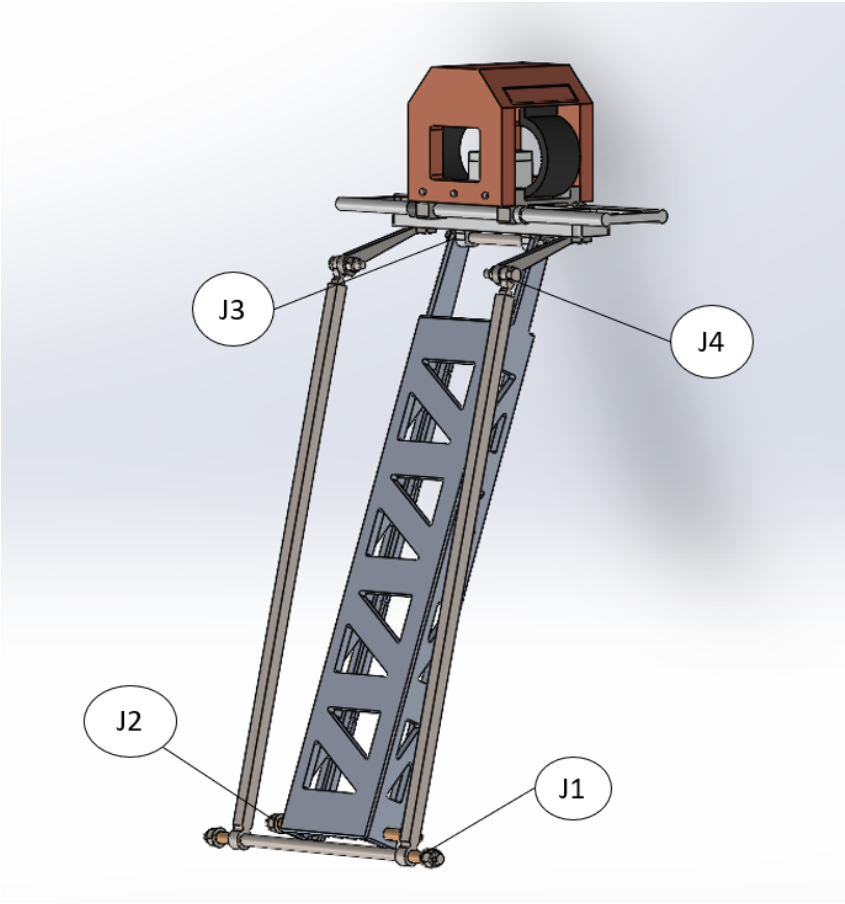

Figure 6.8: Analyzed Joints

For each joint we evaluate the principal reactions in the local joint reference system:

- Radial components: in-plane force $F_r(t) = \sqrt{F_x^2 + F_y^2}$ and in-plane bending moment $M_r(t) = \sqrt{M_x^2 + M_y^2}$;

- Axial components:$F_a(t)$ and $M_a(t)$ along the pin axis, expected to be negligible for a planar mechanism.

In this case too two simulations were performed:

A. Baseline run, considering just gravity and inertia, no contact, yielding

$$\mathbf{R}_A(t) = [F_x, F_y, F_z, M_x, M_y, M_z]$$

B. Contact window run over [4.95, 5.05] s with the equivalent normal force $F_n(t)$ applied along the local column normal, yielding $\mathbf{R}_B(t)$.

To avoid artificial discontinuities between runs, results were not stitched by direct replacement. Instead, the final reactions were obtained by per-component blending in the joint frames:

$$\mathbf{R}_{\text{final}}(t) = \mathbf{R}_A(t) \; + \; w(t)\,\big[\mathbf{R}_B(t) - \mathbf{R}_A(t)\big], \qquad w(t) = \frac{F_n(t)}{F_{n,\max}}.$$

This weighting (with $w = 0$ at the window edges and $w = 1$ at the peak) produces smooth, physically consistent curves. Only after the blending are the radial magnitudes F_r and M_r formed from the components. Axial components are reported for completeness and discussed as they are expected to be negligible.

6.4.1 Axial components

In this section will be shown the axial components F_a and M_a. As previously explained the mechanism moves along a plane of motion, expecting a negligible contribute of axial components compared to the in-plane (radial) ones.

Over the full cycle, PTC Creo was used to evaluate $F_a(t)$ and $M_a(t)$ for all joints. The results confirm the expectation: the measured peaks are on the order of

$$|F_{a,max}| < 1 \cdot 10^{-10} N$$

$$|M_{a,max}| < 1 \cdot 10^{-3} N \cdot m$$

several orders of magnitude below the corresponding in-plane reactions. These components are therefore non-dimensioning and will not be considered further.

For completeness, Figure 6.9 and Figure 6.10 reports representative time histories of $F_a(t)$ and $M_a(t)$; the traces remain effectively at zero across the entire cycle. As the same conclusion holds for all joints (J1–J4), axial plots are not repeated in the per-joint sections.

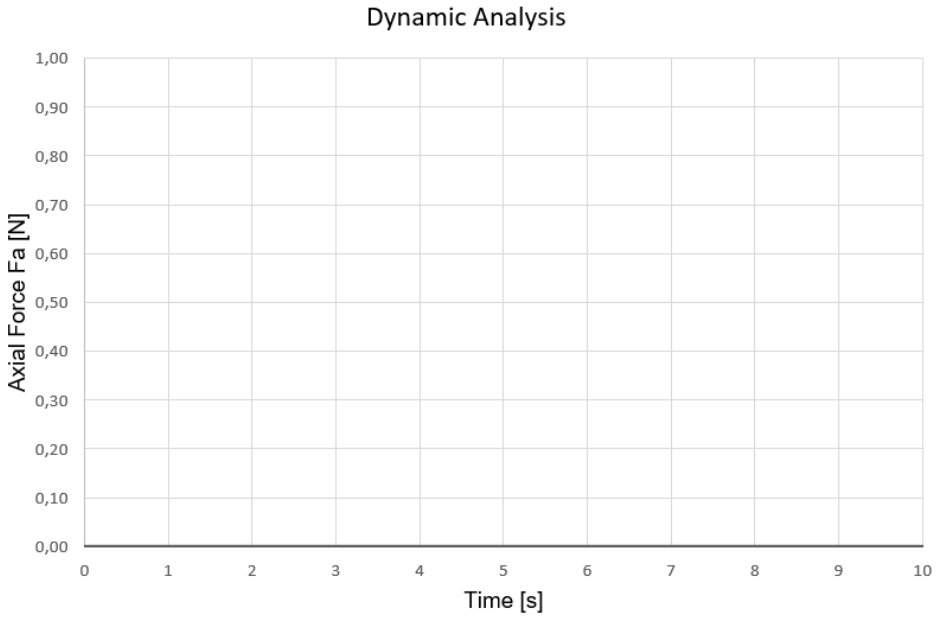

Figure 6.9: Joints' axial force

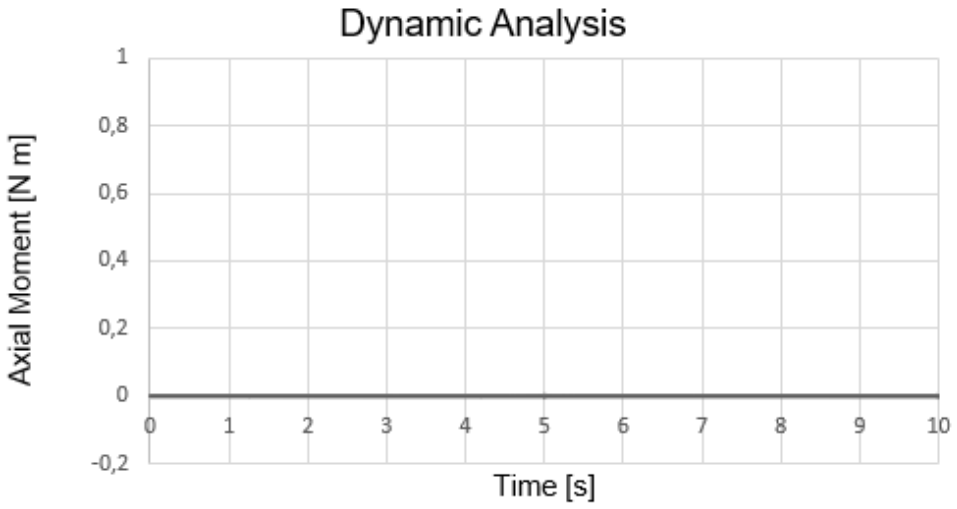

Figure 6.10: Joints' axial moment

6.4.2 J1 - Roof-Main (reticular) link

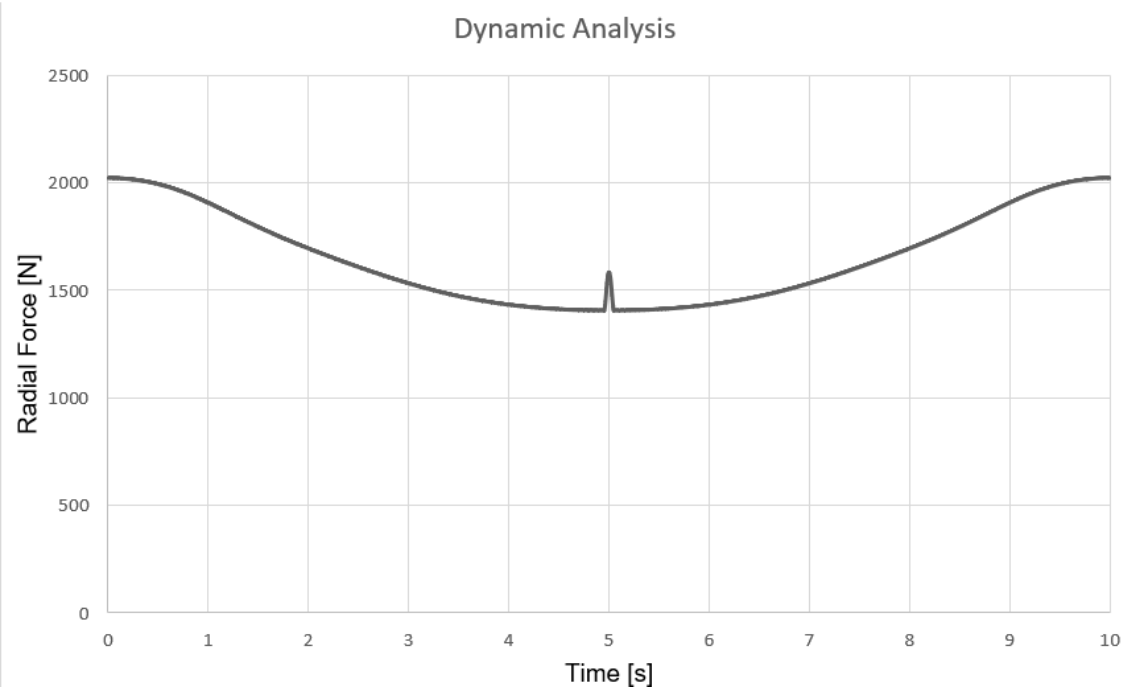

Figure 6.11: J1 Radial force

Figure 6.11 shows the radial force at joint J1 over one cycle. A localized increase associated with the contact event is visible; the Figure 6.12 zooms the [4.95–5.05] s window of contact (grey band). Outside this window the trend is governed by gravity, with a small inertial contribution, hence the overall "U-shaped" profile.

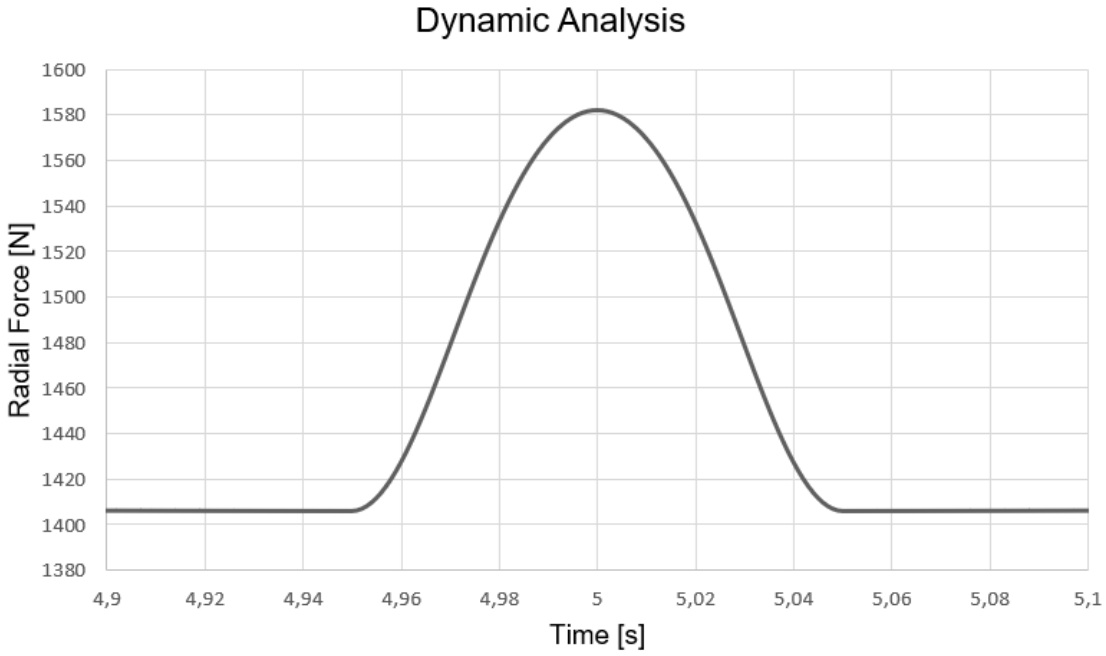

Figure 6.12: J1 Radial force zoom on the contact window

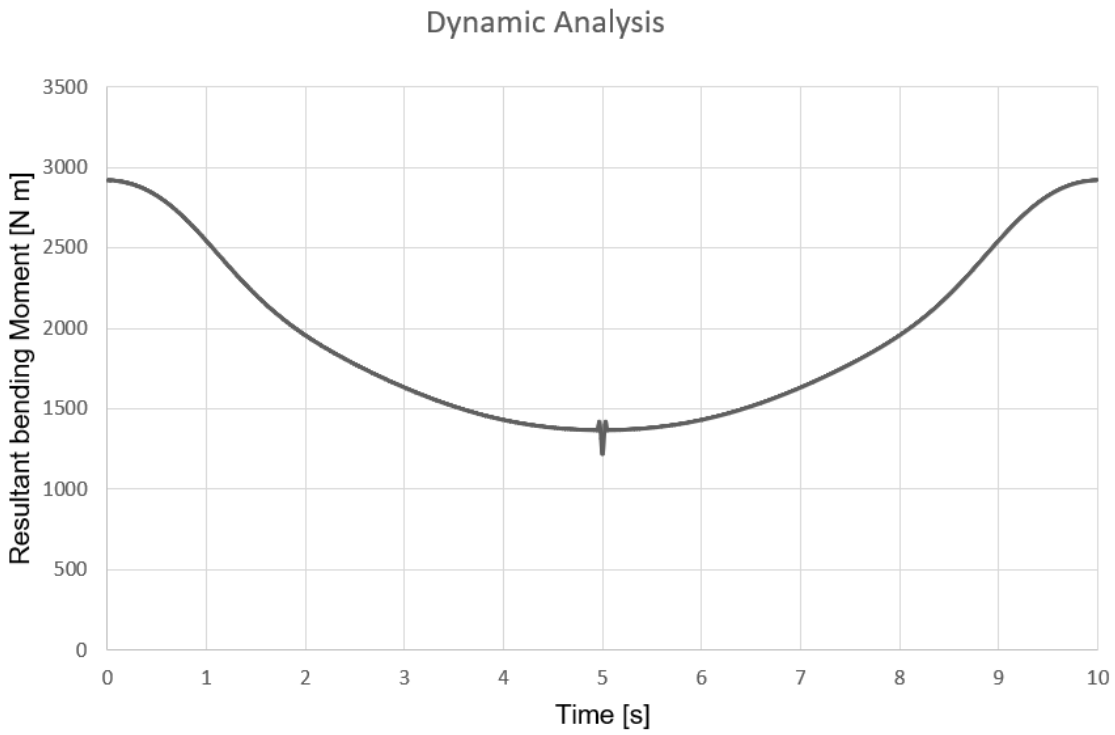

Figure 6.13: J1 Resultant bending moment

The resultant bending moment at joint J1 follows the same qualitative behaviour as $F_r(t)$. A small, localized perturbation appears within the contact window, while the global response over the 0–10 s cycle is dominated by gravity and inertia. The amplitude is consistent with the local lever arm at J1.

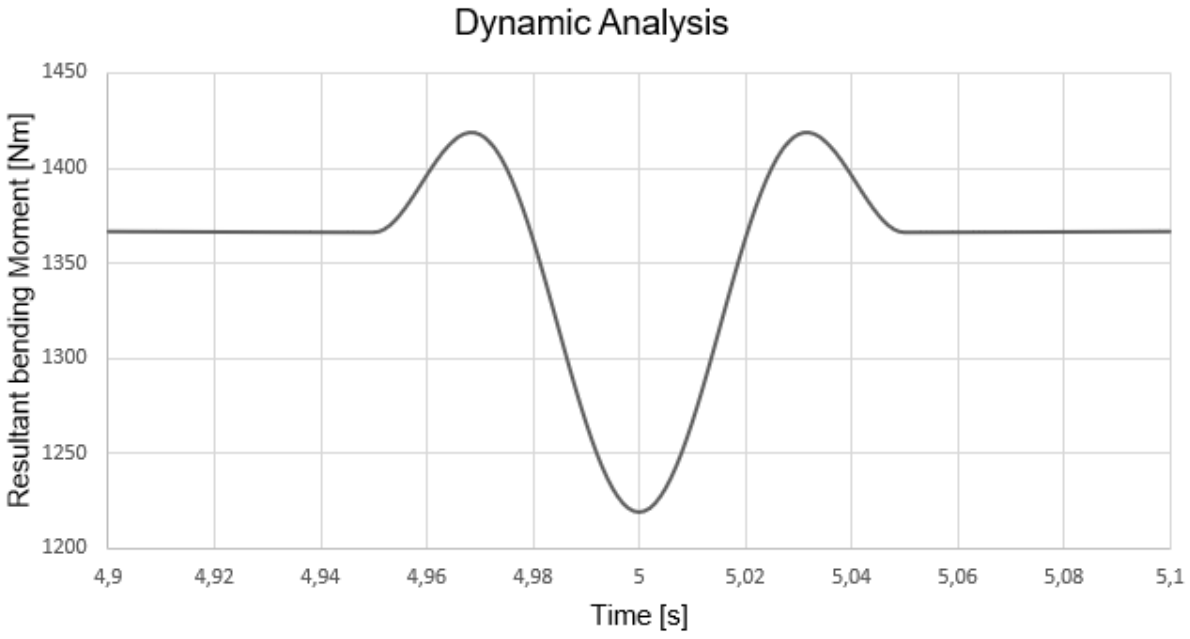

Figure 6.14: J1 Resultant bending moment zoom on the contact window

6.4.3 J2 - Roof-Support link

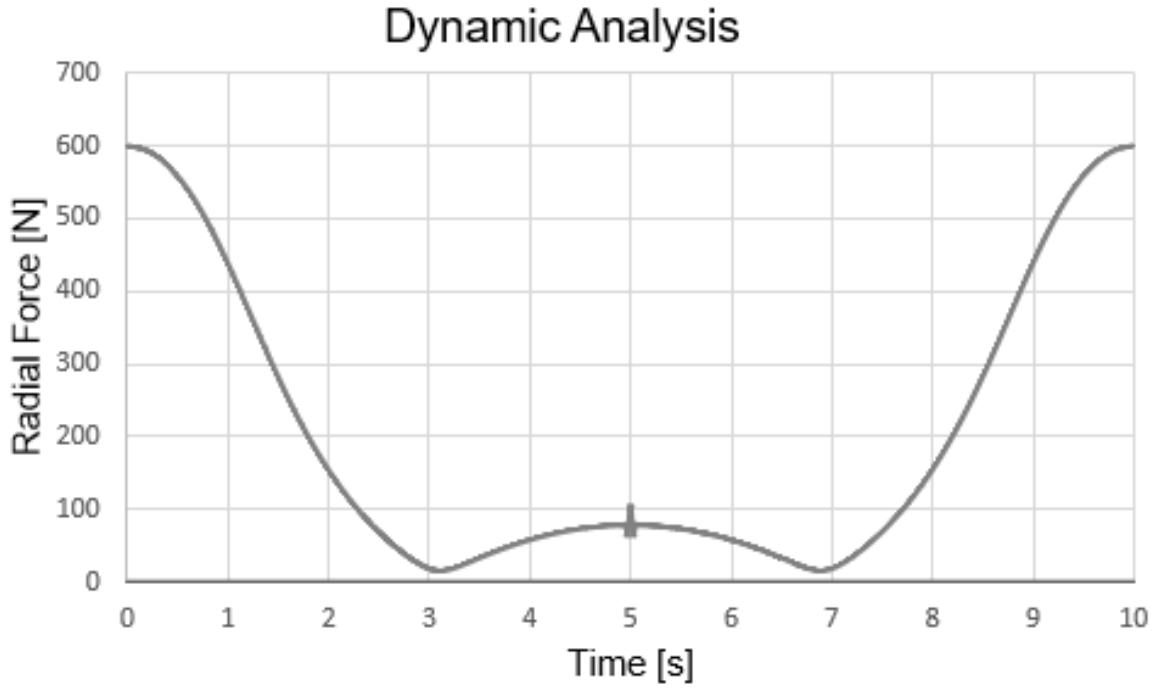

Figure 6.15: J2 Radial force

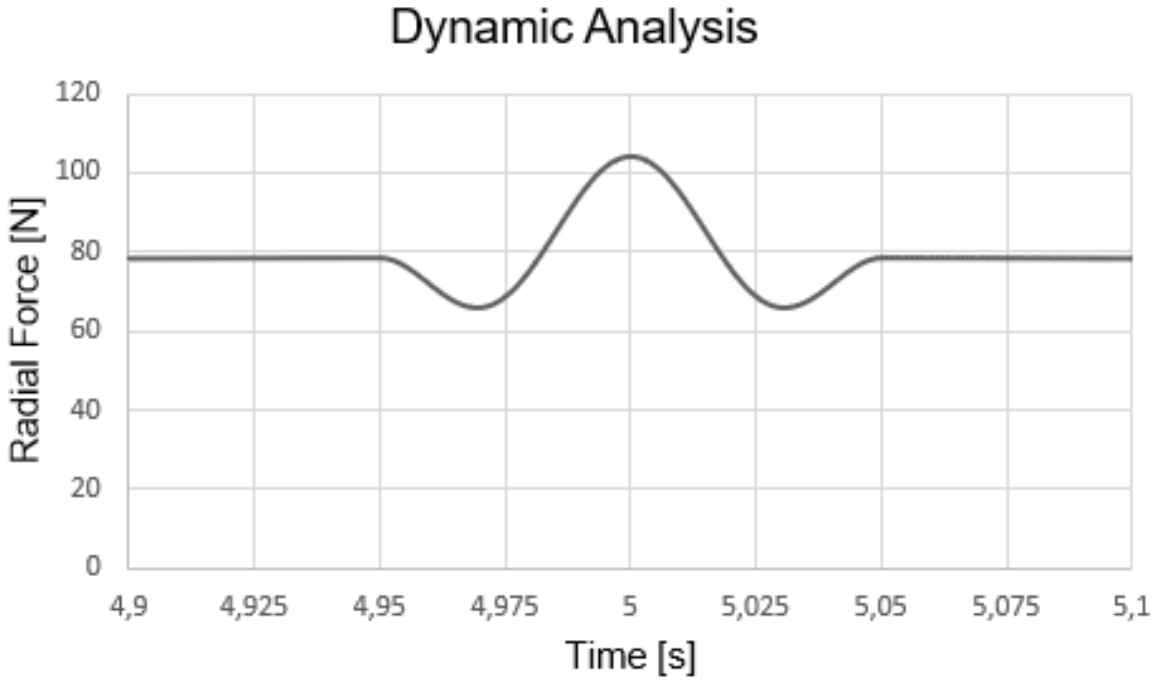

Figure 6.16: J2 Radial force zoom on the contact window

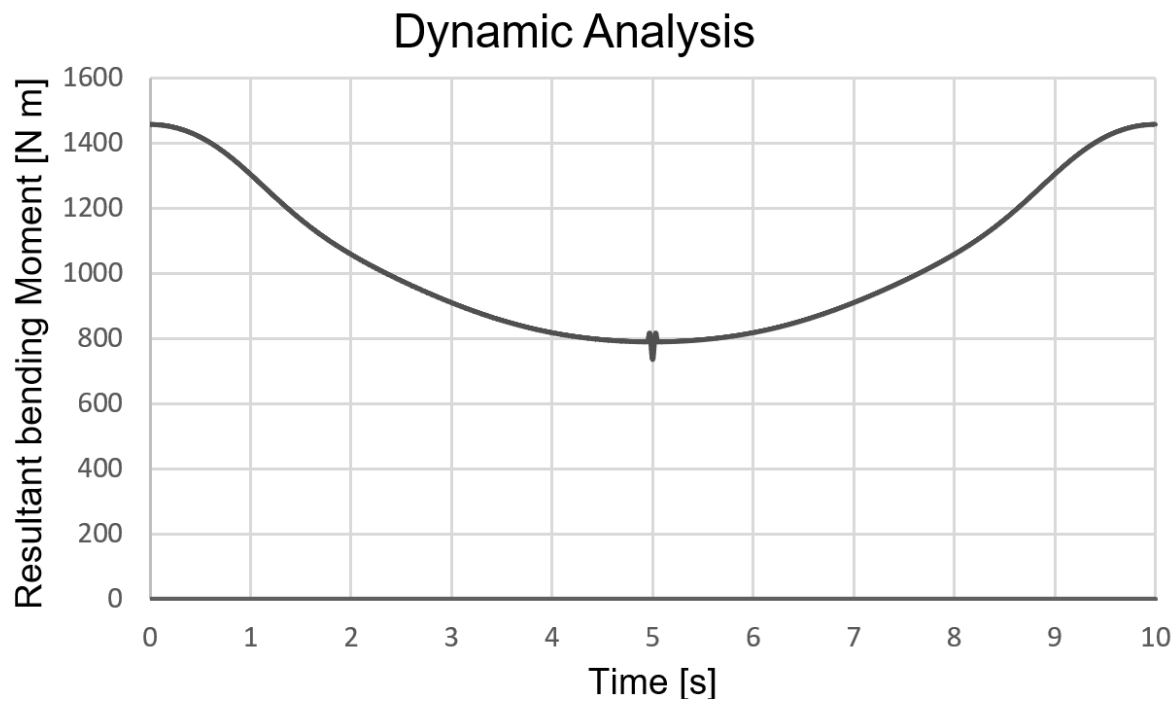

Figure 6.17: J2 Resultant bending moment

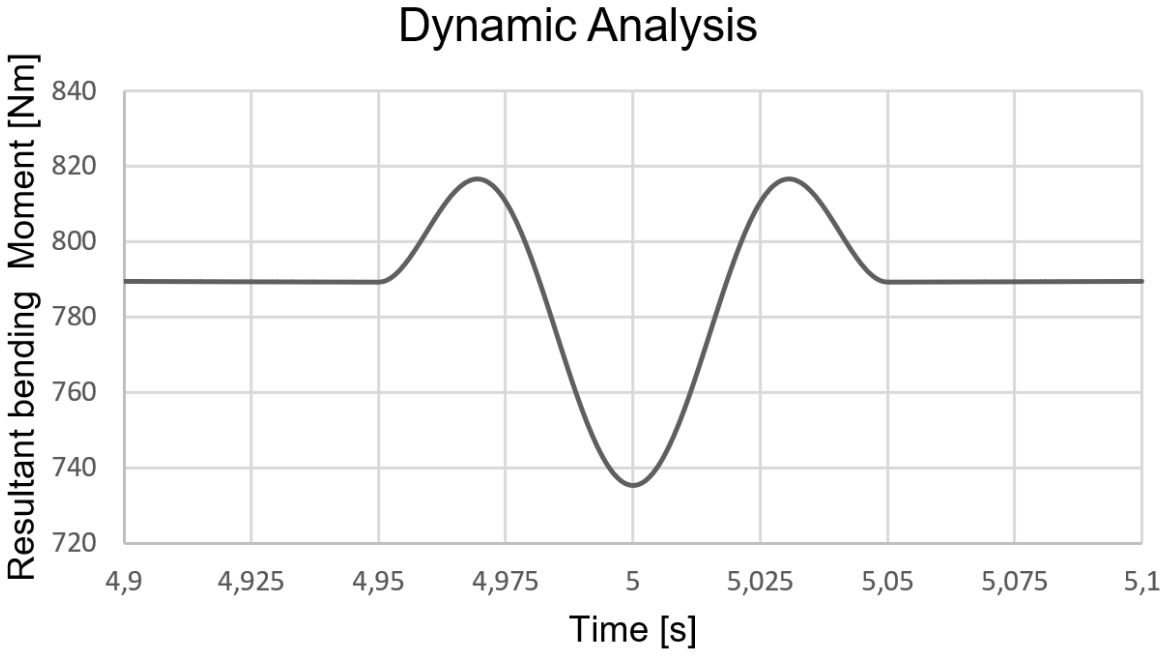

Figure 6.18: J2 Resultant bending moment zoom on the contact window

Same qualitative behaviour as J1: gravity and inertia govern the cycle, and the contact produces a small, localized perturbation within the [4.95–5.05] s window. Differences in amplitude reflect the load path and local geometry of the joint.

6.4.4 J3 - Contact head-Main link

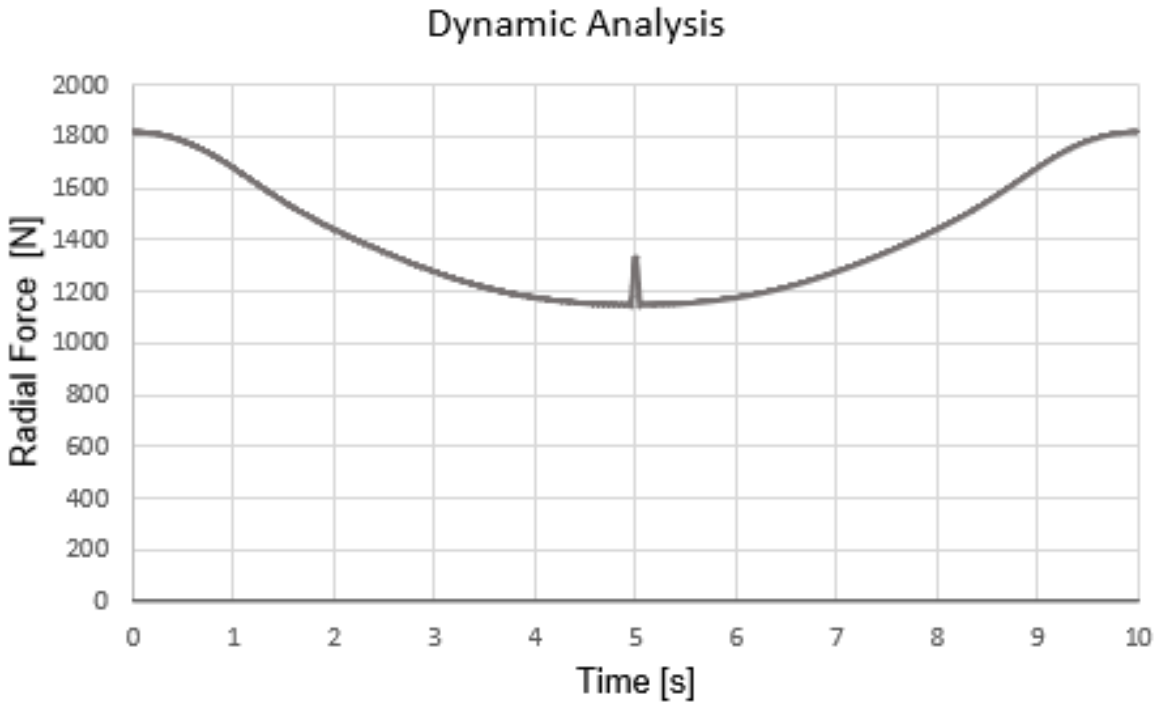

Figure 6.19: J3 Radial force

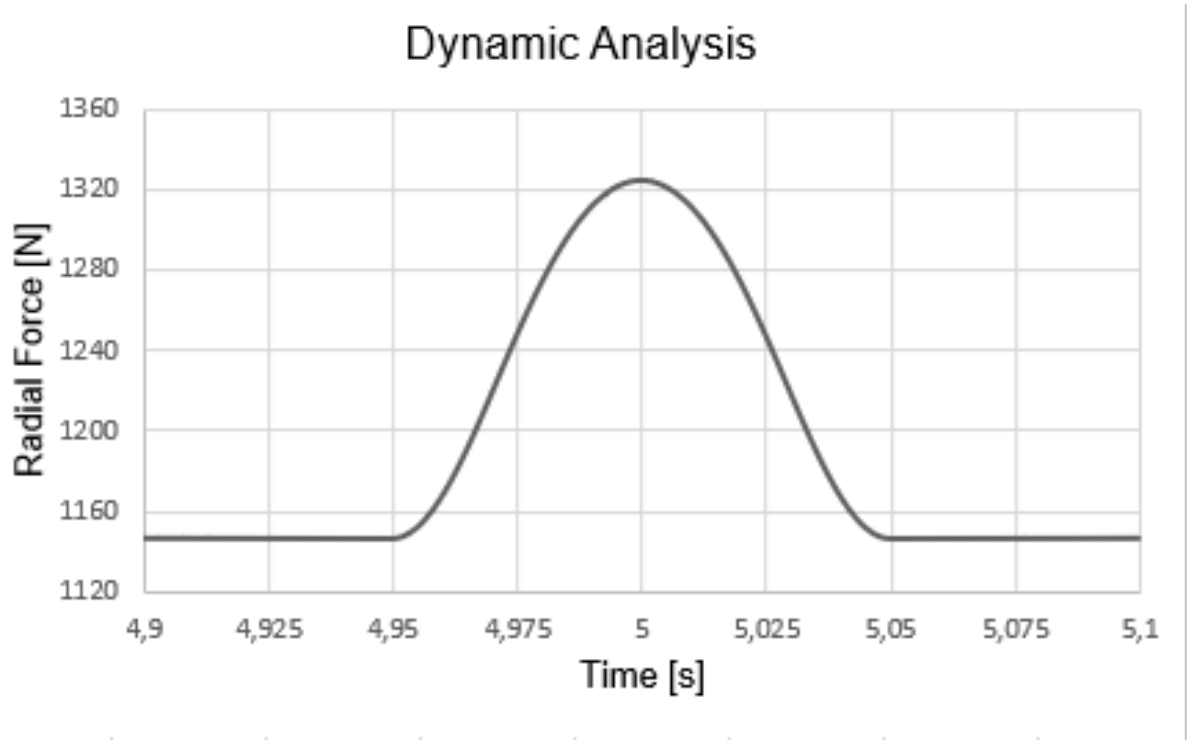

Figure 6.20: J3 Radial force zoom on the contact window

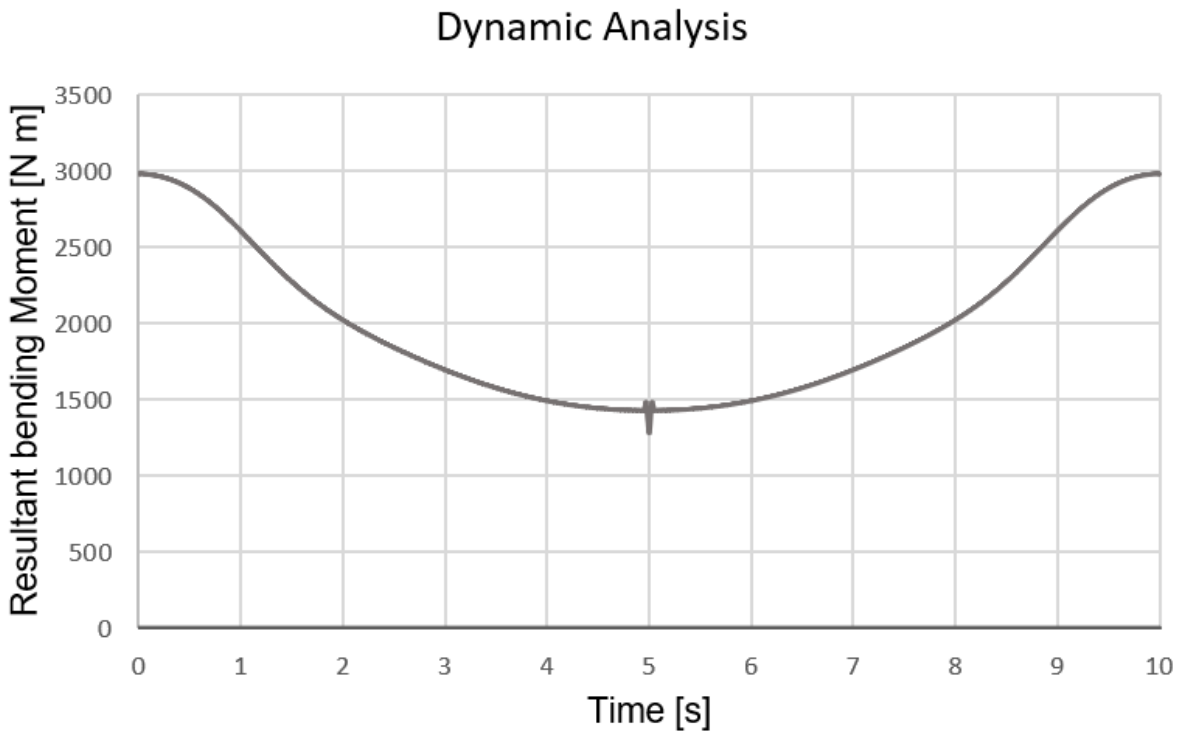

Figure 6.21: J3 Resultant bending moment

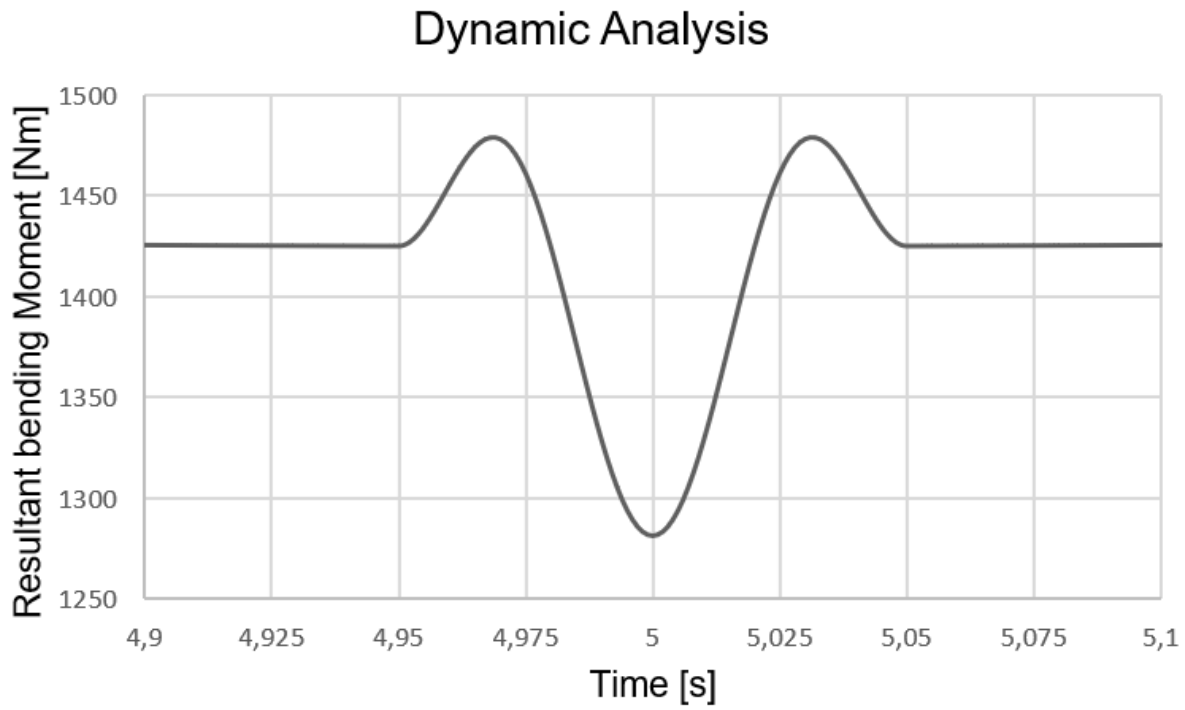

Figure 6.22: J3 Resultant bending moment zoom on the contact window

It exhibits the same qualitative behavior as J1 and J2: gravity and inertia dominate the cycle, while contact induces a minor, localized disturbance confined to the [4.95–5.05] s interval. Amplitude variations stem from the load path and the joint's local geometry.

6.4.5 J4 - Contact head-Support link

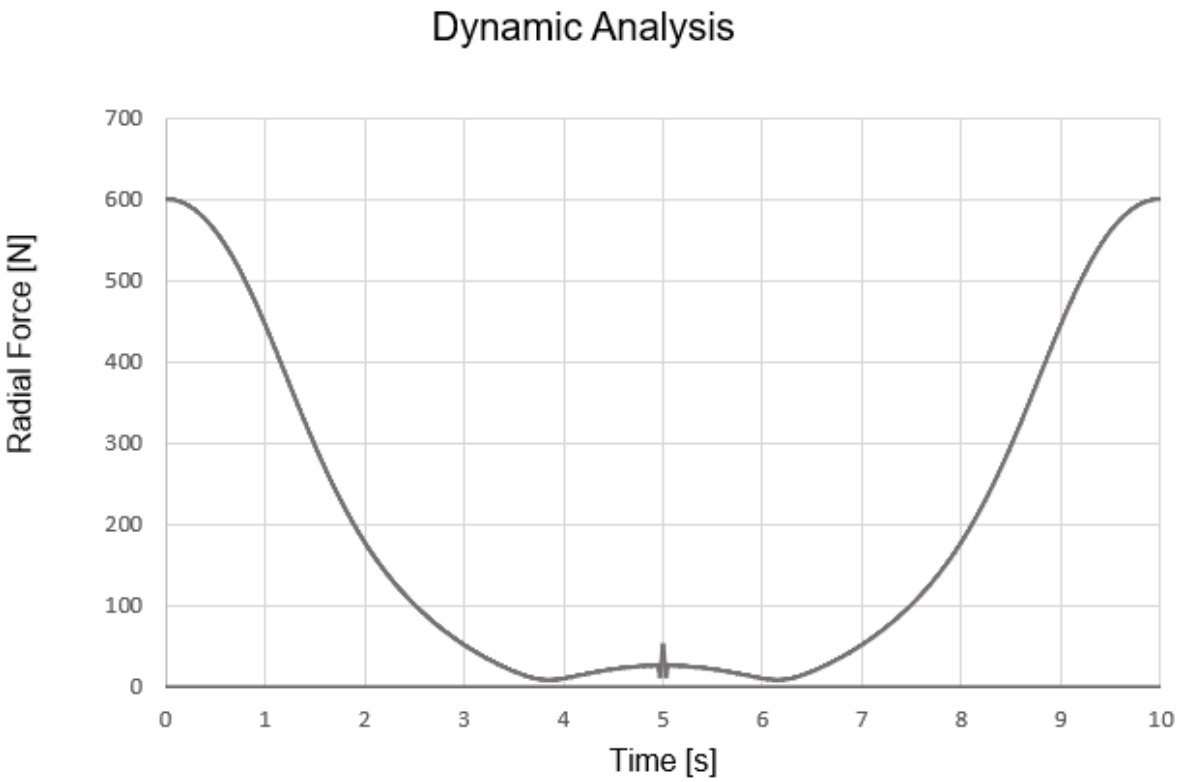

Figure 6.23: J4 Radial force

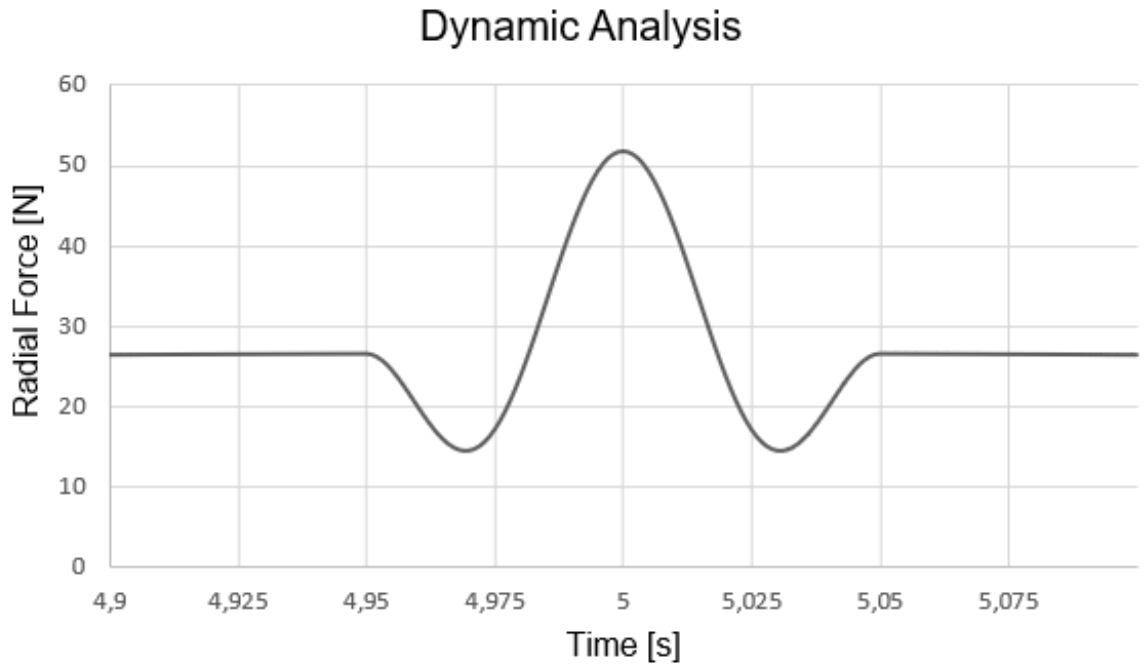

Figure 6.24: J4 Radial force zoom on the contact window

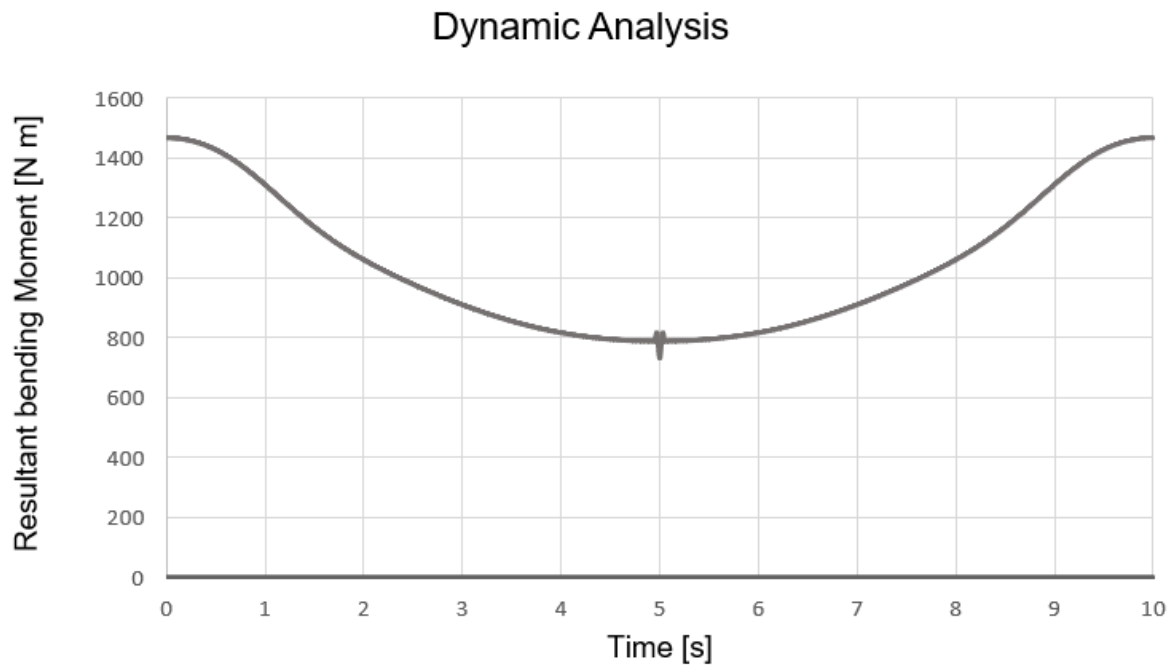

Figure 6.25: J4 Resultant bending moment

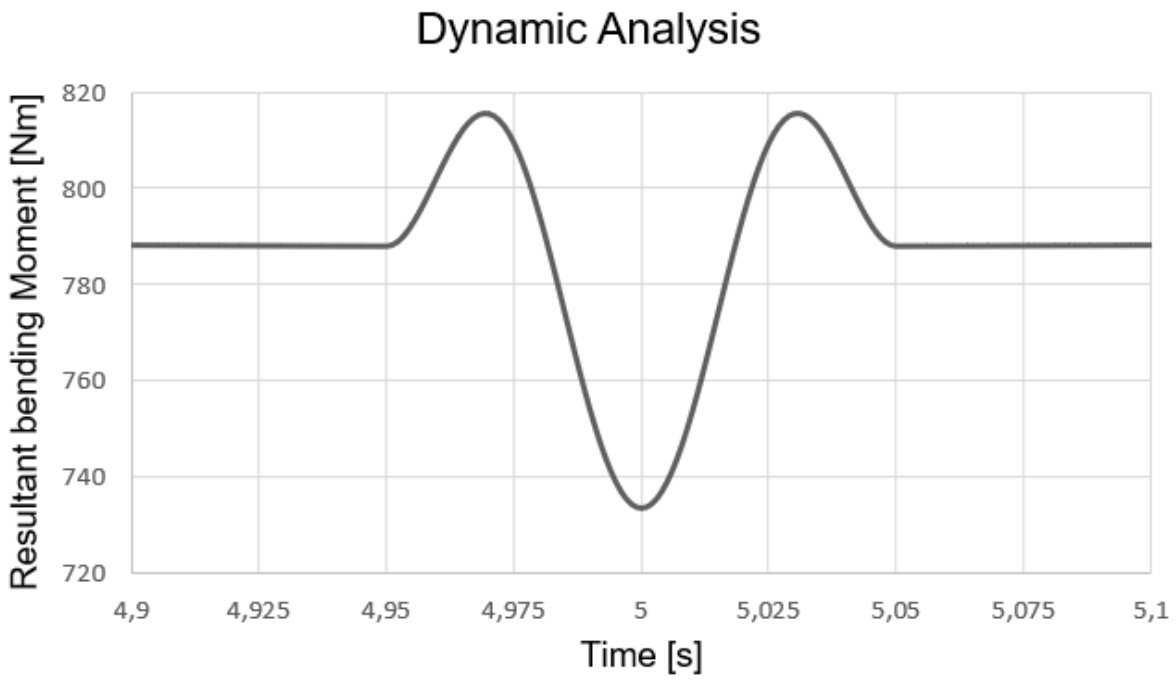

Figure 6.26: J4 Resultant bending moment zoom on the contact window

The qualitative response mirrors that of the previous joints: the cycle is governed by gravity/inertia, with a small, localized perturbation due to contact within [4.95–5.05] s.

Chapter 7

Economic analysis

This section provides an order-of-magnitude economic assessment for installing an on-route pantograph-up charger.
The analysis distinguishes Capital Expenditures (CAPEX) - equipment, civil works, grid connection - and Operational Expenditures (OPEX) - maintenance and electricity (energy and demand charges).

7.0.1 CAPEX

CAPEX is divided into four items:

- Charging equipment (pantograph head + power cabinet). Values vary by power rating, vendor, location and options. As indicative market ranges for a 300–600 kW pantograph system, we assume US$ 120k–180k (hardware only), about €100k–150k at current exchange rates [26–28].

- Civil works and installation: foundations or plinths, trenching and cabling, switchgear, permitting. On-route sites tend to be more expensive than depots due to higher power and urban works. We assume US$ 60k–120k (about €50k–100k), depending on the site [29].

- Grid connection: primary utility engineering and upgrades are typically budgeted per *kW·distance*. Using planning envelopes, US$ 150–2,450 per kW·mile (which corresponds to US$ 93.2–1,522 per kW·km), which is about €79–1,296 per kW·km. Higher charging power generally drives higher upstream costs [30].

- Engineering and permitting: design, permits, commissioning. We assume €17,000–50,000.

Combining the items above we obtain the summary in Table 7.1. For the grid connection line, costs must be multiplied by the site-specific route length (in km) and by the charger power (in kW).

Type of cost	Unit	Cost	Notes and reference
Charging equipment	1 set	€100k – 150k	Hardware only [26–28]
Civil works and installation	lump	€50k – 100k	Foundations, cabling, switchgear [29]
Grid connection	per kW·km	€79 – 1,296	Primary utility engineering [30]
Engineering and permitting	lump	€17,000 – 50,000	Design, permits, commissioning

Table 7.1: CAPEX summary (order of magnitude).

Illustrative total CAPEX example. Assuming a 300 kW charger and 0.5 km of upstream works, the grid connection term is:

$$\text{Grid} = (79\text{–}1{,}296)\ \frac{€}{\text{kW·km}}\ \times 300\ \text{kW}\ \times 0.5\ \text{km} = €11{,}850 - 194{,}400$$

Hence, total CAPEX would be:

Type of cost	Cost
Equipment	€100k – 150k
Civils	€50k – 100k
Grid	€11.9k – 194.4k
Engineering	€17k – 50k
Total	**€180k - 495k**

Table 7.2: CAPEX Total Cost

Actual costs depend on feeder capacity, distance, ground conditions and permitting.

7.0.2 OPEX

OPEX is the recurring cost of operating the site:

- Maintenance: routine inspections, filters, firmware, excluding failures. Planning values: €850–2,500/year [30].
- Electricity (energy and demand charges): the delivered €/kWh is highly sensitive to utilization and demand charges [31, 32].

Type of cost	Unit	Cost	Notes and reference
Annual maintenance	per year	€850 – 2,500	Routine service [30]
Electricity (energy and demand)	kWh	site-specific	Strongly dependent on utilization and tariffs [31, 32]

Table 7.3: OPEX summary.

Illustrative demand-charge example.
If the monthly demand charge is €10/kW·month and the site peaks at 300 kW, the monthly demand fee is €3,000. If the charger delivers 30,000 kWh/month, this adds €0.10/kWh. Higher utilization (more kWh/month) reduces the €/kWh impact; low utilization increases it.

7.0.3 Budget estimate (1-year OPEX added to CAPEX)

To provide a single budget figure, we combine the CAPEX estimation of Table 7.2 with one year of OPEX under the following assumptions:

- Charger rating: 300 kW;
  Upstream works: 0.5 km (grid term per Table 7.2).
- Energy delivered: 30,000 kWh/month ⇒ 360,000 kWh/year.
- Energy price: € 0.15/kWh (base energy tariff).
- Demand charge: € 10/kW·month at 300 kW peak ⇒ € 3,000/month ⇒ € 36,000/year
- Annual maintenance: € 850 – 2,500/year.

Annual electricity cost

With 360,000 kWh/year:

Type of cost	**Operation**	**Annual Cost**
Energy component	360,000 × 0.15	€54,000
Demand charges	12 × 3,000	€36,000
Annual maintenance		€850 - 2,500
Total cost		**€90,850 - 92,500**

Table 7.4: Annual OPEX

Total budget (CAPEX + 1 year OPEX)
Using the CAPEX range from Table 7.2:

CAPEX	€180,000 - 495,000
1 year OPEX	€90,850 - 92,500
Total cost	**€270,850 - 587,500**

Table 7.5: Total budget

The €/kWh impact of demand charges scales inversely with utilization. For example, if monthly energy doubles to 60,000 kWh (same 300 kW peak), demand adds ∼ €0.05/kWh instead of €0.10/kWh; the absolute annual electricity cost rises, but the delivered cost

per kWh falls (improved utilization).

Table 7.5 reports the budget for capital costs plus 1 year of operational costs of the pantograph-up system. Over the system lifetime, the total operating cost can be estimated by multiplying the number of years by the annual OPEX and adding the initial CAPEX.

In this study the bus cost is not considered, as the same charging column may be used by several buses, allowing significant amortization of bus investment costs; the work focuses just on the charging site.

7.0.4 General remarks and conclusions

Economic performance hinges on the bus-to-charger ratio and the quality of the site. Sharing an on-route charger among more buses mitigates demand-charge exposure. Proper location and coordination with the utility are crucial to minimize the Total Cost of Ownership (TCO) [31].

On-route infrastructure has higher upfront costs (power level, utility upgrades) than typical depot charging, but can reduce required battery size and improve service availability thanks to frequent charges [29]. Operational constraints (dwell-time, driver workload) often favour pantograph-up on high-frequency routes.

Overall, public studies and vendor information consistently indicate that grid connection and demand charges are the decisive cost drivers; charger hardware is a smaller share of total site cost. Utilization is the key lever to reduce levelized charging cost.

Assumptions: prices are indicative and based on public sources, such as vendor-listed prices used for order-of-magnitude only; the US$-€ conversion uses a representative rate ($1=€0.85). Site-specific design, feeder capacity and permitting can deeply affect totals.

Chapter 8

Conclusions

This thesis presented the modelling and dynamic assessment of a Pantograph-Up charging system for battery-electric buses, inspired by the real deployment on Barcelona's H16 line. The workflow combined on-site observation, theoretical framing, CAD modelling and multibody simulation to deliver a complete kinematic and dynamic analysis.

Modelling and kinematics .
A planar, single-DOF rigid-body model of the mechanism was derived from the SolidWorks geometry and simulated in PTC Creo under a cosinusoidal motion law over a 10 s cycle (5 s raising and 5 s lowering). The contact was idealised as an instantaneous event at the half of the cycle, which is consistent with a real charging dwell that lasts several minutes under essentially constant contact force. The kinematic analysis produced the expected pose, velocity and acceleration histories; the angular velocity is near zero at the contact instant, which mitigates impulsive effects during electrical engagement.

Dynamic analysis and contact force .
The dynamic study followed a two-step baseline + contact window strategy that isolates the physical effect of contact without relying on a full 3D contact solver. Because the available software version did not robustly handle surface-to-surface contact, the head–column interaction was represented by four compression-only spring–damper pairs located at corresponding points on the contact patch. The reconstructed resultant normal force exhibits a single, localised pulse within the [4.95–5.05] s window, with a peak $F_{n,max} = 240.1\ N$, consistent with typical application ranges reported in the literature and datasheets.

Actuator torque and power .
The contact contribution to actuator torque was computed analytically as

$$T_{contact} = F_n(t) \cdot r_{eff}(t)$$

using the CAD-measured lever arm between the actuator axis and the contact-patch centroid. The maximum increment is about 75 N·m at contact. Superposed on the gravity+inertia baseline torque, the total curve shows a smooth, localised bump at contact

and a peak torque of approximately 2.02 x 10^3 $N \cdot m$ over the cycle.

The instantaneous power

$$P(t) = T(t) \cdot \dot{\theta}(t)$$

reaches about 0.7 kW in magnitude away from contact and remains small at the contact instant because the angular speed is near zero. These results indicate that actuator sizing is dominated by gravity, not by the contact event.

Joint reactions .
Across the four representative joints, radial forces F_r and bending moments M_r govern the mechanical loading over the cycle, with a localised perturbation during contact.
Axial components F_a and M_a remain several orders of magnitude below the in-plane reactions and are non-dimensioning.

Methodological note .
The adopted two-step strategy with per-component blending in the local joint frames proved effective in avoiding spurious discontinuities between runs, while keeping the approach transparent and computationally light. The method yields design-relevant quantities (contact force, torque and power envelopes, joint reaction peaks) with clear traceability.

Economical analysis .
In addition, a first-order economic assessment of an on-route Pantograph-Up site (300 kW, 0.5 km make-ready) indicates a CAPEX value on the range €180k–€495k and an annual OPEX of about €91k (which considers energy delivered, demand charges and maintenance). The analysis confirms that grid connection and demand charges are the dominant cost drivers and that high utilization (buses per charger) is the key lever to reduce levelized €/kWh.

Limitations of the work .
Within the assumptions of planar rigid bodies, surrogate contact, no explicit modeling of joint backlash or dry friction, and no electro-drive co-simulation, the model still predicts contact forces and actuator efforts of the correct order of magnitude, providing a reliable basis for preliminary mechanical sizing and control design.

References

[1] ABB, "Charging infrastructure catalogue," 2022, product catalogue.

[2] "Autobus elettrici nel trasporto pubblico. un vademecum."

[3] E. Parliament, "Co2 emissions from cars: facts and figures (infographics)," *European Parliament*, 2019.

[4] C. Merico, "In città non si respira una bella aria e per il 60% è colpa delle auto," *la Repubblica*, 05/05/2022.

[5] European Environment Agency, "Veicoli elettrici: una scelta intelligente per l'ambiente," *European Environment Agency*, 2019.

[6] Heliox, "In che modo i paesi del mondo hanno elettrificato il trasporto pubblico?" *Heliox*, 2023.

[7] L'Indipendente, "La rivoluzione urbana di barcellona per una mobilità sostenibile," *L'Indipendente*, 2022.

[8] The Map Report, "Barcellona: l'80% dei viaggi effettuati in modo sostenibile lo scorso anno," *The Map Report*, 2024.

[9] Mobility City, "Endesa instala nuevas estaciones de recarga para autobuses eléctricos en barcelona," *Mobility City*, 2019.

[10] U.S. Department of Energy, "Emissions from electric vehicles," *U.S. Department of Energy.*

[11] European Environment Agency, "Electric vehicles and the energy sector - impacts on europe's future emissions," *European Environment Agency*, 2016.

[12] M. H. -I. e. J. P. T. . M. L. T. Peter Kasten, Joß Bracker, "Electric mobility in europe – future impact on the emissions and the energy systems," Öko-Institut e.V., Tech. Rep., 2016.

[13] C40 CITIES, "Cities100: Barcellona - le iniziative dei cittadini guidano l'azione per il clima," *C40 CITIES*, 2016.

[14] G. W. Dennis Wagner, "Techno-economic analysis of mixed battery and fuel cell electric bus fleets: A case study, applied energy," *Volume 376, Part A*, 2024.

[15] Admin AUTOBUSWeb, "Tmb, 210 autobus elettrici e ibridi per accelerare la decarbonizzazione a barcellona," *AUTOBUSWeb*, 2021.

[16] AGENZIA DI INFORMAZIONE FERROVIE, TRASPORTO LOCALE E LOGISTICA, "Barcellona: attivata la seconda linea di bus 100% elettrica ad alta capacità," *AGENZIA DI INFORMAZIONE FERROVIE, TRASPORTO LOCALE E LOGISTICA*, 2023.

[17] O. Elma and H. A. Gabber, "Flywheel-based ultra-fast on-route charging system for public e-buses," *2020 International Conference on Electrical, Communication, and Computer Engineering (ICECCE)*, Istanbul, Turkey, 2020, pp. 1-4.

[18] D. Guerrero, "Barcelona tendrá una línea con todos los buses eléctricos," *LA VANGUARDIA*, 2019.

[19] Enciclopedia Treccani, accessed: 20 March 2025.

[20] F. Policicchio, *Lineamenti di infrastrutture ferroviarie, pp. 147-148.* Firenze University Press, 2007.

[21] https://www.ansa.it/sito/notizie/cronaca/2025/01/11/che-cose-un-pantografo-e-perche-e-cruciale-nella-circolazione-ferroviaria.*html*, *accessed* : 20*March*2025.

[22] enel x: Uno sprint di energia per gli eBus di Barcellona, https://toolbox.enelx.com/it/project/barcelonaebus, accessed: 20 March 2025.

[23] ChargeSim, "Pantograph systems: Up vs. down configuration in electric bus charging," *ChargeSim*, 2024.

[24] "Technical data sheet. inverted pantograph sls 201.106."

[25] A. G. Emma Piedel, Enrico Lauth and D. Göhlich, "Review and evaluation of automated charging technologies for heavy-duty vehicles," *MDPI: Multidisciplinary Digital Publishing Institute*, 2024.

[26] "Super fast pantograph charging system 300kw/600kw, charger for buses and trucks - madeinchina.com."

[27] "Manufacturer 300kw 600kw pantograph ev bus charging station ultra fast charging - madeinchina.com."

[28] "Pantografo di ricarica rapida da 300 kw - alibaba.com."

[29] C. J. N. M. Andrew Valainis, Kyla Maki and A. Cilimburg, *Navigating Options for Transportation Electrification and Solar Charging: Steps and Lessons Learned in Montana Communities.* NREL, Office of Energy Efficiency and Renewable Energy, US department, June 2024.

[30] P. I. M. Kosowski and W. Collins, *MW Scale Electric Vehicle Charging.* THE ELECTRIC POWER RESEARCH INSTITUTE (EPRI), June 2021.

[31] K. C. Alana Aamodt and K. Coney, *ELECTRIFYING TRANSIT: A GUIDEBOOK FOR IMPLEMENTING BATTERY ELECTRIC BUSES.* NREL: National Renewable Energy Laboratory, April 2021.

[32] E. M. B. B. A. M. Jesse Bennett, Partha Mishra and A. Birky, *Estimating the Breakeven Cost of Delivered Electricity To Charge Class 8 Electric Tractors.* NREL: National Renewable Energy Laboratory, December 2022.